The sustainable freight railway: Designing the freight vehicle – track system for higher delivered tonnage with improved availability at reduced cost

SUSTRAIL

Grant Agreement n°: 265740 FP7 - THEME [SST.2010.5.2-2.]
Project Start Date: 2011-06-01
Duration: 48 months

D4.1

Performance Based Design Principles for Resilient Track

Due date of deliverable: 31/05/2014

Actual submission date: 25/7/2014

Work Package Number:	WP 4
Dissemination Level:	PU
Status:	Submitted
Leader of this deliverable:	NR
Prepared by:	Kevin Blacktop (NR) Donato Zangani, Clemente Fuggini (TRAIN) Yann Bezin, Ilaria Grossoni (HUD) Carlos Casanueva, Per-Anders Jönsson (KTH) Stefano Bruni, Stefano Alfi (POLIMI) Stephen M. Famurewa, Iman Arasteh Khouy, Matti Rantatalo, Ulla Juntti, Uday Kumar (LTU) AnVan Ho, Madassar Aslam, Robert Lambert (TATA Steel) Adam Beagles, David Fletcher (USFD)
Verified by:	Kevin Blacktop (NR)

Dissemination Level	
PU	Public
PP	Restricted to other programme participants (including the Commission Services)
RE	Restricted to a group specified by the consortium (including the Commission Services)
CO	Confidential, only for members of the consortium (including the Commission Services)

Document History			
Version	**Date**	**Author/s**	**Description**
D1	09.06.2014	Donato Zangani/Kevin Blacktop	Structure draft and introduction
D2	22.07.2014	All	Chapter population
Submitted	25.07.2014	All	Complete

Disclaimer

The information in this document is provided as is and no guarantee or warranty is given that the information is fit for any particular purpose. The user thereof uses the information at its sole risk and liability.

The document reflects only the author's views and the Community is not liable for any use that may be made of the information contained therein.

EXECUTIVE SUMMARY

Performance Based Design Principles for Resilient Track

Deliverable 4.1 utilises performance based design principles and complementary monitoring tools to determine the factors that influence the resistance of track to the different loads imposed on it by trains, and the means by which this resistance can be improved.

Split into 6 sub-packages, this work considers both the track as part of a system (in conjunction with the other tasks) and for its individual component parts e.g. rails, sleepers and fastenings. The 6 sub-packages are:-

- 4.1.1 - Determine Dynamic Loading of Wagons on Track and Key Components
- 4.1.2 - Influence of Track Stiffness on the Dynamic Loads caused by Wagons on Track and Key Components
- 4.1.3 - Develop Minimum Action Rules Approach to other Defects and New Technologies
- 4.1.4 - Mechanical Testing of Track Components
- 4.1.5a - Risk Analysis in the Design and Operation Phase
- 4.1.5b - From Safety Limits to Maintenance Limits

Determined loads include those imposed through vehicle body (sprung mass) and axle/suspension (un-sprung mass), and the dynamic loads associated with defects in wheels (flats and other out-of-round wheels) and track geometry (vertical and lateral forces). This also includes the impact of track stiffness.

Typical loading on track components for selected critical running vehicle-track combinations has been defined for rail pad forces; ballast-sleeper interface stresses and sleeper bending stresses, and sleeper & rail accelerations. This has enabled mechanical component testing and modelling of rail joints to be undertaken, which has highlighted the impact of rail foot corrosion in this area and the stress concentrations in the joint components.

Minimum Action Rules have been developed for rail foot corrosion, considering rail types and corrosion levels, which has proven that the technique can be used to assist in planning inspection routines and defining the remedial action required following the detection of a defect.

Risk analysis has been undertaken to demonstrate the benefits for Infrastructure Managers to visualise systems and components performance and subsequent interventions to deliver a high performing track. This includes estimations for both system and component failure frequencies and the consequences of failure.

Moving from reactive maintenance, based upon safety limits, to predictive maintenance limits has been considered using decision support tools and maintenance strategies to determine the most cost effective points to undertake maintenance activities. This work has included track geometry, contractor performance and tamping and has identified cost effective intervention limits.

Table of contents

EXECUTIVE SUMMARY **3**

1. INTRODUCTION & OVERVIEW **10**

2. TASK 4.1.1 DETERMINE DYNAMIC LOADS OF WAGONS ON TRACK AND ON KEY COMPONENTS **13**

2.1 CONSIDERATION FOR VARIOUS ASPECTS OF TRACK LOADING BASED ON VEHICLE TYPE, RUNNING CONDITIONS AND TRACK GEOMETRY/LAYOUT 13

2.1.1 Vehicle and running conditions *13*

2.1.2 Simulated routes *14*

2.1.3 track data long wavelength characteristics *14*

2.1.4 Vehicle quasi-static response to track longwavelength and running conditions *16*

2.1.5 Track quality effect on medium frequency (<20Hz) vertical dynamic forces *23*

2.1.6 Conclusion on section 2.1 ..... *29*

2.2 SIMULATION OF FREIGHT VEHICLE TRACK LOADING AND THE PREDICTED EFFECT OF THE SUSTRAIL VEHICLE 30

2.2.1 Characteristics of the virtual test track (VTT) *30*

2.2.2 Vehicles and running conditions *31*

2.2.3 Track quality effect on vertical dynamic forces *32*

2.2.4 Maximum and quasi-static track forces (Q_{dyn} and Y_{qst}) *33*

2.3 PREDICTING THE TRACK LOADING AND KEY COMPONENTS LOADING FOR THE SUSTRAIL SYSTEM LIMIT CONDITIONS 35

2.3.1 Numerical method for the simulation of train-track interaction *35*

2.3.2 Multi-body model of the railway vehicles *36*

2.3.3 The track model *36*

2.3.4 Simulation cases *39*

2.3.5 Simulation results: nominal vehicle condition *40*

2.3.6 Simulation results: effect of reduced un-sprung mass *50*

2.3.7 Simulation results: effect of track irregularity *51*

3. TASK 4.1.2 - INFLUENCE OF TRACK STIFFNESS ON THE DYNAMIC LOADS CAUSED BY WAGONS ON TRACKS AND ON KEY COMPONENTS **54**

3.1 INTRODUCTION ON TRACK STIFFNESS 54

3.2 THE EFFECT OF TRACK SUPPORT STIFFNESS ON TRACK BEHAVIOUR BASED ON UK MEASUREMENT 54

3.2.1 Measurement data for the sleeper support stiffness *55*

3.2.2 Vehicle and running conditions *56*

3.2.3 Simulation results *57*

3.2.4 Conclusions on section 3.2 ..... *68*

3.3 THE EFFECT OF TRACK SUPPORT STIFFNESS ON TRACK BEHAVIOUR AND KEY COMPONENTS BASED ON EUROBALT REFERENCE VALUES 68

3.3.1 The model of train-track interaction *69*

3.3.2 Results *69*

4. TASK 4.1.3 - DEVELOP MINIMUM ACTION RULES APPROACH TO OTHER DEFECTS AND FOR NEW TECHNOLOGIES (TATA STEEL) **71**

4.1 SCOPE OF WORK 71

4.1.1 Problem Statement *71*

4.2 INTRODUCTION TO MINIMUM ACTION MODEL 72

4.2.1 Input *72*

4.2.2 Output *73*

4.2.3 Other aspects of the program *74*

4.3 METHODOLOGY 75

4.3.1 Test Parameters *76*

4.4 RESULTS 76

4.4.1 Simulation result of 56E1 track *76*
4.4.2 Simulation result of 60E2 track *78*
4.5 DISCUSSION 79
4.5.1 56E1 and 60E2 ..... *79*
4.5.2 Probability of detection *79*
4.5.3 Expansion to include randomisation *80*
4.6 CONCLUSIONS 82

5. TASK 4.1.4 - MECHANICAL TESTING OF TRACK COMPONENTS (USFD) 83

5.1 INTRODUCTION 83
5.2 TESTING 83
5.2.1 Lipping *84*
5.2.2 Glues and liners *84*
5.2.3 Full scale tests *86*
5.3 FINITE ELEMENT MODELLING 87
5.4 CONCLUSIONS 90

6. TASK 4.1.5A - RISK ANALYSIS IN THE DESIGN AND OPERATION PHASE (LTU, NR, TRAIN) 92

6.1 ENGINEERING ANALYSIS 92
6.2 RISK MATRIX 93
6.3 CASE STUDY 94
6.4 CONCLUDING REMARKS 96

7. TASK 4.1.5B - FROM SAFETY LIMITS TO MAINTENANCE LIMITS (LTU, NR, TRAIN) 97

7.1 RESEARCH PURPOSE AND OBJECTIVES 97
7.2 TRACK GEOMETRY DEGRADATION AND ITS INFLUENCING PARAMETERS 97
7.3 ANALYSIS OF GEOMETRICAL DEGRADATION PROCESS IN TURNOUTS (CROSSING LOCATION) 101
7.4 EVALUATION OF CURRENT MAINTENANCE STRATEGY EFFECTIVENESS 104
7.5 SPECIFYING COST-EFFECTIVE MAINTENANCE LIMIT FOR TAMPING 105

List of Figures

FIGURE 2-1: RADIUS RANGE DISTRIBUTION ON UK SELECTED ROUTES 14
FIGURE 2-2: CANT DEFICIENCY DISTRIBUTION FOR ALL UK ROUTES AT 80%, 100% AND 120% OF LINESPEED.... 15
FIGURE 2-3: WHEEL-RAIL CONTACT FORCES AS A FUNCTION OF RADIUS (250M TO INFINITY) AND CANT DEFICIENCY (-100MM TO 200MM) 17
FIGURE 2-4: WHEEL-RAIL CONTACT FORCES AS A FUNCTION OF RADIUS (250M TO INFINITY) AND CANT DEFICIENCY (-100MM TO 200MM) FILTERED FOR UK ROUTES RUNNING CONDITIONS AT 80% OF LINESPEED 18
FIGURE 2-5: CHANGE IN BQST MAGNITUDE (LEFT) AND DIRECTION (RIGHT) UNDER THE LEADING AXLE AS A FUNCTION OF CANT DEFICIENCY FOR ALL RADII 22
FIGURE 2-6: CHANGE IN BQST FORCES UNDER THE LEADING AXLE AS A FUNCTION OF CURVE RADIUS FOR ALL CANT DEFICIENCIES. 23
FIGURE 2-7: FOUR UK TRACK HORIZONTAL LEVEL QUALITY (MAX SD OF LEFT OR RIGHT RAIL) OVER 200M SECTIONS, SHOWING MEAN VALUE OF SDS AS WELL AS MEAN + 3 SIGMA STANDARD DEVIATION 24
FIGURE 2-8: FOUR UK TRACK HORIZONTAL LEVEL QUALITY DISTRIBUTION (MAX SD OF LEFT OR RIGHT RAIL) OVER 200M SECTIONS AS A PERCENTAGE OF THE ROUTE, ALSO SHOWING THE MEAN VALUE OF SDS, THE EN13484 QUALITY BAND D LIMIT FOR SPEED IN THE RANGE 80 TO 120KM/H, MEAN + 3 SIGMA STANDARD DEVIATION OF SD VALUES AND NETWORK RAIL POOR QUALITY BAND FOR SPEED RANGE 75-80MPH. 25
FIGURE 2-9:UK TRACK QUALITY CUMULATIVE DISTRIBUTION COMPARED TO EU STANDARD EN13484 QUALITY BANDS 25
FIGURE 2-10: MAXIMUM WHEEL DYNAMIC FORCES COUNT: TARE (LEFT HAND COLUMN), LADEN (RIGHT HAND COLUMN), PART-LADEN (BOTTOM LEFT PLOT) FOR V3 (TOP ROW), V2 (MIDDLE ROW) AND V1 (BOTTOM TWO ROWS) VEHICLES. 27
FIGURE 2-11: MAXIMUM WHEEL DYNAMIC FORCE SD VERSUS TRACK QUALITY SD: TARE (LEFT HAND COLUMN), LADEN (RIGHT HAND COLUMN), PART-LADEN (BOTTOM LEFT PLOT) FOR V3 (TOP ROW), V2 (MIDDLE ROW) AND V1 (BOTTOM TWO ROWS) VEHICLES. 28
FIGURE 2-12: MAXIMUM WHEEL DYNAMIC FORCE SD VERSUS TRACK QUALITY SD – NORMALISED WITH RESPECT TO WHEEL LOAD: TARE (LEFT HAND COLUMN), LADEN (RIGHT HAND COLUMN), PART-LADEN (BOTTOM LEFT PLOT) FOR V3 (TOP ROW), V2 (MIDDLE ROW) AND V1 (BOTTOM TWO ROWS) VEHICLES. 29
FIGURE 2-13: VERTICAL TRACK IRREGULARITY, SD, FOR ALL SECTIONS OF THE FOUR CURVE CLASSES OF THE VIRTUAL TEST TRACK (VTT) 31
FIGURE 2-14: VERTICAL TRACK QUALITY DISTRIBUTION FOR ENTIRE VIRTUAL TEST TRACK (VTT). 31
FIGURE 2-15: MAXIMUM WHEEL DYNAMIC FORCE SD VERSUS TRACK QUALITY SD – NORMALISED WITH RESPECT TO WHEEL LOAD: REFERENCE VEHICLE AT 4.7, 17, 22.5 AND 25 TONNES AXLELOAD. 32
FIGURE 2-16: VERTICAL DYNAMIC TRACK FORCES, Q, FOR TRACK CLASSES 1-4. REFERENCE VEHICLE AT 22.5 TONNES AXLELOAD. 33
FIGURE 2-17: LATERAL QUASISTATIC TRACK FORCES, Y_{QST}, FOR TRACK CLASSES 1-4. REFERENCE VEHICLE AT 22.5 TONNES AXLELOAD. 34
FIGURE 2-18: COMPARISON OF VERTICAL AND LATERAL TRACK FORCES BETWEEN REFERENCE AND SUSTRAIL VEHICLE. 34
FIGURE 2-19: COMPARISON OF VERTICAL AND LATERAL TRACK FORCES BETWEEN REFERENCE AND SUSTRAIL VEHICLE. 35
FIGURE 2-20: SECTIONAL MODEL OF THE TRACK 37
FIGURE 2-21: BALLAST VOLUME SUBJECT TO STRESS TRANSFER FROM THE SLEEPER 38
FIGURE 2-22: REPARTITION OF THE TOTAL BALLAST MASS ON THE SLEEPER, LUMPED MASS AND FIXED LOWER BOUNDARY 39
FIGURE 2-23: POINTS OF THE RAIL SECTION AT WHICH STRESSES ARE EVALUATED 41
FIGURE 2-24: MAXIMUM RAIL SEAT LOAD ON 21 CONSECUTIVE SLEEPERS. NOMINAL VEHICLE CASE, AXLE LOAD 25 T/AXLE, SPEED 120 KM/H. 42
FIGURE 2-25: TIME HISTORY OF THE RAIL SEAT LOAD (LEFT – BLUE, RIGHT – RED) ON SLEEPER N.21. NOMINAL VEHICLE CASE, AXLE LOAD 25 T/AXLE, SPEED 120 KM/H. 43
FIGURE 2-26: MAXIMUM RAIL SEAT LOAD ON 21 CONSECUTIVE SLEEPERS. NOMINAL VEHICLE CASE, AXLE LOAD 22.5 T/AXLE, SPEED 120 KM/H. 43
FIGURE 2-27: TIME HISTORY OF THE RAIL SEAT LOAD (LEFT – BLUE, RIGHT – RED) ON SLEEPER N.21. NOMINAL VEHICLE CASE, AXLE LOAD 22.5 T/AXLE, SPEED 120 KM/H. 44
FIGURE 2-28: MAXIMUM RAIL SEAT LOAD ON 21 CONSECUTIVE SLEEPERS. NOMINAL VEHICLE CASE, AXLE LOAD 17 T/AXLE, SPEED 120 KM/H. 44
FIGURE 2-29: TIME HISTORY OF THE RAIL SEAT LOAD (LEFT – BLUE, RIGHT – RED) ON SLEEPER N.10. NOMINAL VEHICLE CASE, AXLE LOAD 17 T/AXLE, SPEED 120 KM/H. 45

FIGURE 2-30: MAXIMUM SLEEPER-BALLAST CONTACT PRESSURE ON 21 CONSECUTIVE SLEEPERS. NOMINAL VEHICLE 7CASE, AXLE LOAD 25 T/AXLE, SPEED 120 KM/H. 46
FIGURE 2-31: TIME HISTORY OF THE SLEEPER-BALLAST CONTACT PRESSURE (LEFT – BLUE, RIGHT – RED) ON SLEEPER N.21. NOMINAL VEHICLE CASE, AXLE LOAD 25 T/AXLE, SPEED 120 KM/H. 47
FIGURE 2-32: MAXIMUM BENDING STRESSES AT MID SLEEPER BAY EVALUATED ON 21 CONSECUTIVE SLEEPER BAYS. NOMINAL VEHICLE CASE, AXLE LOAD 25 T/AXLE, SPEED 120 KM/H. 50
FIGURE 2-33: TIME HISTORY OF THE BENDING STRESS AT MID SLEEPER BAY, SLEEPER BAY N.3. NOMINAL VEHICLE CASE, AXLE LOAD 25 T/AXLE, SPEED 120 KM/H. 50
FIGURE 2-34: COMPARISON OF MEASURED IRREGULARITY PSD CURVE VS ORE/ERRI LOW AND HIGH LEVEL (LEFT: VERTICAL PROFILE, RIGHT: LATERAL ALIGNMENT). 52
FIGURE 3-1: VERTICAL VEHICLE-TRACK COUPLING MODEL. 55
FIGURE 3-2: SUPPORT STIFFNESS DISTRIBUTION IN CASE OF (A) SITE 1, (B) SITE 2, (C) SITE 3, (D) SITE 4. 56
FIGURE 3-3: CURVE FITTING FOR THE FOUR SITES CONSIDERED 56
FIGURE 3-4: (A) BALLAST FORCES VERSUS SPEED VARYING THE SITE; (B) PERCENTAGE DIFFERENCE OF BALLAST FORCE WITH THE MEAN VALUE VERSUS SPEED VARYING THE SITE. 57
FIGURE 3-5: MEAN BALLAST FORCE RESPONSE AS A FUNCTION OF SITE MEAN SUPPORT STIFFNESS 57
FIGURE 3-6: SELECTED DISTRIBUTION OF THE BALLAST FORCE FOR SITE 1, 2, 3 AND 4 (FROM TOP TO BOTTOM).... 59
FIGURE 3-7: DISTRIBUTION OF THE BALLAST FORCE VERSUS DISTRIBUTION OF STIFFNESS SUPPORT ((A) SITE 1; (B) SITE 2; (C) SITE 3; (D) SITE 4). 59
FIGURE 3-8: (A) SLEEPER DISPLACEMENT VERSUS SPEED VARYING THE SITE; (B) – PERCENTAGE DIFFERENCE OF SLEEPER DISPLACEMENT WITH THE MEAN VALUE VERSUS SPEED VARYING THE SITE. 60
FIGURE 3-9: SELECTED DISTRIBUTION OF THE SLEEPER DISPLACEMENT FOR SITE 1, 2, 3 AND 4 (FROM TOP TO BOTTOM) 61
FIGURE 3-10: DISTRIBUTION OF THE SLEEPER DISPLACEMENT VERSUS DISTRIBUTION OF STIFFNESS SUPPORT: (A) SITE 1; (B) SITE 2; (C) SITE 3; (D) SITE 4 62
FIGURE 3-11: (A) SLEEPER ACCELERATION VERSUS SPEED VARYING THE SITE; (B) PERCENTAGE DIFFERENCE OF SLEEPER ACCELERATION WITH THE MEAN VALUE VERSUS SPEED VARYING THE SITE. 62
FIGURE 3-12: SELECTED DISTRIBUTION OF THE SLEEPER ACCELERATION FOR SITE 1, 2, 3 AND 4 (FROM TOP TO BOTTOM) 64
FIGURE 3-13: DISTRIBUTION OF THE SLEEPER ACCELERATION VERSUS DISTRIBUTION OF STIFFNESS SUPPORT: (A) SITE 1; (B) SITE 2; (C) SITE 3; (D) SITE 4 64
FIGURE 3-14: EXAMPLE OF RAIL BENDING STRESS. 65
FIGURE 3-15: (A) RAIL STRESS VERSUS SPEED VARYING THE SITE; (B) PERCENTAGE DIFFERENCE OF RAIL STRESS WITH THE MEAN VALUE VERSUS SPEED VARYING THE SITE. 66
FIGURE 3-16: EXAMPLE OF DISTRIBUTION OF THE RAIL STRESS FOR SITE 1, 2, 3 AND 4 (FROM TOP TO BOTTOM) ... 67
FIGURE 3-17: DISTRIBUTION OF THE RAIL STRESS VERSUS DISTRIBUTION OF STIFFNESS SUPPORT: (A) SITE 1; (B) SITE 2; (C) SITE 3; (D) SITE 4 68
FIGURE 4-1 - AN EXAMPLE OF A FATIGUE CRACK IN THE FOOT OF A RAIL 71
FIGURE 4-2 - LOSS OF FOOT AREA FROM CORROSION 72
FIGURE 4-3 - CRACK GEOMETRY 73
FIGURE 4-4 – EXAMPLE OUTPUT FILE 74
FIGURE 4-5- PROBABILITY OF DETECTION CURVE FOR MINIMUM ACTION MODEL 75
FIGURE 4-6 - EXAMPLE OF MODELLED FOOT CORROSION 75
FIGURE 4-7 - THE GROWTH OF A 2 MM CRACK ON 56E1 TRACK WITH DIFFERENT LEVELS OF REDUCTION IN FOOT AREA DUE TO CORROSION 77
FIGURE 4-8 - THE GROWTH OF A 2 MM CRACK ON 60E2 TRACK WITH DIFFERENT LEVELS OF REDUCTION IN FOOT AREA DUE TO CORROSION 78
FIGURE 4-9 - DISTRIBUTION OF OUTCOMES FOR VARYING CORROSION LEVELS 80
FIGURE 4-10 - CRACK GROWTH FOR RANDOMISED AND UNRANDOMISED MODEL RUNS WITH 0MM CORROSION 81
FIGURE 4-11 - CRACK GROWTH FOR RANDOMISED AND UNRANDOMISED MODEL RUNS WITH VARYING LEVELS OF CORROSION 81
FIGURE 5-1: A TYPICAL INSULATED JOINT 83
FIGURE 5-2: TYPICAL TEST PIECES IN SUROS MACHINE AND RAIL DISC WITH ENDPOST INSERTS 84
FIGURE 5-3: SMALL-SCALE GLUE AND LINER SHEAR TESTS 85
FIGURE 5-4: SHEAR TEST OF JOINT SECTION 85
FIGURE 5-5: FOUR-POINT BENDING RIG 86
FIGURE 5-6: STANDARD RAIL JOINT FAILURE 87
FIGURE 5-7: MODIFIED RAIL JOINT FAILURE 87
FIGURE 5-8: FINITE ELEMENT MESH OF RAIL AND IBJ 88
FIGURE 5-9: MAJOR PRINCIPAL STRESS IN FISHPLATE FOR DEBONDED GLUE 89
FIGURE 5-10: MAJOR PRINCIPAL STRESS IN STUCK FISHPLATE 89

FIGURE 5-11: LONGITUDINAL (Z) STRESS IN ENDPOST 90
FIGURE 5-12: LONGITUDINAL STRESS IN GLUED JOINT ASSEMBLY 90
FIGURE 6-1: ENGINEERING ANALYSIS FOR HIGH PERFORMING TRACK SYSTEM 92
FIGURE 6-2: RISK MATRIX DESIGN USING QUANTITATIVE AND QUALITATIVE APPROACH 93
FIGURE 6-3: TYPICAL RISK EVALUATION MATRIX 94
FIGURE 6-4: CRITICAL FAILURE MODES BASED ON FAILURE FREQUENCY AND DELAY CONSEQUENCE 95
FIGURE 6-5: WEAKEST LINKS (I.E. TRAFFIC ZONES) ON THE LINE 95
FIGURE 6-6: CATEGORISATION OF ZONES BASED ON THE RISK OF TARGET PERFORMANCE REQUIREMENTS 96
FIGURE 7-1 ISHIKAWA DIAGRAM (CAUSE AND EFFECT DIAGRAM) OF THE FACTORS INFLUENCING TRACK GEOMETRY DEGRADATION. 98
FIGURE 7-2 HISTOGRAM OF LONGITUDINAL LEVEL DEGRADATION RATES IN TANGENT SEGMENTS BETWEEN 2007 AND 2009. 98
FIGURE 7-3 CUMULATIVE DISTRIBUTION FUNCTIONS OF GEOMETRY FAULTS VERSUS MGT (A) B-FAULTS, (B) C-FAULTS AND (C) TWIST (3 M & 6 M) FAILURES. 101
FIGURE 7-4 DEFINED GEOMETRY PARAMETERS IN THE SECOND APPROACH 102
FIGURE 7-5 TRENDS OF THE DEFINED GEOMETRY PARAMETERS IN SELECTED TURNOUTS (A) PARAMETER A, (B) PARAMETERS C & D, (C) PARAMETERS E & F, (D) PARAMETERS E' & F' AND (E) PARAMETERS G & H ... 104
FIGURE 7-6 EVALUATION OF THE CONTRACTOR'S PERFORMANCE A: CONTRACTOR'S PERFORMANCE ON THE CASE STUDY LINE. B: CONTRACTOR'S PERFORMANCE ON A REFERENCE LINE IN CENTRAL SWEDEN 104
FIGURE 7-7 OBSERVED TAMPING EFFECTIVENESS WITHIN STUDIED TIME INTERVAL 106
FIGURE 7-8 COMPARISON OF MAINTENANCE COST PER MGT FOR DIFFERENT INTERVENTION LIMITS 106

List of Tables

TABLE 2.1: VEHICLE CHARACTERSITICS AS USED FOR VAMPIRE SIMULATIONS 14
TABLE 2.2 : UK ROUTES STATISTICS 14
TABLE 2.3: BQST FORCE MAGNITUDE [KN] (LEFT COLUMN) AND ANGLE TO VERTICAL [DEG] (RIGHT COLUMN) FOR ALL COMBINED UK ROUTES AT 80% LINE SPEED. FROM TOP TO BOTTOM: LEADING AXLE HIGH RAIL, LEADING AXLE LOW RAIL, TRAILING AXLE HIGH RAIL AND TRAILING AXLE LOW RAIL 19
TABLE 2.4: BQST FORCE MAGNITUDE [KN] (LEFT COLUMN) AND ANGLE TO VERTICAL [DEG] (RIGHT COLUMN) FOR ALL COMBINED UK ROUTES AT 100% LINE SPEED. FROM TOP TO BOTTOM: LEADING AXLE HIGH RAIL, LEADING AXLE LOW RAIL, TRAILING AXLE HIGH RAIL AND TRAILING AXLE LOW RAIL 20
TABLE 2.5: BQST FORCE MAGNITUDE [KN] (LEFT COLUMN) AND ANGLE TO VERTICAL [DEG] (RIGHT COLUMN) FOR ALL COMBINED UK ROUTES AT 120% LINE SPEED. FROM TOP TO BOTTOM: LEADING AXLE HIGH RAIL, LEADING AXLE LOW RAIL, TRAILING AXLE HIGH RAIL AND TRAILING AXLE LOW RAIL 21
TABLE 2.6: PECENTAGE OF FORCE SD INCREASE (WRT NOMINAL) PER UNIT TRACK SD 28
TABLE 2-7: MAIN CHARACTERISTICS OF THE VIRTUAL TEST TRACK (VTT), WITH V_{ADM} AND CD_{ADM} THE ADMISSIBLE VEHICLE SPEED AND ADMISSIBLE CANT DEFICIENCY RESPECTIVELY AS PER EN14363. 30
TABLE 2-8: PECENTAGE OF FORCE SD INCREASE (WRT NOMINAL) PER UNIT TRACK SD 33
TABLE 2.9: TRACK STIFFNESS AND DAMPING VALUES FROM THE EUROBALT PROJECT 37
TABLE 2.10: COMBINATIONS OF AXLE LOAD AND VEHICLE SPEED CONSIDERED FOR THE NOMINAL VEHICLE CONDITION 40
TABLE 2.11: OVERALL MAXIMA OF THE RAIL SEAT LOAD FORCES FOR THE NOMINAL VEHICLE CONDITION AND FOR VARIOUS SPEED AND AXLE LOAD VALUES. 42
TABLE 2.12: OVERALL MAXIMA OF THE SLEEPER-BALLAST CONTACT PRESSURE FOR THE NOMINAL VEHICLE CONDITION AND FOR VARIOUS SPEED AND AXLE LOAD VALUES. 46
TABLE 2.13: OVERALL MAXIMA OF THE RAIL BENDING STRESSES AT MID SLEEPER BAY FOR THE NOMINAL VEHICLE CONDITION AND FOR VARIOUS SPEED AND AXLE LOAD VALUES. 49
TABLE 2.14:COMPARISON OF MAXIMUM RAIL SEAT LOADS, SLEEPER-BALLAST CONTACT PRESSURE (SBCP) AND RAIL STRESSES FOR THE NOMINAL VEHICLE CONDITION AND FOR REDUCED (-10%) UN-SPRUNG MASS. 51
TABLE 2.15: COMPARISON OF MAXIMUM RAIL SEAT LOADS, SLEEPER-BALLAST CONTACT PRESSURE (SBCP) AND RAIL STRESSES FOR ORE/ERRI "HIGH LEVEL" AND MEASURED TRACK IRREGULARITIES 53
TABLE 3.1: MAIN CHARACTERISTICS OF THE ANALYSED SITES 56
TABLE 3.2: MEAN VALUES OF BALLAST FORCE AS A FUNCTION OF SPEED 58
TABLE 3.3: MEAN VALUES OF SLEEPER DISPLACEMENT DEPENDING ON THE SPEED. 60
TABLE 3.4: MEAN VALUES OF SLEEPER ACCELERATION DEPENDING ON THE SPEED 63
TABLE 3.5: MEAN VALUES OF RAIL STRESS DEPENDING ON THE SPEED 66

TABLE 3.6: COMPARISONOF MAXIMUM RAIL SEAT LOADS, SLEEPER-BALLAST CONTACT PRESSURE (SBCP) AND RAIL STRESSES FOR A "TYPICAL" TRACK AND "STIFF" TRACK. 70
TABLE 7 - BASIC INPUT PARAMETERS 76
TABLE 8: SUMMARY OF TEST CASE RESULT SHOWING THE CRACK SIZE AT FAILURE AND THE REDUCTION IN LIFE OF 56E1 TRACK WITH DIFFERENT LEVEL OF FOOT CORROSION 78
TABLE 9: SUMMARY OF TEST CASE RESULT SHOWING THE CRACK SIZE AT FAILURE AND THE REDUCTION IN LIFE OF 60E2 TRACK WITH DIFFERENT LEVEL OF FOOT CORROSION 79
TABLE 10: COMPARISON BETWEEN 56E1 AND 60E2 PROFILE 79

1. INTRODUCTION & OVERVIEW

Sustainable Track (Work Package 4) will facilitate the need for the railway infrastructure to accommodate more traffic whilst at the same time reducing deterioration of track and wheels through increasing the resistance of the track to the loads imposed on it by vehicles. This will assist in sustainable achievement of increased speed and capacity for freight traffic, thus contributing towards making rail freight more competitive.

There is a very strong coupling to WP3 - The freight train of the future, since it is essential to undertake a systems approach to analyse the combined track and vehicle loads and deterioration. The outputs from the WP4 will also inform the decision making for WP5 - Business Case that will select the most promising infrastructure technologies for testing and demonstration. Sustainable Track (Work Package 4) is made up of 5 tasks:-

- Task 4.1: Performance based design principles for resilient track
- Task 4.2: Supportive ballast and substrate
- Task 4.3: Optimised track systems and geometry
- Task 4.4: Switches and Crossings
- Task 4.5: Track-based monitoring and limits for imposed loads

The five tasks complement each other to deliver new techniques, analysis and modelling tools to understand the challenges of the existing track and vehicle system and also to predict the impact of the proposed SUSTRAIL future freight train (WP3).

Deliverable - Task 4.1 - Performance based design principles for resilient track

This task utilises performance based design principles and complementary monitoring tools to determine the factors that influence the resistance of track to the different loads imposed on it by trains, and the means by which this resistance can be improved. This deliverable comprises of the following 6 sub-packages:-

Task 4.1.1 - Determine Dynamic Loading of Wagons on Track and Key Components (Chapter 2)

The scope of 4.1.1 is to predict track forces and load distributions using mathematical modeling of vehicle track interaction. Four UK routes were analysed for distribution of curvature, cant, actual line speed and raised line speed. Track irregularities were also considered. This analysis allowed static and dynamic forces to be determined for 3 reference conventional freight wagon models and to develop predictions for the reduction in forces due to design improvements for the proposed SUSTRAIL wagons.

Assessment was undertaken of the typical force reaction of the track key components and stresses for the reference freight vehicle (17.5t, 22.5t and 25t axle load) running at 80, 120 and 140km/h. This also included consideration of fully laden and part laden vehicles, which showed the highest variation in dynamic loading. This has highlighted the need for the proposed SUSTRAIL vehicle to have good performance in both load conditions. This work has also highlighted the benefit of reducing un-sprung mass of the wagon to counter rising rail bending stress with rising speed.

Task 4.1.2 - Influence of Track Stiffness on the Dynamic Loads caused by Wagons on Track and Key Components (Chapter 3)

The scope of this work is to analyse the influence of the variability of the support conditions on the vehicle track dynamic interaction. The approach taken is to use a vehicle-track coupling model in which the sleeper ballast stiffness interface can be modified on every individual sleeper to reflect ballast stiffness values obtained from UK route measurements.

The results for the stiff ballast / sleeper interface track are compared to the results for the typical track already presented in the previous sub-package. The comparison has been undertaken at the maximum speed considered for each axle load value. The increase of track stiffness leads to a significant increase of the rail seat loads and sleeper-ballast contact pressure, in the order of +16 – 20%. This is due to the fact that stiffer track is less efficient than a more deformable one in distributing the wheel load, therefore, the amount of load applied on the sleeper by the presence of a wheel is increasing for increasing track stiffness. However, a stiffer sleeper support leads to lower bending moment in the rails, due to less deflection. This is the reason why the bending stresses in the rail are lower for the stiff track case, especially for the 22.5t and 25t axle loads.

Task 4.1.3 - Develop Minimum Action Rules Approach to other Defects and New Technologies (Chapter 4)

The scope of this work for is to expand the Minimum Action methodology into additional defects/rail regimes. Due to its importance in track maintenance, rail foot corrosion was chosen as a suitable defect to apply the Minimum Action model as corrosion defects can have a large bearing on the life of a rail.

Three corrosion levels were modelled and results reported using unrandomised single model run data to provide exact figures. Additionally, a larger randomised variable run was undertaken to demonstrate the validity of the single run data.

The work highlighted that corrosion of even 0.5mm all around the foot has a significant influence on the lifetime before failure and higher levels of corrosion show even more severe reductions. The 60E2 rail profile shows more resistance to corrosion over 56E1 profile due to the increased cross sectional area.

Overall this work demonstrated that the Minimum Action model can be utilised to assist in planning inspection routines and defining the remedial action required following the detection of a defect.

Task 4.1.4 - Mechanical Testing of Track Components (Chapter 5)

The performance of insulated rail joints (IBJ) was identified in SUSTRAIL deliverable 2.5 as needing improvement. A range of tests have been undertaken to investigate the effect of varying properties on the performance of rail joints. Some novel tests have been undertaken and have the potential to be used to investigate the behaviour of different materials and geometries for insulated joints.

The physical testing has been supported by finite element modelling, the results of which suggest that the mechanical strength of joints is not adversely affected by debonding of glue

in the joint, but there may be adverse electrical effects if debonding reduces the resistance of the insulation.

It was found that the use of absorbant liners increases the shear capacity of the glued joint. It was also found that hard endpost materials are less prone to failure by lipping, and that the rate of lipping is not affected by the thickness of the endpost.

A significant finding is that it is important to check the underside of rails adjacent to joints as high stresses here can lead to failure of the rail. A redesign of the ends of fishplates could reduce the stress concentration at these locations.

Task 4.1.5a - Risk Analysis in the Design and Operation Phase (Chapter 6)

An essential aspect, of sustainable railway vehicle and track system, is effective engineering analysis and assessment of the system at the different life cycle phases, this requires a systematic engineering analyses of the railway network is undertaken to support a high performing and resilient track system in the design and operation phase.

The risk matrix tool provides a visual presentation and categorisation of systems and components into different risk groups. The result shows the traffic zones which are weakest link on the route investigated. Further analysis can be done on the items and subsystems in the line sections to rank them for improvement purposes. In case where economic and safety consequence are required (besides operation consequence), the second axis in the matrix can be changed to a combine all in cost terms.

It is common at the design stage to have limited data for analysis, but techniques such as similarity analysis (for existing system or change in design parameters), stress analysis (for new operating conditions), simulation modelling or expert judgment (for new design) can be used to estimate failure frequency and consequences.

Task 4.1.5b - From Safety Limits to Maintenance Limits (Chapter 7)

This section describes a method for cost-effective maintenance of railway track geometry with the aim of moving the maintenance decision making from an approach based on safety limits to a process based on maintenance limits.

The work undertaken to optimise track geometry maintenance by identifying cost-effective maintenance limits included track geometry degradation analysis, evaluation of the effectiveness of the present Trafikverket (Swedish Transport Administration) track geometry maintenance strategy and defining the geometrical degradation process in turnouts.

The developed models define a cost-effective inspection interval and identify maintenance limits. These models were developed using contractor performance, tamping effectiveness and geometry degradation.

2. TASK 4.1.1 DETERMINE DYNAMIC LOADS OF WAGONS ON TRACK AND ON KEY COMPONENTS

In this chapter numerical tools of the vehicle and track interaction are used to predict the typical track loading expected from freight vehicles in different track types and running conditions. The range of parameters investigated are mainly the range of curves, the vehicle speed and the resulting cant deficiency that the freight vehicle is expected to run at. This has a strong influence on the output vertical (Q) and lateral forces (Y) at each of the wheel-rail interface of the vehicle. Using the cases of the UK routes, it is shown how much the expected combined vertical and lateral load (B_{qst}) can be expected to increase in the worst conditions, which are those met in the tightest curves at the highest cant deficiency. Additionally the effect of track irregularities on the vertical vehicle dynamic behaviour is also investigated in details, so that a dynamic coefficient can be estimated based on the type of vehicle and the track quality considered. Various version of Y-series freight vehicles have been compared and evenutally the improved performance of selected SUSTRAIL vehicle innovations are assessed and compared with the best reference base case. The final part of the chapter is using a more advanced vehicle-track interaction model including details about the track support, so as to assess the impact of vehicle speed and axle load onto the force distribution in track and its components. This then links into the following section on track support stiffness.

2.1 Consideration for various aspects of track loading based on vehicle type, running conditions and track geometry/layout

In WP2.4, track data was collected for the four UK routes and vehicle dynamic simulation of several existing freight vehicles was carried out by the University of Huddersfield to predict the expected wheel-rail contact forces in the low frequency range (below <20Hz) as influenced by vehicle dynamics aspects. Based on this data (track characteristics and simulation output), expected typical track loading have been analysed inferred. The following is included:

- Description of the UK routes characteristics in terms of curvature and running cant deficiency (based on line permissible speed).
- Tables of quasi-static load (low frequency – long wavelength) applied by the freight vehicles on these routes and under the specified running conditions.
- Distribution of low frequency dynamics forces (below 20Hz) of the freight vehicles on the routes as a function of the track quality.

2.1.1 Vehicle and running conditions

Three variant of validated Vampire® models of Y-series types freight vehicles have been simulated in WP2 and they are name variant_1, variant_2 and variant_3. The main characteristics are summarised in the Table 2.1below:

Vehicle	Bogie type	Bogie wheelbase	Pivot spacing	Axle load
v1 Laden	Y33	2m	13.94m	199 kN (20.3t)
v1 Part Laden	-	-	-	108 kN (11t)
v1 Tare	-	-	-	49.4 kN (5t)

v2 Laden	Y25	2m	13.65m	252 kN (25.7t)
v2 Tare	-	-	-	67.4 kN (6.9t)
v3 Laden	Y25	1.8m	8.84m	221 kN (22.5t)
v3 Tare	-	-	-	55.7 kN (5.7t)

Table 2.1: vehicle charactersitics as used for Vampire simulations

2.1.2 Simulated routes

The four UK routes reported in D2.4 are used in this report, they are referenced as:

- Route 1: DCL 2100 - Chester Line Jn 53mi 12ch to Leamington Spa Jn 106mi 25ch
- Route 2: EMP 2100 - Ely North 71mi 63ch to Peterborough Jn 100mi 2ch
- Route 3: BML1 1100 - Northam Short Jn 77mi 68ch to Basingstoke Jn 47mi 52ch
- Route 4: LEC2 to LEC5 - Nuneaton 87mi 10ch to Crewe 158mi 0ch

2.1.3 track data long wavelength characteristics

The total length of the routes and percentage of tangent track are as given in Table 2.2.

	% tangent (R>9km)	total length (m)
Route 1	26%	85,377
Route 2	82%	40,422
Route 3	65%	48,742
Route 4	40%	92,128
All combined	48%	266,669

Table 2.2 : UK routes statistics

The percentage distribution of curves for each route and for the combined data is shown in Figure 2-1. The data is based on recorded track curvature signal. There is a very small proportion of tight curves (R<775m) on route 2 and 4, which in some cases may be attributed to short transient running through switches and crossings. The radius distribution chart is produced using every single value of these channels (measured every 0.2m) without track section averaging, therefore shorter transients features are reflected in this chart.

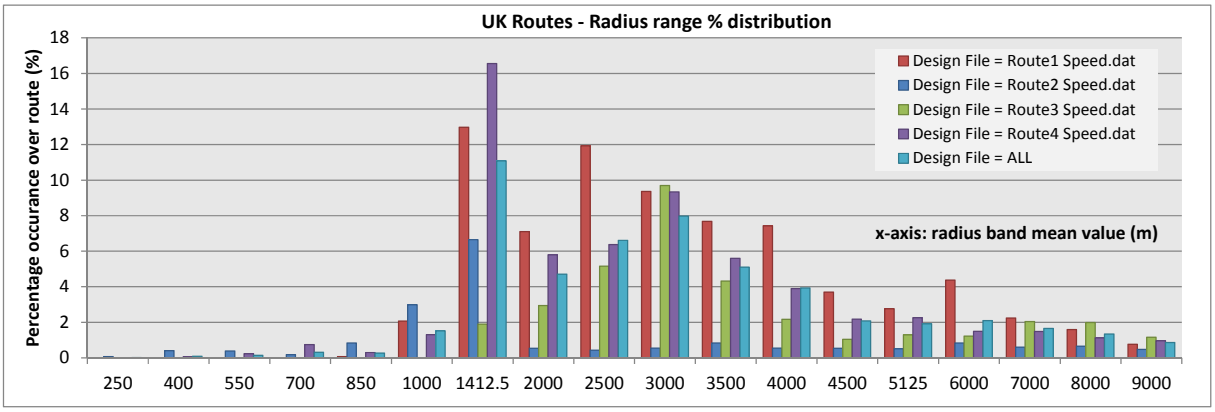

Figure 2-1: radius range distribution on UK selected routes

Figure 2-2 shows the distribution of cant deficiency[1] for each of the routes for 80% linespeed (realistic actual), 100% linespeed (potential optimum) and 120% linespeed (futuristics optimum) respectively. The increase in speed highlight a shift of running conditions from cant excess towards cant deficiency. Further details are given in the following section 2.1.3.1.

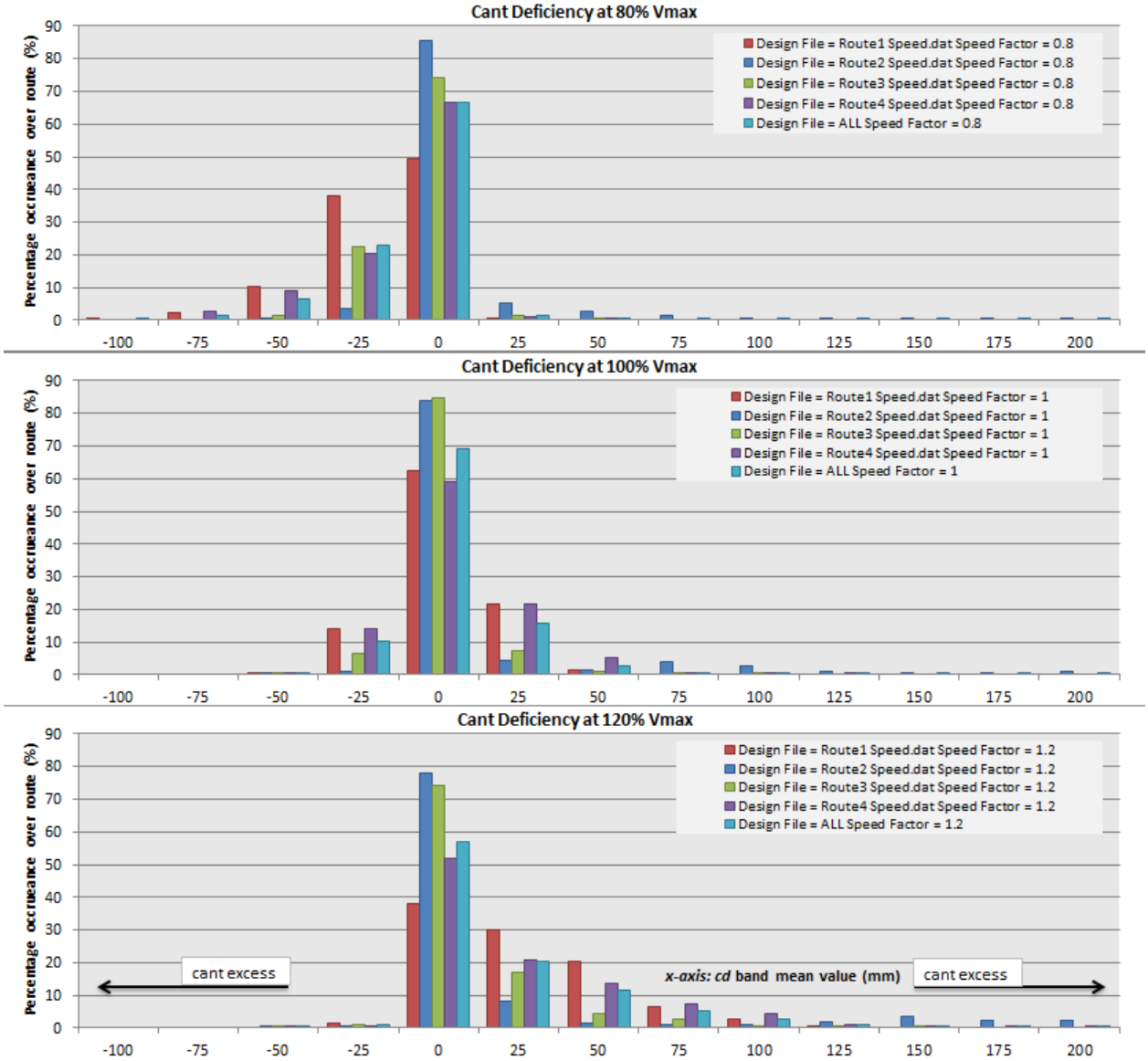

Figure 2-2: Cant deficiency distribution for all UK routes at 80%, 100% and 120% of linespeed

2.1.3.1 Interpretation of route long wavelength characterisitcs

For the vehicle running at 80% of the quoted linespeed the majority of the running conditions are near balanced speed on most routes: 49% (route 1), 86% (route 2), 74% (route 3) and 67% (route 4). A significant proportion of the curves produce a cant excess running condition: e.g. around -25mm for 20% of route 3 and 4, and near 40% of route 1. A few cases cases exist with larger cant excess around -75mm. This would most likely represent current running condition for freight traffic on these routes, and most likely the speed would be lower in a lot of places where freight traffic has to slow down, thus leading to even more cant excess.

[1] Cant deficiency calculated as: *CD* = Eq (equilibrium cant) – Ea (applied cant) = $11.82xV^2/R$ – Ea Where V is the linespeed (km/h) and R the curve radius (m). Ea and Eq are in mm

For the vehicle running at 100% of the linespeed, the majority of the running conditions are also at balanced speed on most routes as would be expected: 62% (route 1), 83% (route 2), 85% (route 3) and 58% (route 4). A small proportion of the curves produce low value cant excess, which is a consequence of the mixed traffic routes where curves are generally canted for faster vehicles. Some proportion of the curves now also produce cant deficiency around 25mm or above. A few extreme values are noticeable above 100mm and these would most likely correspond to switches and crossing with no superelevation. These running conditions would be representative of the optimised SUSTRAIL freight vehicle running at optimum linespeed.

For the vehicle running at 120% of the linespeed, the majority of the running conditions remain at balanced speed on all routes: 38% (route 1), 78% (route 2), 74% (route 3) and 52% (route 4). A significant proportion of the curves produce cant deficiency up to around 100mm and extreme values remain above 100mm. These running conditions would be representative of the futuristic SUSTRAIL freight vehicle running at raised speed above current linespeed.

2.1.4 Vehicle quasi-static response to track longwavelength and running conditions

The WP2 freight vehicle v1 model from Vampire with 20t axle load (99.5kN wheel load) was used to predict typical wheel-rail contact force output using quasi-static runs corresponding to the curve radius and cant deficiency conditions listed previously. As freight vehicles with friction damped suspension do not provide reliable results for pure steady state curving analyses (due to the hysteresis caused by the static break-out friction) irregularities from the Vampire track file Track110 were superimposed over the curve design geometry. The output mean value is then taken as the equivalent quasi-static. The following outputs are produced:

- **FY**, **FX** and **FZ** the resultant total force at any wheel of the leading bogie (leading axle, trailing axle, left and right wheels) in lateral, longitudinal and vertical direction respectively.
- **Tgamma** (leading axle, trailing axle, left, right and flange contact).
- **Bqst** the resultant total force in the vertical plane and the corresponding angle from vertical, derived from FY and FZ [Bqst=sqrt(FY^2+FZ^2)] (leading axle, trailing axle, left and right wheels).

In terms of track loading the main quantity of interest is B_{qst} as it is the combined vertical and lateral loading on the high and low rails from various axles. This quantity is explored further in the following section.

2.1.4.1 Investigation of total wheel-rail force (FY, FZ and Bqst)

Quasi-static wheel rail contact forces can be expresssed in table form as a function of curve radius and cant deficiency. This may also be plotted (FZ against FY) to show the magnitude and direction of the Bqst force at each wheel for all possible track running conditions. Figure 2-3 shows all possible forces for leading/trailing axle on high and low rail. Dark blue markers indicate cant excess while light blue indicate cant deficiency. Each point for a same marker indicate the range of radii considered. It can be seen that the leading axle is highly influenced both by the cant deficiency and the curve radius, while the trailing axle is mainly influenced by the cant deficiency. As the curve tightens and the cant deficiency increases the forces deviate from equal balance on the high and low rails and lateral component increases.

These results can then be filtered to reflect the actual running conditions of the track of interest, in this case the combined UK routes. Figure 2-4 shows the same results removing the points which do not apply to this route of the assumed actual running conditions (80% of

linespeed). The full tables used for these plot can be found in Table 2.3, 2.4 and 2.5 for 80%, 100% and 120% of linespeed.

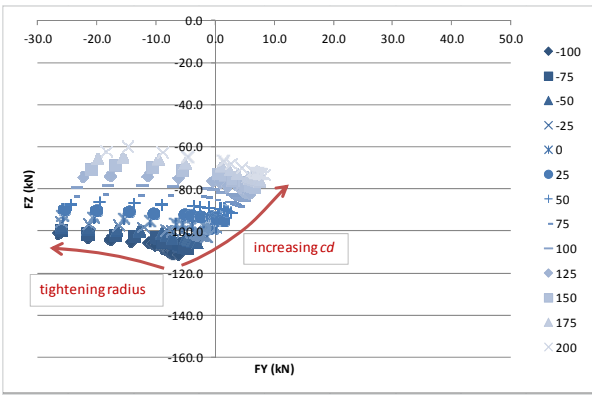

Leading axle - low rail

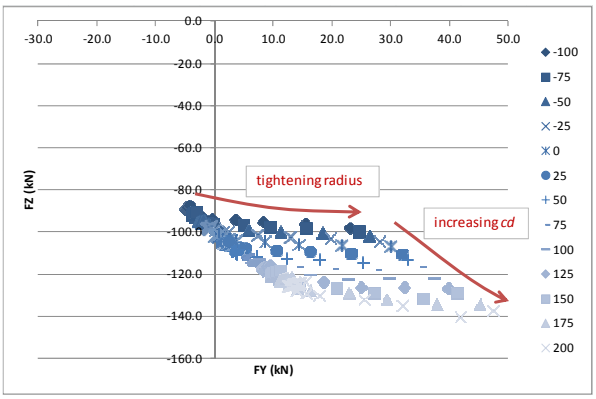

Leading axle - high rail

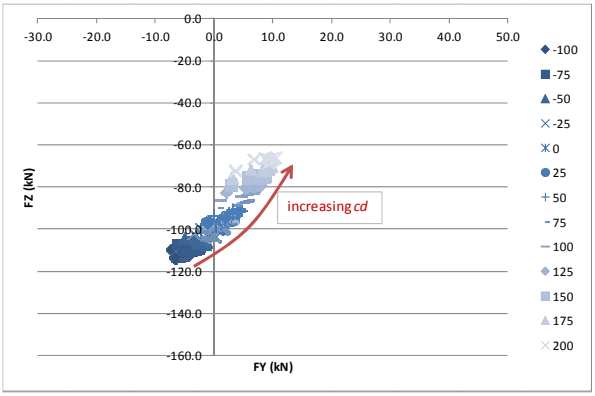

Trailing axle – low rail

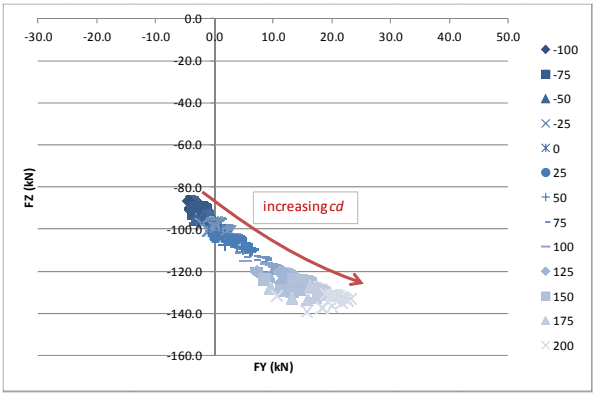

Trailing axle – high rail

Figure 2-3: Wheel-rail contact forces as a function of radius (250m to infinity) and cant deficiency (-100mm to 200mm)

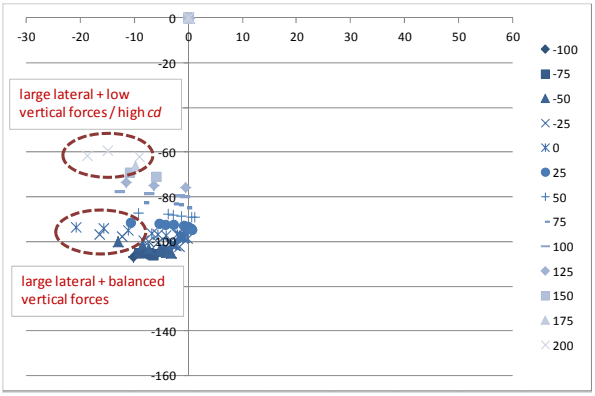

Leading axle - low rail

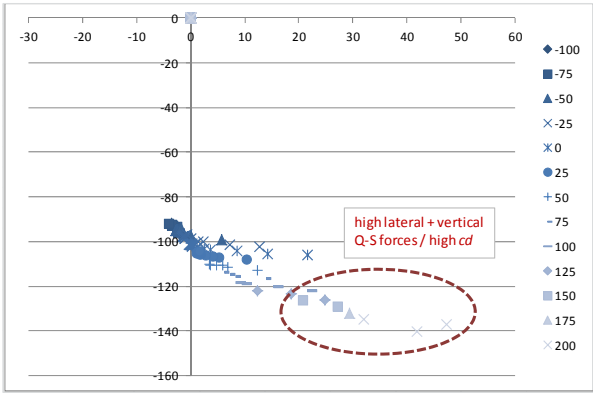

Leading axle - high rail

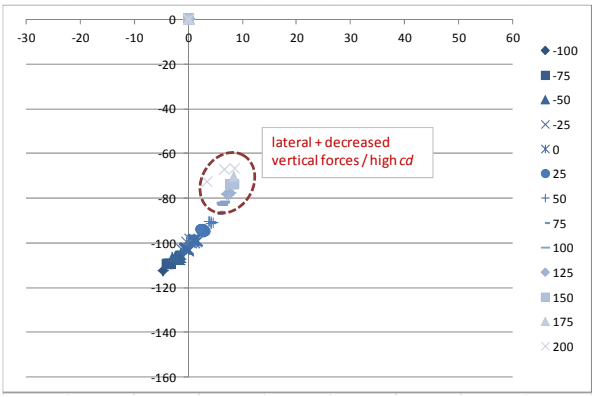

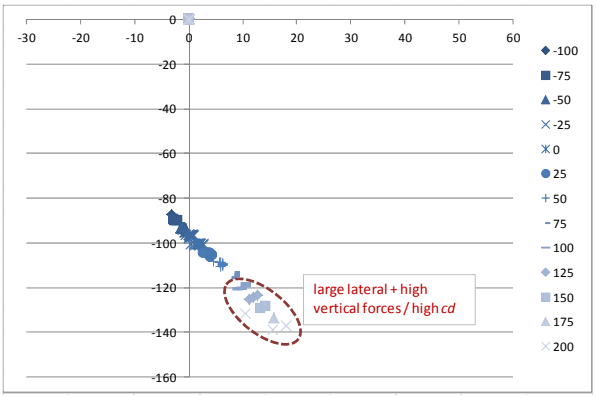

Trailing axle – low rail **Trailing axle – high rail**

Figure 2-4: Wheel-rail contact forces as a function of radius (250m to infinity) and cant deficiency (-100mm to 200mm) filtered for UK routes running conditions at 80% of linespeed

Rows:19_Columns:13_Veh:Y25_Lube:No_Whl:new-P10_Rai:113a_Horizontal:cd_Vertical:cv_Body:FZ WS1_

	-100	-75	-50	-25	0	25	50	75	100	125	150	175	200
250	0	0	0	0	0	0	0	0	0	0	0	0	145
400	0	0	0	0	108	0	0	0	0	0	0	0	146
550	0	0	0	103	106	0	0	0	124	128	132	135	139
700	0	0	99	102	105	109	113	117	121	125	128	0	0
850	0	0	0	100	104	108	111	116	119	123	0	0	0
1000	0	0	97	100	103	107	111	115	118	0	0	0	0
1413	92	94	96	99	102	106	110	114	0	0	0	0	0
2000	0	93	96	99	102	106	110	0	0	0	0	0	0
2500	0	93	96	98	102	106	110	0	0	0	0	0	0
3000	0	93	95	98	102	106	0	0	0	0	0	0	0
3500	0	92	95	98	102	105	0	0	0	0	0	0	0
4000	0	0	95	98	101	105	0	0	0	0	0	0	0
4500	0	0	95	98	101	105	0	0	0	0	0	0	0
5125	0	0	95	98	101	105	0	0	0	0	0	0	0
6000	0	0	95	98	101	105	0	0	0	0	0	0	0
7000	0	0	95	98	101	105	0	0	0	0	0	0	0
8000	0	0	95	98	101	105	0	0	0	0	0	0	0
9000	0	0	95	97	101	105	0	0	0	0	0	0	0
5E+09	0	0	94	97	101	0	0	0	0	0	0	0	0

	-100	-75	-50	-25	0	25	50	75	100	125	150	175	200
250	0	0	0	0	0	0	0	0	0	0	0	0	19
400	0	0	0	0	12	0	0	0	0	0	0	0	17
550	0	0	0	7	8	0	0	0	10	11	12	13	13
700	0	0	3	4	5	6	6	7	8	9	9	0	0
850	0	0	0	1	2	3	4	4	5	6	0	0	0
1000	0	0	0	1	1	2	3	4	4	0	0	0	0
1413	-2	-1	-1	0	1	2	2	3	0	0	0	0	0
2000	0	-2	-1	-1	0	1	2	0	0	0	0	0	0
2500	0	-2	-1	-1	0	1	2	0	0	0	0	0	0
3000	0	-2	-1	-1	0	1	0	0	0	0	0	0	0
3500	0	-2	-2	-1	0	1	0	0	0	0	0	0	0
4000	0	0	-2	-1	0	1	0	0	0	0	0	0	0
4500	0	0	-2	-1	0	1	0	0	0	0	0	0	0
5125	0	0	-2	-1	0	1	0	0	0	0	0	0	0
6000	0	0	-2	-1	0	1	0	0	0	0	0	0	0
7000	0	0	-2	-1	0	1	0	0	0	0	0	0	0
8000	0	0	-1	-1	0	1	0	0	0	0	0	0	0
9000	0	0	-1	-1	0	1	0	0	0	0	0	0	0
5E+09	0	0	-1	0	0	0	0	0	0	0	0	0	0

Rows:19_Columns:13_Veh:Y25_Lube:No_Whl:new-P10_Rai:113a_Horizontal:cd_Vertical:cv_Body:FZ WS1_

	-100	-75	-50	-25	0	25	50	75	100	125	150	175	200
250	0	0	0	0	0	0	0	0	0	0	0	0	64
400	0	0	0	0	96	0	0	0	0	0	0	0	61
550	0	0	0	98	95	0	0	0	79	74	70	67	63
700	0	0	101	99	96	92	88	83	79	75	71	0	0
850	0	0	0	100	96	92	88	83	79	76	0	0	0
1000	0	0	102	100	97	93	88	84	80	0	0	0	0
1413	107	106	103	101	97	93	89	85	0	0	0	0	0
2000	0	106	104	100	97	93	89	0	0	0	0	0	0
2500	0	106	104	101	97	93	89	0	0	0	0	0	0
3000	0	106	104	101	97	94	0	0	0	0	0	0	0
3500	0	107	104	101	98	94	0	0	0	0	0	0	0
4000	0	0	104	101	98	94	0	0	0	0	0	0	0
4500	0	0	104	102	98	94	0	0	0	0	0	0	0
5125	0	0	104	102	98	94	0	0	0	0	0	0	0
6000	0	0	104	102	98	94	0	0	0	0	0	0	0
7000	0	0	105	102	98	95	0	0	0	0	0	0	0
8000	0	0	105	102	98	95	0	0	0	0	0	0	0
9000	0	0	105	102	98	95	0	0	0	0	0	0	0
5E+09	0	0	105	102	99	0	0	0	0	0	0	0	0

	-100	-75	-50	-25	0	25	50	75	100	125	150	175	200
250	0	0	0	0	0	0	0	0	0	0	0	0	-17
400	0	0	0	0	-13	0	0	0	0	0	0	0	-14
550	0	0	0	-10	-9	0	0	0	-9	-9	-9	-8	-8
700	0	0	-7	-7	-7	-7	-6	-6	-5	-5	-5	0	0
850	0	0	0	-5	-4	-3	-2	-2	-1	0	0	0	0
1000	0	0	-5	-4	-3	-3	-2	-1	0	0	0	0	0
1413	-5	-5	-4	-3	-2	-2	-1	0	0	0	0	0	0
2000	0	-4	-3	-2	-1	0	0	0	0	0	0	0	0
2500	0	-4	-3	-2	-1	0	1	0	0	0	0	0	0
3000	0	-3	-3	-2	-1	0	0	0	0	0	0	0	0
3500	0	-3	-3	-2	-1	0	0	0	0	0	0	0	0
4000	0	0	-3	-2	-1	0	0	0	0	0	0	0	0
4500	0	0	-2	-2	-1	0	0	0	0	0	0	0	0
5125	0	0	-2	-1	-1	0	0	0	0	0	0	0	0
6000	0	0	-2	-1	-1	0	0	0	0	0	0	0	0
7000	0	0	-2	-1	-1	0	0	0	0	0	0	0	0
8000	0	0	-2	-1	0	0	0	0	0	0	0	0	0
9000	0	0	-2	-1	0	0	0	0	0	0	0	0	0
5E+09	0	0	-2	-1	0	0	0	0	0	0	0	0	0

Rows:19_Columns:13_Veh:Y25_Lube:No_Whl:new-P10_Rai:113a_Horizontal:cd_Vertical:cv_Body:FZ WS2_

	-100	-75	-50	-25	0	25	50	75	100	125	150	175	200
250	0	0	0	0	0	0	0	0	0	0	0	0	132
400	0	0	0	0	101	0	0	0	0	0	0	0	140
550	0	0	0	98	101	0	0	0	121	126	130	134	138
700	0	0	95	97	101	106	111	116	121	125	129	0	0
850	0	0	0	97	101	105	110	115	120	124	0	0	0
1000	0	0	93	97	101	105	110	114	119	0	0	0	0
1413	87	90	93	97	101	105	109	114	0	0	0	0	0
2000	0	90	94	97	101	105	109	0	0	0	0	0	0
2500	0	90	93	97	101	105	109	0	0	0	0	0	0
3000	0	90	93	97	101	105	0	0	0	0	0	0	0
3500	0	90	93	97	100	105	0	0	0	0	0	0	0
4000	0	0	93	97	101	105	0	0	0	0	0	0	0
4500	0	0	93	97	100	105	0	0	0	0	0	0	0
5125	0	0	93	97	100	105	0	0	0	0	0	0	0
6000	0	0	93	97	100	105	0	0	0	0	0	0	0
7000	0	0	93	97	100	105	0	0	0	0	0	0	0
8000	0	0	93	97	100	105	0	0	0	0	0	0	0
9000	0	0	93	97	100	105	0	0	0	0	0	0	0
5E+09	0	0	93	97	101	0	0	0	0	0	0	0	0

	-100	-75	-50	-25	0	25	50	75	100	125	150	175	200
250	0	0	0	0	0	0	0	0	0	0	0	0	5
400	0	0	0	0	0	0	0	0	0	0	0	0	6
550	0	0	0	0	1	0	0	0	4	5	6	7	8
700	0	0	0	0	1	2	3	4	5	5	6	0	0
850	0	0	0	0	1	2	3	4	5	6	0	0	0
1000	0	0	0	1	2	2	3	4	5	0	0	0	0
1413	-2	-1	0	1	1	2	3	4	0	0	0	0	0
2000	0	-2	-1	0	1	2	3	0	0	0	0	0	0
2500	0	-2	-1	0	1	2	3	0	0	0	0	0	0
3000	0	-2	-1	0	1	2	0	0	0	0	0	0	0
3500	0	-1	-1	0	1	2	0	0	0	0	0	0	0
4000	0	0	-1	0	1	2	0	0	0	0	0	0	0
4500	0	0	-1	0	1	2	0	0	0	0	0	0	0
5125	0	0	-1	0	1	2	0	0	0	0	0	0	0
6000	0	0	-1	0	1	2	0	0	0	0	0	0	0
7000	0	0	-1	0	1	2	0	0	0	0	0	0	0
8000	0	0	-1	0	1	2	0	0	0	0	0	0	0
9000	0	0	-1	0	1	2	0	0	0	0	0	0	0
5E+09	0	0	-1	0	1	0	0	0	0	0	0	0	0

Rows:19_Columns:13_Veh:Y25_Lube:No_Whl:new-P10_Rai:113a_Horizontal:cd_Vertical:cv_Body:FZ WS2_

	-100	-75	-50	-25	0	25	50	75	100	125	150	175	200
250	0	0	0	0	0	0	0	0	0	0	0	0	72
400	0	0	0	0	99	0	0	0	0	0	0	0	67
550	0	0	0	102	100	0	0	0	83	78	75	71	67
700	0	0	105	103	100	95	91	87	82	78	74	0	0
850	0	0	0	104	100	95	92	87	83	79	0	0	0
1000	0	0	107	103	99	95	91	87	83	0	0	0	0
1413	112	110	106	103	99	94	91	87	0	0	0	0	0
2000	0	110	106	103	99	94	90	0	0	0	0	0	0
2500	0	110	106	103	99	94	90	0	0	0	0	0	0
3000	0	110	106	103	99	94	0	0	0	0	0	0	0
3500	0	110	106	103	99	94	0	0	0	0	0	0	0
4000	0	0	106	103	99	94	0	0	0	0	0	0	0
4500	0	0	106	102	99	94	0	0	0	0	0	0	0
5125	0	0	106	102	99	94	0	0	0	0	0	0	0
6000	0	0	106	103	99	94	0	0	0	0	0	0	0
7000	0	0	106	103	99	94	0	0	0	0	0	0	0
8000	0	0	106	103	99	94	0	0	0	0	0	0	0
9000	0	0	106	103	99	94	0	0	0	0	0	0	0
5E+09	0	0	106	103	98	0	0	0	0	0	0	0	0

	-100	-75	-50	-25	0	25	50	75	100	125	150	175	200
250	0	0	0	0	0	0	0	0	0	0	0	0	3
400	0	0	0	0	0	0	0	0	0	0	0	0	6
550	0	0	0	0	0	0	0	0	4	5	6	7	7
700	0	0	-1	0	1	2	3	4	5	6	7	0	0
850	0	0	0	0	1	2	3	4	4	5	0	0	0
1000	0	0	-1	0	1	2	3	4	5	0	0	0	0
1413	-2	-2	-1	0	1	2	3	4	0	0	0	0	0
2000	0	-2	-1	0	1	2	2	0	0	0	0	0	0
2500	0	-2	-1	0	1	2	2	0	0	0	0	0	0
3000	0	-2	-1	0	1	1	0	0	0	0	0	0	0
3500	0	-2	-1	0	1	2	0	0	0	0	0	0	0
4000	0	0	-1	0	1	2	0	0	0	0	0	0	0
4500	0	0	-1	0	1	2	0	0	0	0	0	0	0
5125	0	0	-1	0	1	2	0	0	0	0	0	0	0
6000	0	0	-1	0	1	2	0	0	0	0	0	0	0
7000	0	0	-1	0	1	1	0	0	0	0	0	0	0
8000	0	0	-1	0	1	1	0	0	0	0	0	0	0
9000	0	0	-1	0	0	1	0	0	0	0	0	0	0
5E+09	0	0	-2	-1	0	0	0	0	0	0	0	0	0

Table 2.3: Bqst force magnitude [kN] (left column) and angle to vertical [deg] (right column) for all combined UK routes at 80% line speed. From top to bottom: leading axle high rail, leading axle low rail, trailing axle high rail and trailing axle low rail

Rows:19_Columns:13_Veh:Y25_Lube:No_Whl:new-P10_Rai:113a_Horizontal:cd_Vertical:cv_Body:FZ WS1_Bqst angle to vertical

	-100	-75	-50	-25	0	25	50	75	100	125	150	175	200
250	0	0	0	0	0	0	0	0	0	0	0	0	145.2
400	0	0	0	0	0	112.3	0	0	0	0	0	0	146.2
550	0	0	0	0	106.5	110.3	0	0	0	0	0	0	138.6
700	0	0	0	101.7	104.5	109	113.3	117.4	121.3	124.9	0	131.2	134.3
850	0	0	0	0	103.9	107.6	111.5	115.8	119.4	122.7	125.8	128.4	131.2
1000	0	0	0	99.83	103.1	107	110.9	115	118.5	121.5	124.4	127.1	0
1413	0	0	96.19	98.87	102.2	106.3	110.4	114	116.7	119.7	122.5	0	0
2000	0	0	95.72	98.86	102.3	106	110.4	113.2	116.1	0	0	0	0
2500	0	0	95.53	98.44	102	105.8	109.9	112.8	0	0	0	0	0
3000	0	0	95.26	98.18	101.7	105.6	109.7	0	0	0	0	0	0
3500	0	0	95.25	98.07	101.5	105.5	109.2	0	0	0	0	0	0
4000	0	0	95.11	97.84	101.4	105.2	109.1	0	0	0	0	0	0
4500	0	0	95.05	97.72	101.4	105.3	109	0	0	0	0	0	0
5125	0	0	0	97.66	101.4	105.1	0	0	0	0	0	0	0
6000	0	0	0	97.62	101.3	105.1	0	0	0	0	0	0	0
7000	0	0	0	97.58	101.3	104.9	0	0	0	0	0	0	0
8000	0	0	0	97.55	101.2	104.8	0	0	0	0	0	0	0
9000	0	0	0	97.48	101.2	104.8	0	0	0	0	0	0	0
5E+09	0	0	93.84	97.04	100.8	104.4	0	0	0	0	0	0	0

	-100	-75	-50	-25	0	25	50	75	100	125	150	175	200
250	0	0	0	0	0	0	0	0	0	0	0	0	19
400	0	0	0	0	0	12	0	0	0	0	0	0	17
550	0	0	0	0	8	8	0	0	0	0	0	0	13
700	0	0	0	4	5	6	6	7	8	9	0	10	11
850	0	0	0	0	2	3	4	4	5	6	6	7	8
1000	0	0	0	1	1	2	3	4	4	5	6	6	0
1413	0	0	-1	0	1	2	2	3	4	5	5	0	0
2000	0	0	-1	-1	0	1	2	3	3	0	0	0	0
2500	0	0	-1	-1	0	1	2	3	0	0	0	0	0
3000	0	0	-1	-1	0	1	2	0	0	0	0	0	0
3500	0	0	-2	-1	0	1	2	0	0	0	0	0	0
4000	0	0	-2	-1	0	1	2	0	0	0	0	0	0
4500	0	0	-2	-1	0	1	2	0	0	0	0	0	0
5125	0	0	0	-1	0	1	0	0	0	0	0	0	0
6000	0	0	0	-1	0	1	0	0	0	0	0	0	0
7000	0	0	0	-1	0	1	0	0	0	0	0	0	0
8000	0	0	0	-1	0	1	0	0	0	0	0	0	0
9000	0	0	0	-1	0	1	0	0	0	0	0	0	0
5E+09	0	0	-1	0	0	1	0	0	0	0	0	0	0

Rows:19_Columns:13_Veh:Y25_Lube:No_Whl:new-P10_Rai:113a_Horizontal:cd_Vertical:cv_Body:FZ WS1_Bqst angle to vertical

	-100	-75	-50	-25	0	25	50	75	100	125	150	175	200
250	0	0	0	0	0	0	0	0	0	0	0	0	64.49
400	0	0	0	0	0	92.33	0	0	0	0	0	0	61.21
550	0	0	0	0	95.31	91.91	0	0	0	0	0	0	62.87
700	0	0	0	98.61	95.63	92.29	87.5	83.12	78.91	75	0	68	64.57
850	0	0	0	0	96.48	92.32	87.75	83.18	79.36	75.82	72.48	69.41	66.38
1000	0	0	0	100.2	96.81	92.65	88.08	83.63	79.89	76.67	73.66	70.7	0
1413	0	0	103.3	100.6	97.16	92.91	88.82	84.94	81.27	78.31	75.56	0	0
2000	0	0	103.5	100.5	96.97	93.17	88.92	85.57	82.18	0	0	0	0
2500	0	0	103.7	100.9	97.19	93.41	89.26	85.93	0	0	0	0	0
3000	0	0	104	101	97.47	93.71	89.55	0	0	0	0	0	0
3500	0	0	104.1	101.2	97.75	93.97	90.01	0	0	0	0	0	0
4000	0	0	104.2	101.4	97.85	94.25	90.1	0	0	0	0	0	0
4500	0	0	104.2	101.5	97.9	94.22	90.23	0	0	0	0	0	0
5125	0	0	0	101.6	97.96	94.41	0	0	0	0	0	0	0
6000	0	0	0	101.6	97.99	94.48	0	0	0	0	0	0	0
7000	0	0	0	101.7	98.04	94.69	0	0	0	0	0	0	0
8000	0	0	0	101.7	98.14	94.72	0	0	0	0	0	0	0
9000	0	0	0	101.8	98.15	94.77	0	0	0	0	0	0	0
5E+09	0	0	105.2	102.2	98.53	95.15	0	0	0	0	0	0	0

	-100	-75	-50	-25	0	25	50	75	100	125	150	175	200
250	0	0	0	0	0	0	0	0	0	0	0	0	-17
400	0	0	0	0	0	-13	0	0	0	0	0	0	-14
550	0	0	0	0	-9	-9	0	0	0	0	0	0	-8
700	0	0	0	-7	-7	-7	-6	-6	-5	-5	0	-4	-4
850	0	0	0	0	-4	-3	-2	-2	-1	0	0	1	1
1000	0	0	0	-4	-3	-3	-2	-1	0	1	1	2	0
1413	0	0	-4	-3	-2	-2	-1	0	1	1	2	0	0
2000	0	0	-3	-2	-1	0	0	1	2	0	0	0	0
2500	0	0	-3	-2	-1	0	1	1	0	0	0	0	0
3000	0	0	-3	-2	-1	0	1	0	0	0	0	0	0
3500	0	0	-3	-2	-1	0	1	0	0	0	0	0	0
4000	0	0	-3	-2	-1	0	1	0	0	0	0	0	0
4500	0	0	-2	-2	-1	0	1	0	0	0	0	0	0
5125	0	0	0	-1	-1	0	0	0	0	0	0	0	0
6000	0	0	0	-1	-1	0	0	0	0	0	0	0	0
7000	0	0	0	-1	-1	0	0	0	0	0	0	0	0
8000	0	0	0	-1	0	0	0	0	0	0	0	0	0
9000	0	0	0	-1	0	0	0	0	0	0	0	0	0
5E+09	0	0	-2	-1	0	1	0	0	0	0	0	0	0

Rows:19_Columns:13_Veh:Y25_Lube:No_Whl:new-P10_Rai:113a_Horizontal:cd_Vertical:cv_Body:FZ WS2_Bqst angle to vertical

	-100	-75	-50	-25	0	25	50	75	100	125	150	175	200
250	0	0	0	0	0	0	0	0	0	0	0	0	131.8
400	0	0	0	0	0	104.4	0	0	0	0	0	0	139.7
550	0	0	0	0	100.8	104.9	0	0	0	0	0	0	138.4
700	0	0	0	97.4	100.7	106.3	110.7	115.8	120.7	125	0	133.5	137.5
850	0	0	0	0	100.8	105.5	110	114.8	119.5	123.8	127.9	132.2	136.4
1000	0	0	0	96.86	100.8	105.5	109.9	114.4	119	123.3	127.4	131.6	0
1413	0	0	93.48	96.78	100.7	105.4	109.3	113.6	118.4	122.4	126.5	0	0
2000	0	0	93.56	96.68	100.6	105.1	108.9	113.4	117.8	0	0	0	0
2500	0	0	93.23	96.66	100.6	104.9	108.8	113.1	0	0	0	0	0
3000	0	0	93.22	96.62	100.6	104.8	108.7	0	0	0	0	0	0
3500	0	0	93.2	96.55	100.5	104.7	108.9	0	0	0	0	0	0
4000	0	0	93.24	96.67	100.6	104.8	108.8	0	0	0	0	0	0
4500	0	0	93.17	96.71	100.5	104.6	108.7	0	0	0	0	0	0
5125	0	0	0	96.68	100.5	104.6	0	0	0	0	0	0	0
6000	0	0	0	96.62	100.5	104.6	0	0	0	0	0	0	0
7000	0	0	0	96.57	100.4	104.6	0	0	0	0	0	0	0
8000	0	0	0	96.54	100.5	104.5	0	0	0	0	0	0	0
9000	0	0	0	96.54	100.5	104.5	0	0	0	0	0	0	0
5E+09	0	0	92.91	96.53	100.5	104.5	0	0	0	0	0	0	0

	-100	-75	-50	-25	0	25	50	75	100	125	150	175	200
250	0	0	0	0	0	0	0	0	0	0	0	0	5
400	0	0	0	0	0	1	0	0	0	0	0	0	6
550	0	0	0	0	1	2	0	0	0	0	0	0	8
700	0	0	0	0	1	2	3	4	5	5	0	7	8
850	0	0	0	0	1	2	3	4	5	6	7	8	9
1000	0	0	0	1	2	2	3	4	5	6	7	8	0
1413	0	0	0	1	1	2	3	4	5	6	7	0	0
2000	0	0	-1	0	1	2	3	4	5	0	0	0	0
2500	0	0	-1	0	1	2	3	4	0	0	0	0	0
3000	0	0	-1	0	1	2	3	0	0	0	0	0	0
3500	0	0	-1	0	1	2	3	0	0	0	0	0	0
4000	0	0	-1	0	1	2	3	0	0	0	0	0	0
4500	0	0	-1	0	1	2	3	0	0	0	0	0	0
5125	0	0	0	0	1	2	0	0	0	0	0	0	0
6000	0	0	0	0	1	2	0	0	0	0	0	0	0
7000	0	0	0	0	1	2	0	0	0	0	0	0	0
8000	0	0	0	0	1	2	0	0	0	0	0	0	0
9000	0	0	0	0	1	2	0	0	0	0	0	0	0
5E+09	0	0	-1	0	1	2	0	0	0	0	0	0	0

Rows:19_Columns:13_Veh:Y25_Lube:No_Whl:new-P10_Rai:113a_Horizontal:cd_Vertical:cv_Body:FZ WS2_Bqst angle to vertical

	-100	-75	-50	-25	0	25	50	75	100	125	150	175	200
250	0	0	0	0	0	0	0	0	0	0	0	0	72.48
400	0	0	0	0	0	95.88	0	0	0	0	0	0	67.35
550	0	0	0	0	99.92	95.94	0	0	0	0	0	0	67.02
700	0	0	0	103	100	95.12	91.17	86.54	81.93	78.17	0	70.67	67.1
850	0	0	0	0	99.54	95.35	91.54	87.11	82.66	78.74	75	71.18	67.28
1000	0	0	0	103.2	99.32	94.89	91.21	87.12	82.94	78.91	74.99	71.06	0
1413	0	0	106.2	102.9	99.07	94.48	90.61	86.71	82.98	79.02	74.98	0	0
2000	0	0	106	102.7	98.89	94.41	90.41	86.58	82.84	0	0	0	0
2500	0	0	106.1	102.6	98.85	94.4	90.5	86.75	0	0	0	0	0
3000	0	0	106.1	102.6	98.72	94.34	90.53	0	0	0	0	0	0
3500	0	0	105.9	102.6	98.69	94.27	90.28	0	0	0	0	0	0
4000	0	0	105.9	102.5	98.64	94.13	90.34	0	0	0	0	0	0
4500	0	0	106	102.5	98.64	94.28	90.4	0	0	0	0	0	0
5125	0	0	0	102.5	98.59	94.18	0	0	0	0	0	0	0
6000	0	0	0	102.5	98.59	94.21	0	0	0	0	0	0	0
7000	0	0	0	102.5	98.58	94.17	0	0	0	0	0	0	0
8000	0	0	0	102.6	98.53	94.2	0	0	0	0	0	0	0
9000	0	0	0	102.6	98.56	94.22	0	0	0	0	0	0	0
5E+09	0	0	106.4	102.6	98.4	94.21	0	0	0	0	0	0	0

	-100	-75	-50	-25	0	25	50	75	100	125	150	175	200
250	0	0	0	0	0	0	0	0	0	0	0	0	3
400	0	0	0	0	0	1	0	0	0	0	0	0	6
550	0	0	0	0	0	1	0	0	0	0	0	0	7
700	0	0	0	0	1	2	3	4	5	6	0	7	8
850	0	0	0	0	1	2	3	4	4	5	6	7	8
1000	0	0	0	0	1	2	3	4	5	5	6	7	0
1413	0	0	-1	0	1	2	3	4	5	6	7	0	0
2000	0	0	-1	0	1	2	2	4	5	0	0	0	0
2500	0	0	-1	0	1	2	2	3	0	0	0	0	0
3000	0	0	-1	0	1	1	2	0	0	0	0	0	0
3500	0	0	-1	0	1	2	3	0	0	0	0	0	0
4000	0	0	-1	0	1	2	3	0	0	0	0	0	0
4500	0	0	-1	0	1	2	3	0	0	0	0	0	0
5125	0	0	0	0	1	2	0	0	0	0	0	0	0
6000	0	0	0	0	1	2	0	0	0	0	0	0	0
7000	0	0	0	0	1	1	0	0	0	0	0	0	0
8000	0	0	0	0	1	1	0	0	0	0	0	0	0
9000	0	0	0	0	1	1	0	0	0	0	0	0	0
5E+09	0	0	-2	-1	0	1	0	0	0	0	0	0	0

Table 2.4: Bqst force magnitude [kN] (left column) and angle to vertical [deg] (right column) for all combined UK routes at 100% line speed. From top to bottom: leading axle high rail, leading axle low rail, trailing axle high rail and trailing axle low rail

Rows:19_Columns:13_Veh:Y25_Lube:No_Whl:new-P10_Rai:113a_Horizontal:cd_Vertical:cv_Body:FZ WS1_Bqst angle to vertical

	-100	-75	-50	-25	0	25	50	75	100	125	150	175	200
250	0	0	0	0	0	0	0	0	0	0	0	0	145.2
400	0	0	0	0	0	0	116.9	0	0	0	0	0	146.2
550	0	0	0	0	0	110.3	114.4	118.9	0	0	0	0	138.6
700	0	0	0	0	104.5	109	113.3	117.4	121.3	0	128.1	131.2	134.3
850	0	0	0	0	103.9	107.6	111.5	115.8	119.4	122.7	125.8	128.4	131.2
1000	0	0	0	0	103.1	0	110.9	115	118.5	121.5	124.4	127.1	129.7
1413	0	0	0	0	102.2	106.3	110.4	114	116.7	119.7	122.5	125.1	128
2000	0	0	0	0	102.3	106	110.4	113.2	116.1	118.7	0	0	0
2500	0	0	0	0	102	105.8	109.9	112.8	115.4	0	0	0	0
3000	0	0	0	98.18	101.7	105.6	109.7	112.4	0	0	0	0	0
3500	0	0	0	98.07	101.5	105.5	109.2	111.8	0	0	0	0	0
4000	0	0	0	97.84	101.4	105.2	109.1	111.7	0	0	0	0	0
4500	0	0	0	97.72	101.4	105.3	109	0	0	0	0	0	0
5125	0	0	0	97.66	101.4	105.1	108.8	0	0	0	0	0	0
6000	0	0	0	97.62	101.3	105.1	108.6	0	0	0	0	0	0
7000	0	0	0	97.58	101.3	104.9	108.6	0	0	0	0	0	0
8000	0	0	0	97.55	101.2	104.8	0	0	0	0	0	0	0
9000	0	0	0	97.48	101.2	104.8	0	0	0	0	0	0	0
5E+09	0	0	93.84	97.04	100.8	104.4	0	0	0	0	0	0	0
	0	0	0	0	0	0	0	0	0	0	0	0	0

	-100	-75	-50	-25	0	25	50	75	100	125	150	175	200
250	0	0	0	0	0	0	0	0	0	0	0	0	19
400	0	0	0	0	0	0	13	0	0	0	0	0	17
550	0	0	0	0	8	9	10	0	0	0	0	0	13
700	0	0	0	5	6	6	7	8	0	9	10	11	
850	0	0	0	2	3	4	4	5	6	6	7	8	
1000	0	0	0	1	0	3	4	4	5	6	6	7	
1413	0	0	0	1	2	2	3	4	5	5	6	6	
2000	0	0	0	0	1	2	3	3	4	0	0	0	
2500	0	0	0	0	1	2	3	3	0	0	0	0	
3000	0	0	-1	0	1	2	3	0	0	0	0	0	
3500	0	0	-1	0	1	2	2	0	0	0	0	0	
4000	0	0	-1	0	1	2	2	0	0	0	0	0	
4500	0	0	-1	0	1	2	0	0	0	0	0	0	
5125	0	0	-1	0	1	2	0	0	0	0	0	0	
6000	0	0	-1	0	1	2	0	0	0	0	0	0	
7000	0	0	-1	0	1	2	0	0	0	0	0	0	
8000	0	0	-1	0	1	0	0	0	0	0	0	0	
9000	0	0	-1	0	1	0	0	0	0	0	0	0	
5E+09	0	0	-1	0	0	1	0	0	0	0	0	0	0

Rows:19_Columns:13_Veh:Y25_Lube:No_Whl:new-P10_Rai:113a_Horizontal:cd_Vertical:cv_Body:FZ WS1_Bqst angle to vertical

	-100	-75	-50	-25	0	25	75	100	125	150	175	200
250	0	0	0	0	0	0	0	0	0	0	0	64.49
400	0	0	0	0	0	0	88.43	0	0	0	0	61.21
550	0	0	0	0	0	91.91	87.77	83.65	0	0	0	62.87
700	0	0	0	0	95.63	92.29	87.5	83.12	78.91	0	71.43	68
850	0	0	0	0	96.48	92.32	87.75	83.18	79.36	75.82	72.48	69.41
1000	0	0	0	0	96.81	0	88.08	83.63	79.89	76.67	73.66	70.7
1413	0	0	0	0	97.16	92.91	88.82	84.94	81.27	78.31	75.56	72.75
2000	0	0	0	0	96.97	93.17	88.92	85.57	82.18	79.26	0	0
2500	0	0	0	0	97.19	93.41	89.26	85.93	82.82	0	0	0
3000	0	0	0	101	97.47	93.71	89.55	86.28	0	0	0	0
3500	0	0	0	101.2	97.75	93.97	90.01	86.68	0	0	0	0
4000	0	0	0	101.4	97.85	94.25	90.1	86.82	0	0	0	0
4500	0	0	0	101.5	97.9	94.22	90.23	0	0	0	0	0
5125	0	0	0	101.6	97.96	94.41	90.34	0	0	0	0	0
6000	0	0	0	101.6	97.99	94.48	90.52	0	0	0	0	0
7000	0	0	0	101.7	98.04	94.69	90.58	0	0	0	0	0
8000	0	0	0	101.7	98.14	94.72	0	0	0	0	0	0
9000	0	0	0	101.8	98.15	94.77	0	0	0	0	0	0
5E+09	0	0	105.2	102.2	98.53	95.15	0	0	0	0	0	0

	-100	-75	-50	-25	0	25	50	75	100	125	150	175	200
250	0	0	0	0	0	0	0	0	0	0	0	0	-17
400	0	0	0	0	0	0	-13	0	0	0	0	0	-14
550	0	0	0	0	-9	-9	-9	0	0	0	0	0	-8
700	0	0	0	-7	-7	-6	-6	-5	0	-5	-4	-4	
850	0	0	0	-4	-3	-2	-2	-1	0	0	1	1	
1000	0	0	0	-3	0	-2	-1	0	1	1	2	2	
1413	0	0	0	-2	-2	-1	0	1	1	2	3	4	
2000	0	0	0	-1	0	0	1	2	3	0	0	0	
2500	0	0	0	-1	0	1	1	2	0	0	0	0	
3000	0	0	-2	-1	0	1	2	0	0	0	0	0	
3500	0	0	-2	-1	0	1	2	0	0	0	0	0	
4000	0	0	-2	-1	0	1	2	0	0	0	0	0	
4500	0	0	-2	-1	0	1	0	0	0	0	0	0	
5125	0	0	-1	-1	0	1	0	0	0	0	0	0	
6000	0	0	-1	-1	0	1	0	0	0	0	0	0	
7000	0	0	-1	-1	0	1	0	0	0	0	0	0	
8000	0	0	-1	0	0	0	0	0	0	0	0	0	
9000	0	0	-1	0	0	0	0	0	0	0	0	0	
5E+09	0	0	-2	-1	0	1	0	0	0	0	0	0	0

Rows:19_Columns:13_Veh:Y25_Lube:No_Whl:new-P10_Rai:113a_Horizontal:cd_Vertical:cv_Body:FZ WS2_Bqst angle to vertical

	-100	-75	-50	-25	0	25	50	75	100	125	150	175	200
250	0	0	0	0	0	0	0	0	0	0	0	0	131.8
400	0	0	0	0	0	0	108.2	0	0	0	0	0	139.7
550	0	0	0	0	0	104.9	109.4	114.5	0	0	0	0	138.4
700	0	0	0	0	100.7	106.3	110.7	115.8	120.7	0	129.3	133.5	137.5
850	0	0	0	0	100.8	105.5	110	114.8	119.5	123.8	127.9	132.2	136.4
1000	0	0	0	0	100.8	0	109.9	114.4	119	123.3	127.4	131.6	135.9
1413	0	0	0	0	100.7	105.4	109.3	113.6	118.4	122.4	126.5	130.8	135
2000	0	0	0	0	100.6	105.1	108.9	113.4	117.8	121.8	0	0	0
2500	0	0	0	0	100.6	104.9	108.8	113.1	117.6	0	0	0	0
3000	0	0	0	96.62	100.6	104.8	108.7	113	0	0	0	0	0
3500	0	0	0	96.55	100.5	104.7	108.9	113.5	0	0	0	0	0
4000	0	0	0	96.67	100.6	104.8	108.8	113.3	0	0	0	0	0
4500	0	0	0	96.71	100.5	104.6	108.7	0	0	0	0	0	0
5125	0	0	0	96.68	100.5	104.6	108.7	0	0	0	0	0	0
6000	0	0	0	96.62	100.5	104.6	108.6	0	0	0	0	0	0
7000	0	0	0	96.57	100.4	104.6	108.5	0	0	0	0	0	0
8000	0	0	0	96.54	100.5	104.5	0	0	0	0	0	0	0
9000	0	0	0	96.54	100.5	104.5	0	0	0	0	0	0	0
5E+09	0	0	92.91	96.53	100.5	104.5	0	0	0	0	0	0	0

	-100	-75	-50	-25	0	25	50	75	100	125	150	175	200
250	0	0	0	0	0	0	0	0	0	0	0	0	5
400	0	0	0	0	0	0	2	0	0	0	0	0	6
550	0	0	0	0	0	2	2	3	0	0	0	0	8
700	0	0	0	0	1	2	3	4	5	0	6	7	8
850	0	0	0	0	1	2	3	4	5	6	7	8	9
1000	0	0	0	0	2	0	3	4	5	6	7	8	10
1413	0	0	0	0	1	2	3	4	5	6	7	9	10
2000	0	0	0	0	1	2	3	4	5	6	0	0	0
2500	0	0	0	0	1	2	3	4	5	0	0	0	0
3000	0	0	0	0	1	2	3	4	0	0	0	0	0
3500	0	0	0	0	1	2	3	4	0	0	0	0	0
4000	0	0	0	0	1	2	3	4	0	0	0	0	0
4500	0	0	0	0	1	2	3	0	0	0	0	0	0
5125	0	0	0	0	1	2	3	0	0	0	0	0	0
6000	0	0	0	0	1	2	3	0	0	0	0	0	0
7000	0	0	0	0	1	2	3	0	0	0	0	0	0
8000	0	0	0	0	1	2	0	0	0	0	0	0	0
9000	0	0	0	0	1	2	0	0	0	0	0	0	0
5E+09	0	0	-1	0	1	2	0	0	0	0	0	0	0

Rows:19_Columns:13_Veh:Y25_Lube:No_Whl:new-P10_Rai:113a_Horizontal:cd_Vertical:cv_Body:FZ WS2_Bqst angle to vertical

	-100	-75	-50	-25	0	25	50	75	100	125	150	175	200
250	0	0	0	0	0	0	0	0	0	0	0	0	72.48
400	0	0	0	0	0	0	92	0	0	0	0	0	67.35
550	0	0	0	0	0	95.94	92.13	87.55	0	0	0	0	67.02
700	0	0	0	0	100	95.12	91.17	86.54	81.93	0	74.45	70.67	67.1
850	0	0	0	0	99.54	95.35	91.54	87.11	82.66	78.74	75	71.18	67.28
1000	0	0	0	0	99.32	0	91.21	87.12	82.94	78.91	74.99	71.06	67.15
1413	0	0	0	0	99.07	94.48	90.61	86.71	82.98	79.02	74.98	70.83	66.91
2000	0	0	0	0	98.89	94.41	90.41	86.58	82.84	79.16	0	0	0
2500	0	0	0	0	98.85	94.4	90.5	86.75	82.87	0	0	0	0
3000	0	0	0	102.6	98.72	94.34	90.53	86.79	0	0	0	0	0
3500	0	0	0	102.6	98.69	94.27	90.28	86.5	0	0	0	0	0
4000	0	0	0	102.5	98.64	94.13	90.34	86.61	0	0	0	0	0
4500	0	0	0	102.5	98.64	94.28	90.4	0	0	0	0	0	0
5125	0	0	0	102.5	98.59	94.18	90.45	0	0	0	0	0	0
6000	0	0	0	102.5	98.59	94.21	90.51	0	0	0	0	0	0
7000	0	0	0	102.5	98.58	94.17	90.57	0	0	0	0	0	0
8000	0	0	0	102.6	98.53	94.2	0	0	0	0	0	0	0
9000	0	0	0	102.6	98.56	94.22	0	0	0	0	0	0	0
5E+09	0	0	106.4	102.6	98.4	94.21	0	0	0	0	0	0	0

	-100	-75	-50	-25	0	25	50	75	100	125	150	175	200
250	0	0	0	0	0	0	0	0	0	0	0	0	3
400	0	0	0	0	0	0	1	0	0	0	0	0	6
550	0	0	0	0	1	2	3	0	0	0	0	0	7
700	0	0	0	1	2	3	4	5	0	7	7	7	8
850	0	0	0	1	2	3	4	4	5	6	7	7	8
1000	0	0	0	1	0	3	4	5	5	6	7	7	8
1413	0	0	0	1	2	3	4	5	6	7	8	8	
2000	0	0	0	1	2	2	4	5	6	0	0	0	
2500	0	0	0	1	2	2	3	4	0	0	0	0	
3000	0	0	0	1	1	2	3	0	0	0	0	0	
3500	0	0	0	1	2	3	4	0	0	0	0	0	
4000	0	0	0	1	2	3	4	0	0	0	0	0	
4500	0	0	0	1	2	3	0	0	0	0	0	0	
5125	0	0	0	1	2	3	0	0	0	0	0	0	
6000	0	0	0	1	2	2	0	0	0	0	0	0	
7000	0	0	0	1	1	2	0	0	0	0	0	0	
8000	0	0	0	1	1	0	0	0	0	0	0	0	
9000	0	0	0	0	1	0	0	0	0	0	0	0	
5E+09	0	0	-2	-1	0	1	0	0	0	0	0	0	0

Table 2.5: Bqst force magnitude [kN] (left column) and angle to vertical [deg] (right column) for all combined UK routes at 120% line speed. From top to bottom: leading axle high rail, leading axle low rail, trailing axle high rail and trailing axle low rail

2.1.4.2 Noticeable behaviour of the B_{qst} forces

Running in cant excess: in all radius curves the low rail sees an increased force of about 106kN (trailing axle) and the high rail sees a reduced force of about 93kN (trailing axle) - +/- 6%.

Running in cant deficiency: the force increases on the high rail under the leading wheel and decreases on the low rail in a linear manner as shown in Figure 2-5. The maximum observed on the high rail under **extreme cant deficiency (200mm)** is around **145kN** with an angle of **19 degrees**. Note that for the case of Network Rail the maximum designed permissible cant deficiency is 110mm on continuously welded track and 150mm exceptional value. Extreme values highlighted here may be due to local alignment and cross level deviations. For **typical maximum design cant deficiency**, the **maximum force** would be around **126kN** (R=850, cd=150) with an angle of about **6 to 8 degrees**. This increase of forces could be typical of a vehicle running at optimum linespeed.

Running in tighter radius: Figure 2-6 shows the B_{qst} forces and angle as the radius decreases for all cant deficiencies. Forces above the nominal wheel load line are forces on the high rail. For radii above ~1200m the forces are predominantly affected by cant deficiency and have a low dependency on curve radius. As the radius tightens, the cornering forces increase/decrease significantly on the high/low rails following a logarithmic trend. The 'hotspot' loads are clearly identified for largest cant deficiency and tightest radius combination.

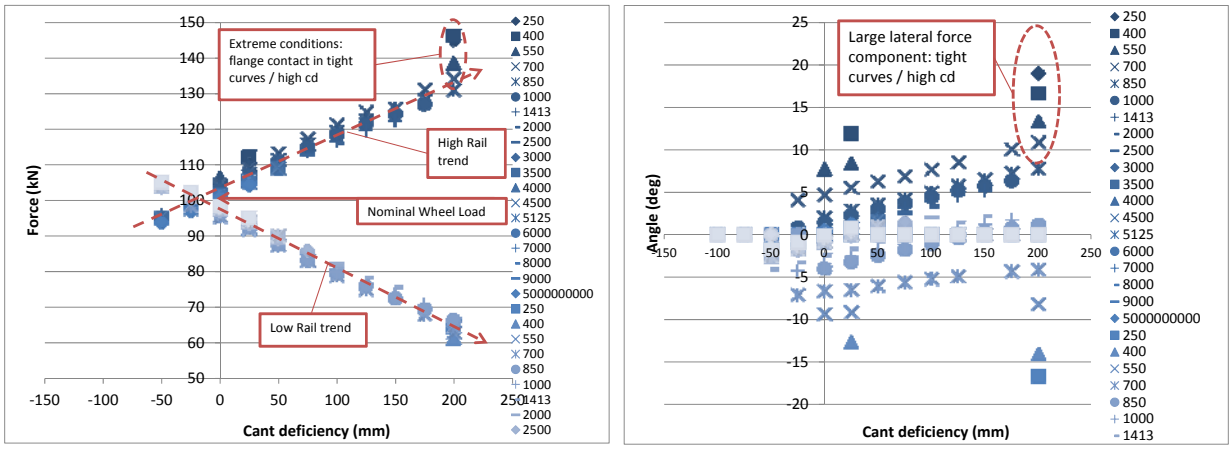

Figure 2-5: change in Bqst magnitude (left) and direction (right) under the leading axle as a function of cant deficiency for all radii

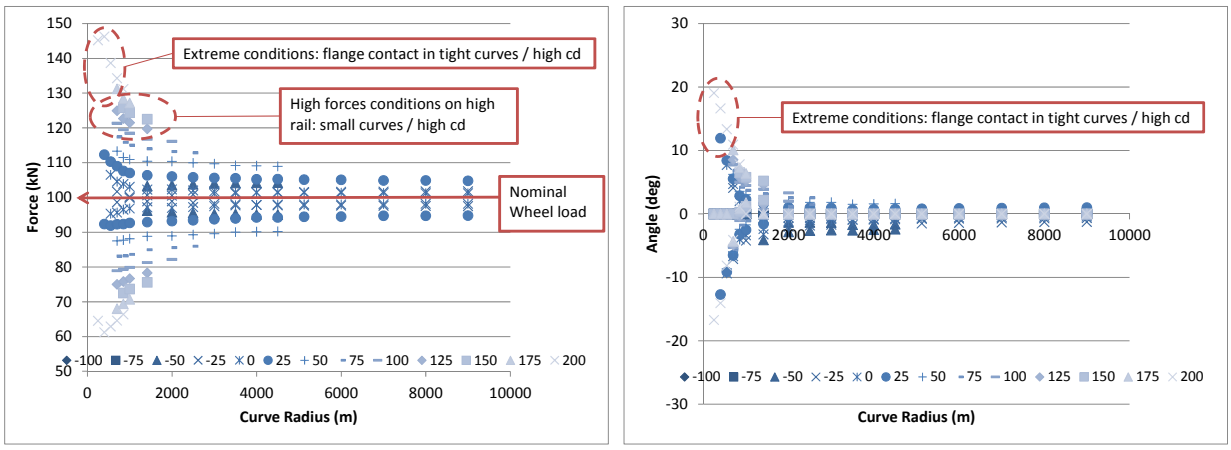

Figure 2-6: change in Bqst forces under the leading axle as a function of curve radius for all cant deficiencies

2.1.5 Track quality effect on medium frequency (<20Hz) vertical dynamic forces

Quasi-static force predictions depend on long wavelength track input and vehicle running cant deficiency. Additionally, the short wavelength track irregularities in the range [3-25m] also produce increased dynamic forces at the wheel rail contact, which have to be considered in addition to the above for fatigue of the track components and track degradation.

Results from WP2 simulations are used to characterise the freight vehicle dynamic force as a function of the track quality. To achieve this, the input signal (vertical rail irregularities) and the output (vertical wheel force) are split into 200m sections and standard deviations are calculated. Plotting one against the other indicates the typical dynamic reaction of the vehicle in different loading conditions and different speeds on the UK routes.

2.1.5.1 Track quality assessment

For reference the vertical left and right rail signals of the Vampire input file, filtered with a 4th order Butterworth bandpass (3 to 25m) filter have been used to calculate the standard deviation for every 200m sections (Figure 2-7), and a distribution plotted for all four routes as well as the cumulative of all routes (Figure 2-8).

The cumulative distribution for the all UK routes have been plotted in Figure 2-9 and compared with the EN13484 quality band representative of EU track conditions for the speed range up to 120km/h. All tracks apart from route number 2 are compliant with the EN standard values and they all have an overall good quality distribution. The cumulative data of all routes is also compliant and therefore constitute of good reference case for European mixed traffic corridor.

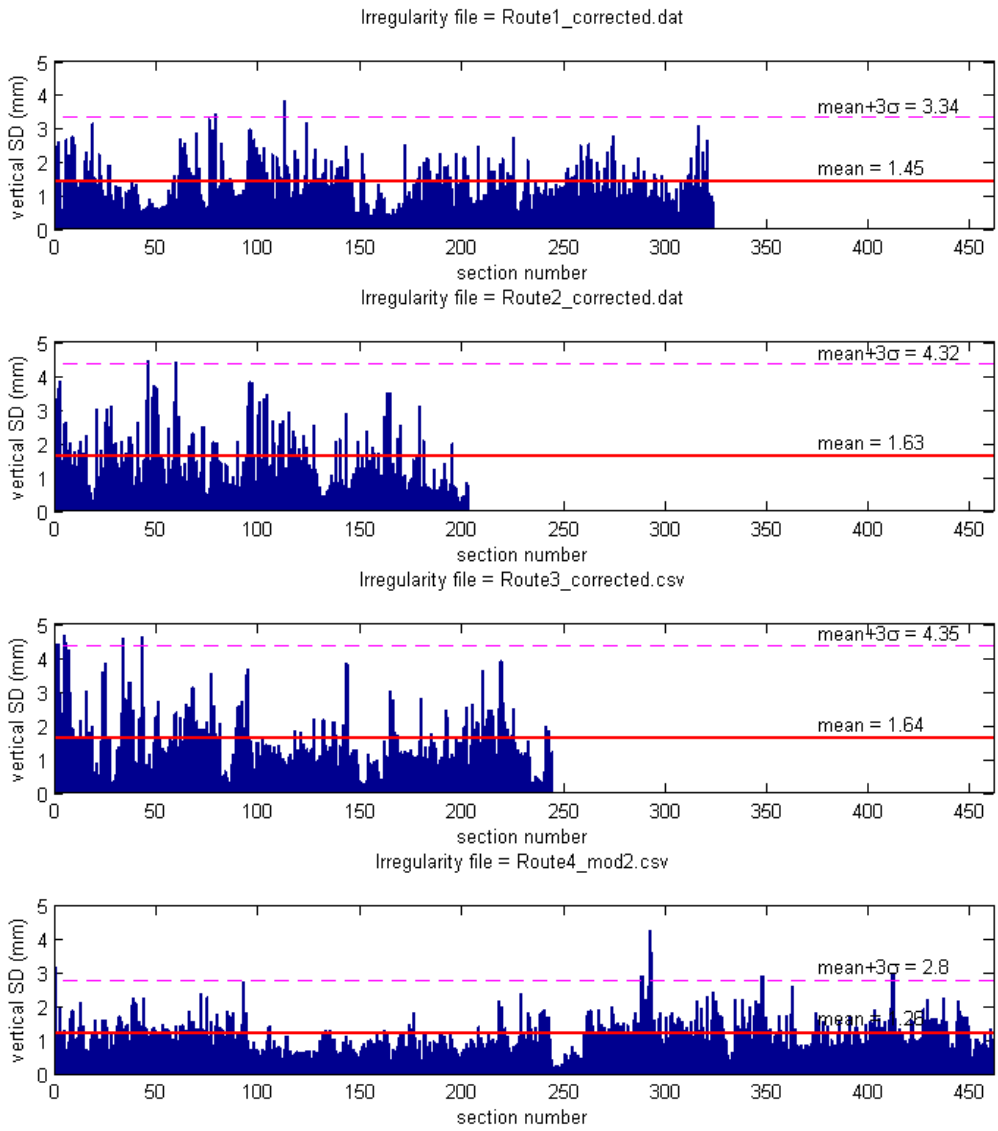

Figure 2-7: Four UK track horizontal level quality (max SD of left or right rail) over 200m sections, showing mean value of SDs as well as mean + 3 sigma standard deviation

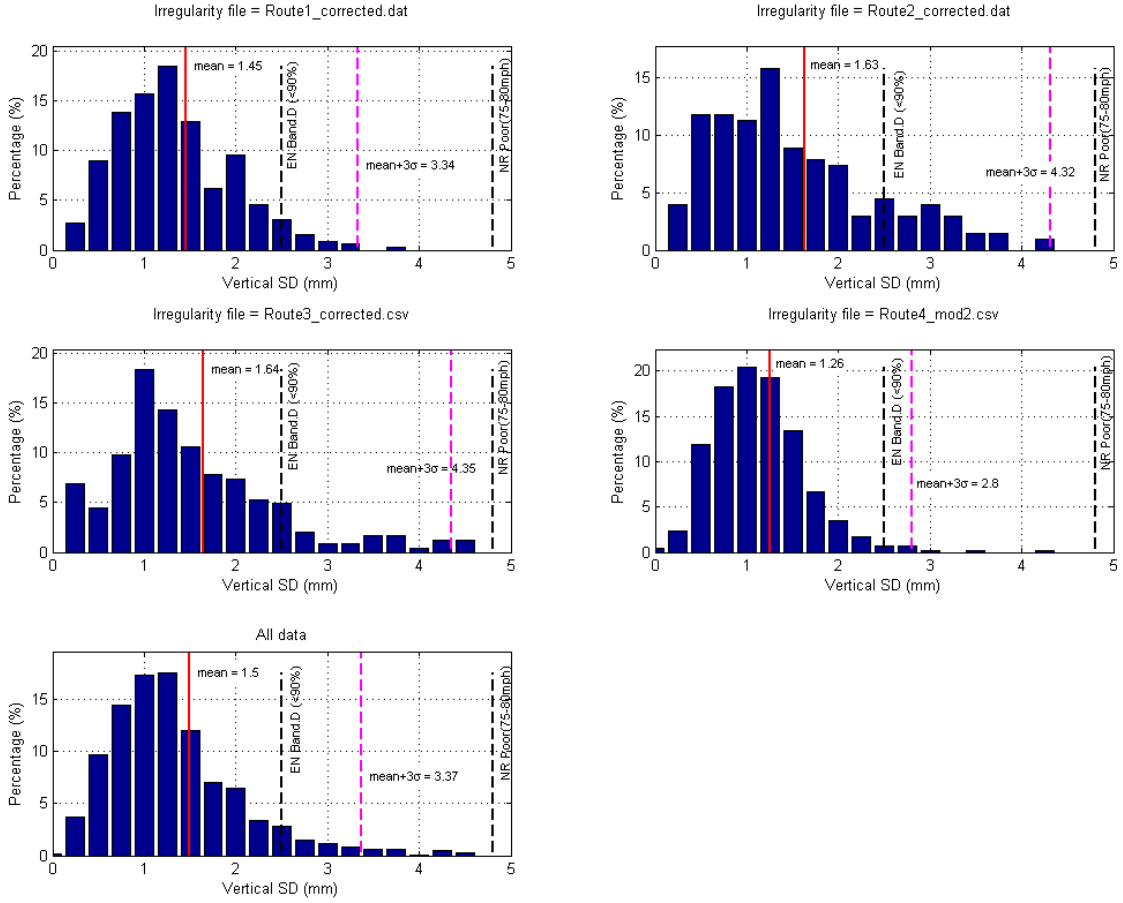

Figure 2-8: Four UK track horizontal level quality distribution (max SD of left or right rail) over 200m sections as a percentage of the route, also showing the mean value of SDs, the EN13484 Quality Band D limit for speed in the range 80 to 120km/h, mean + 3 sigma standard deviation of SD values and Network Rail Poor quality band for speed range 75-80mph.

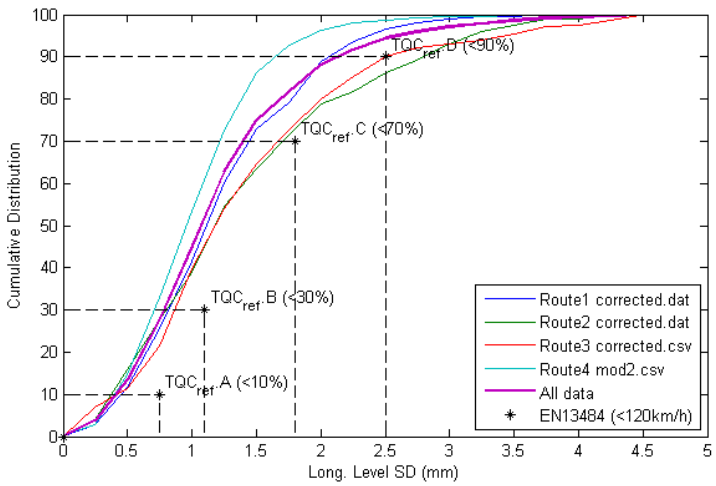

Figure 2-9:UK track quality cumulative distribution compared to EU standard EN13484 quality bands

Results of vertical dynamic force (standard deviation) against track quality are presented in section 2.1.5.2 for all vehicle configurations running at 120km/h on the DCL route (number

1). According to Figure 2-9 route 1 has the closed quality distribution to the average of all tracks.

2.1.5.2 Vehicle dynamic response to track irregularities

The vertical force response for the three freight vehicles simulated on UK DCL route 1 is analysed. Figure 2-9 shows route 1 to have the closed quality distribution to the average of all routes. The vertical response is quantified in terms of the standard variation (SD) of the dynamic load (variation around nominal) at the wheels of the leading bogie. The maximum value is taken out from of all four wheels' response.

In order to obtain an idea of the distribution of this data, histogram plots are generated in Figure 2-10. These show the mean value of the dynamic wheel load SD as well as its variation for the route. As expected the mean dynamic loads for the tare vehicles are low (between 3.5 and 4.7kN) and their variation too (typical mean+3σ varies between 5.26kN and 7.18kN)[2]. On the other hand the laden vehicles have high dynamic contribution (between 9.7kN and 13.6kN) with high variation (typical mean+3σ varies between 14.7kN and 26.7kN). Furthermore, each vehicle also shows large differences, V1 clearly is badly responding to the track input while heavily loaded. In its part laden configuration is it is also responding with a mean value of 8kN and a mean+3σ of 16.35kN. This illustrates the importance of the details of the vehicle type and of the modelling assumptions made, as well as the importance of the vehicle loading conditions.

In order to be able to estimate the dynamic forces as a function of the track quality, the same data is plotted against the track horizontal level (SD value) in Figure 2-11 below. For all data a reasonable fit is achieved which depends principally on the vehicle type: r^2 = 0.81-0.86 for v3, r^2 = 0.70-0.71 for v2 and r^2 = 0.84-0.91 for v1. This is using a 1st order linear regression (least square method). It is also clear that the tare vehicles show little dispersion in the data and only a small increase with track SD (slope between 0.63 and 1.51kN/mm). On the other hand for the laden vehicles, both the scatter in data is more important (σ between 1.68kN and 4.36kN) and the slope is also much higher (between 2.23 and 6.58kN/mm). Vehicle V1 is also exhibiting an obviously poorer ride quality. The dashed line represents the best fit line + 3σ to represent an estimate of the expected maximum load limit. In all cases the data remains below this limit apart for one section for the laden vehicle v2 at around 2.6mm track SD.

Finally, in order to compare all vehicles together, the dynamics force SDs have been normalised with wheel load. This allows a like for like comparison of all vehicle types (v1, v2 and v3) irrespective of their actually loading. Figure 2-12 shows the same plot as Figure 2-11 but normalised. Here the increase can be quantified in percentage force per mm track SD. Values in Table 2.6 are thus obtained. Clearly the vehicle v1 shows a much larger force increase than the other two vehicles. The loading as a secondary influence with respect to vehicle type and in the case of v1, the part-laden vehicle actually sees the highest increase of all.

[2] To provide an estimate of the maximum likely encountered value, the mean added with 3 times the standard deviation of the population of the quantity of interest is quoted. This parameter, k=3, is used in EN14363 for the assessment of track loading and safety limits while carrying out vehicle testing or simulation of acceptance tests.

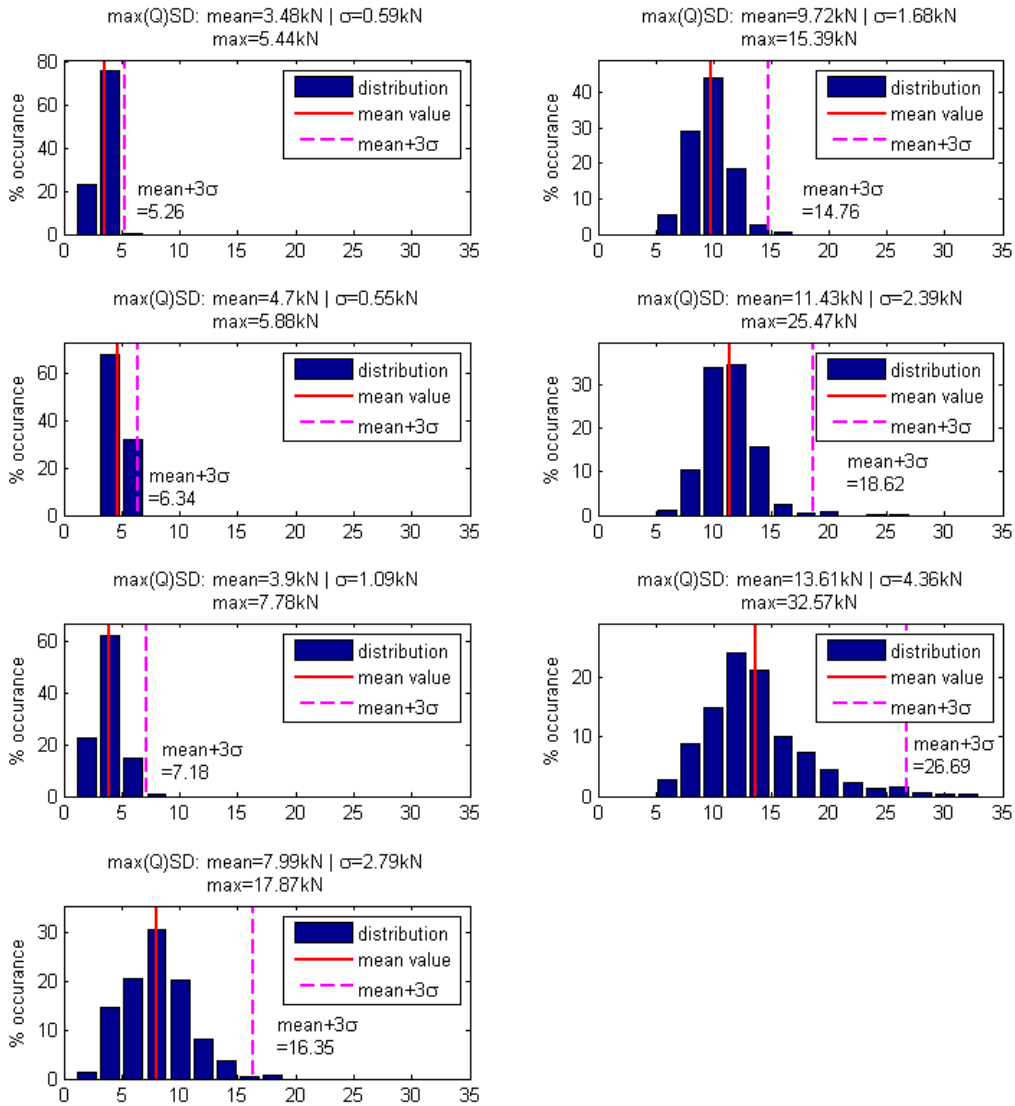

Figure 2-10: maximum wheel dynamic forces count: Tare (left hand column), Laden (right hand column), Part-laden (bottom left plot) for V3 (top row), V2 (middle row) and V1 (bottom two rows) vehicles.

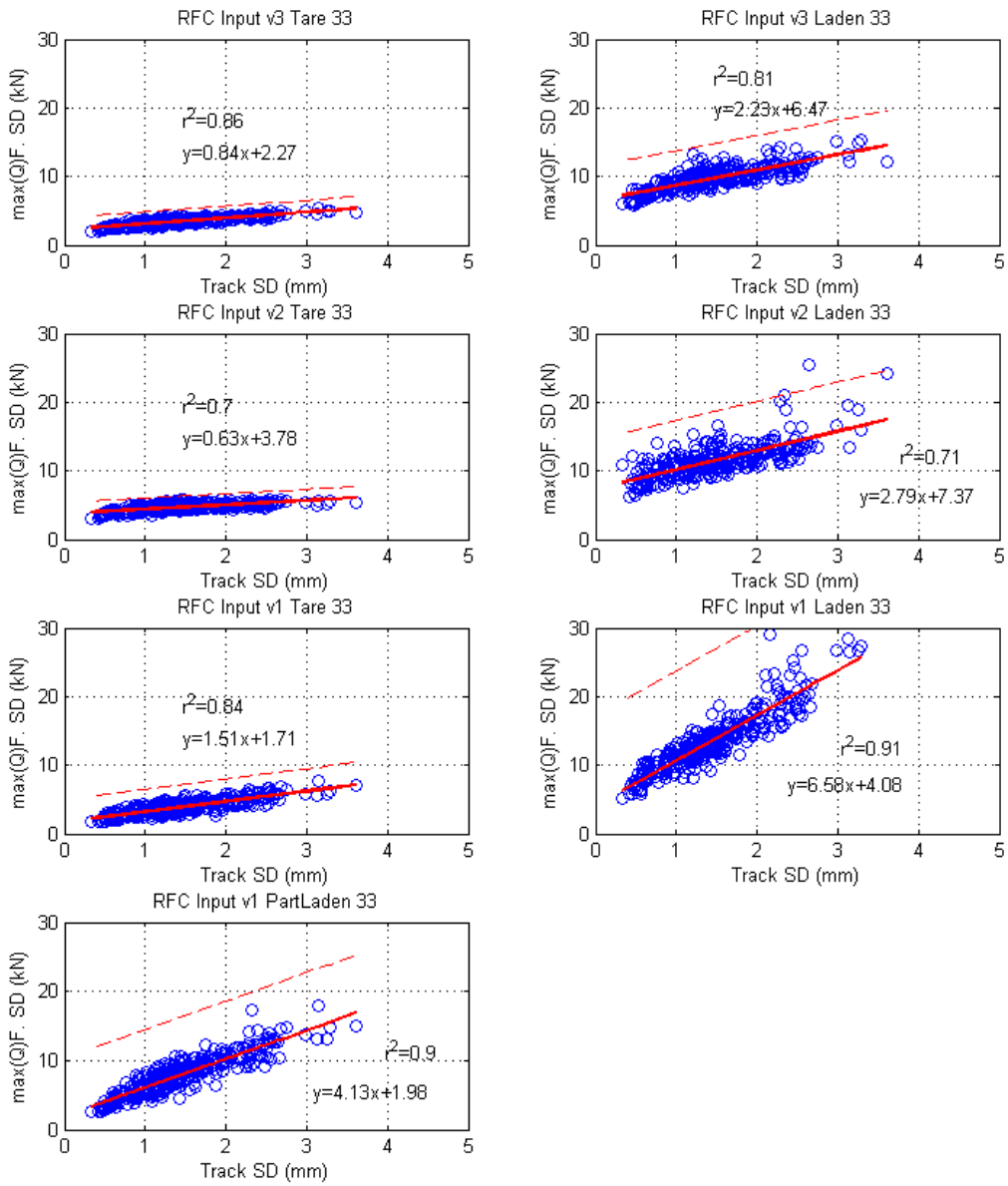

Figure 2-11: Maximum wheel dynamic force SD versus track quality SD: Tare (left hand column), Laden (right hand column), Part-laden (bottom left plot) for V3 (top row), V2 (middle row) and V1 (bottom two rows) vehicles.

Vehicle v3		Vehicle v2		Vehicle v1		
Tare	Laden	Tare	Laden	Tare	Part-laden	Laden
1.5%	1%	0.9%	1.1%	3%	3.8%	3.3%

Table 2.6: Pecentage of Force SD increase (wrt nominal) per unit track SD

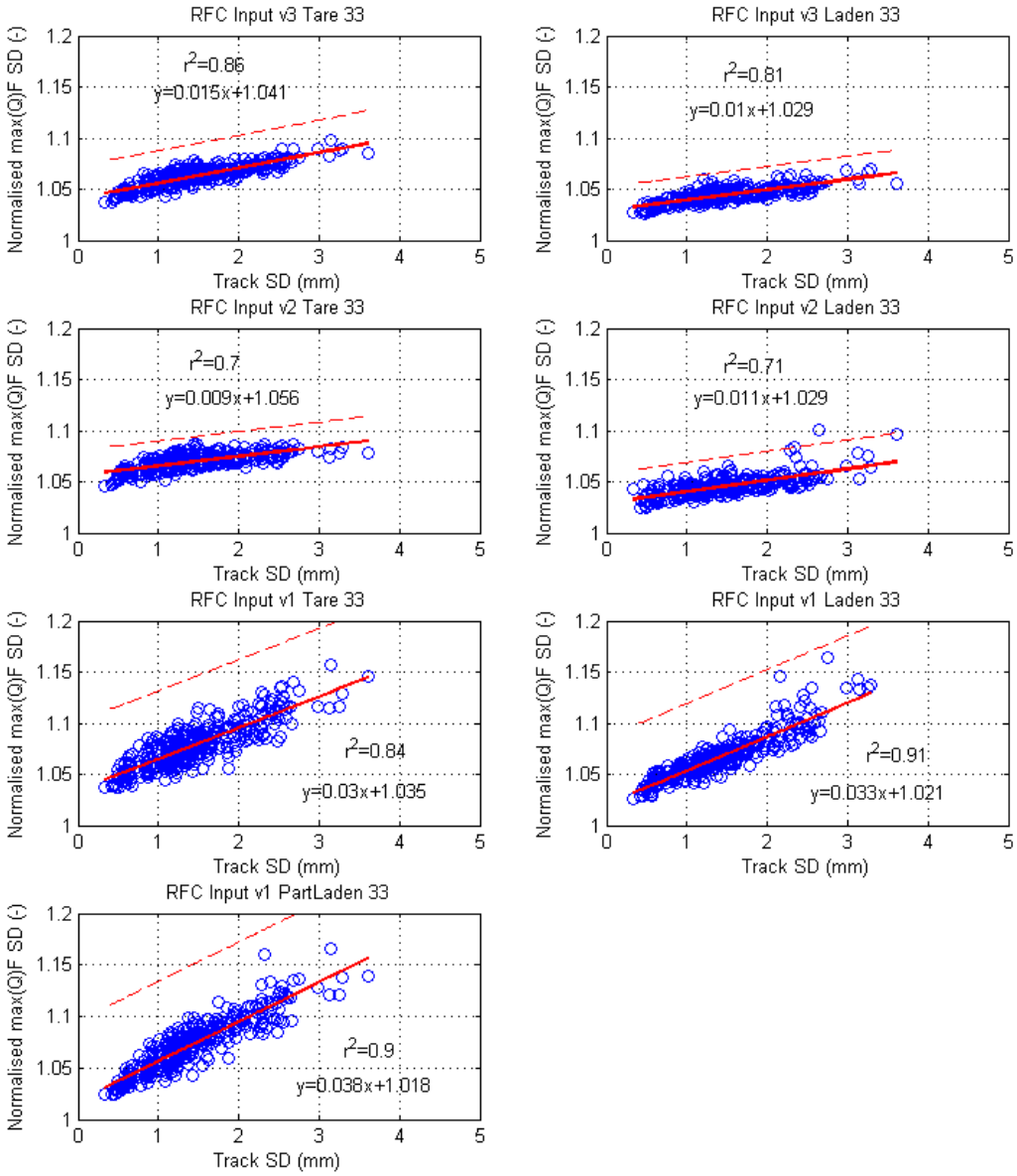

Figure 2-12: Maximum wheel dynamic force SD versus track quality SD – normalised with respect to wheel load: Tare (left hand column), Laden (right hand column), Part-laden (bottom left plot) for V3 (top row), V2 (middle row) and V1 (bottom two rows) vehicles.

2.1.6 Conclusion on section 2.1

The selected Sustrail UK routes have been analysed and compared to typical vehicle dynamic outputs in order to identify 'hotspot' corresponding to high loading forces on these tracks. These correspond to extreme cant deficiency and tight radius combinations of the route. The effect of three speeds have also been highlighted showing that increasing the freight vehicle to near linespeed or above will increase the propensity of cant deficiency running condition and therefore increase the loading forces on the high rail.

Additionally the effect of track quality on the vertical dynamic forces has been assessed. The following points are reported:

- The laden and part-laden vehicles show the highest variation in absolute dynamics loading.

- Different types of Y-series freight vehicle and their model specificities can lead to large differences in the predicted dynamics forces imposed onto the track. For the SUSTRAIL vehicle it was therefore verified that the simulation base case subsequently used by partners was matching with the v1 and v2 vehicles.
- Part-laden vehicle can show larger relative increase of dynamic forces with track SD than laden vehicle. It was therefore important to carry out further simulation based on a range of fully loaded and partly loaded conditions. Furthermore it was agreed that the tare condition is not as crucial from a track loading condition and track deterioration point of view.
- Increase in dynamic track forces variation as a function of the unit track quality was predicted between 1% of nominal per mm (v1 and v2) and 4% of nominal per mm (v3). It is later ensured that the SUSTRAIL vehicle improves on the performance of the v1 and v2 vehicle used here.

2.2 Simulation of freight vehicle track loading and the predicted effect of the SUSTRAIL vehicle

2.2.1 Characteristics of the virtual test track (VTT)

In order to extend the simulation set to a wider parameter range a series of virtual test track (VTT) has been designed using a tool developed by the University of Huddersfield. The virtual tracks are based on the UK routes irregularities, but concateneted into a virtual test environment that is compliant with EN14363 and includes the relevant testing characteristics in terms of layout and quality distribution. The summary of the test tracks are given in the Table 2.9 and show that it covers the extreme running conditions in terms of speed and cant deficiency as highlighted in the previous subsection. The level of vertical irregularities per each test sections are shown in Figure 2-13 and the overall distribution Figure 2-14. Note that for subsequent results presented the VTT are repeated with factorising the amplitude of the track irregularities around the nominal value (80%, 90%, 100%, 110% and 120%) in order to increase the statistical representation of vehicle response against track quality (e.g. Figure 2-15).

Track number	Track type	Curve radius [m]	Number of sections	total track length	reference speed and cant deficiency
1	Tangent track	infinite	20	2000m	V_{adm}+10km/h
2	Large radius curves	1000 – 1200	12	1000m	V_{adm},$cd_{adm[0.5,0.9,1.05]}$
3	Average radius curves	400 – 600	10	800m	$cd_{adm[0.8,1.05,1.15]}$
4	Sharp radius curves	250 – 400	10	500m	$cd_{adm[0.9,1.05,1.15]}$

Table 2-7: Main characteristics of the virtual test track (VTT), with V_{adm} and cd_{adm} the admissible vehicle speed and admissible cant deficiency respectively as per EN14363.

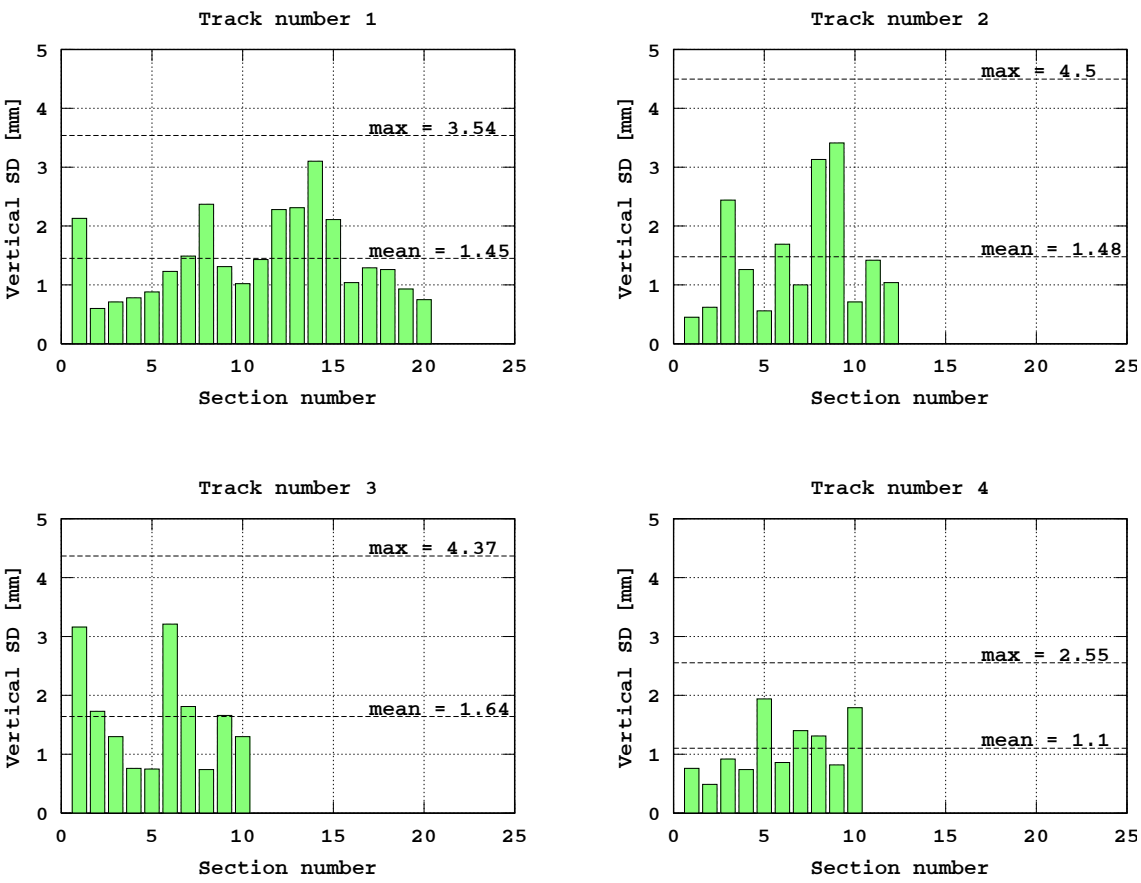

Figure 2-13: Vertical track irregularity, SD, for all sections of the four curve classes of the virtual test track (VTT)

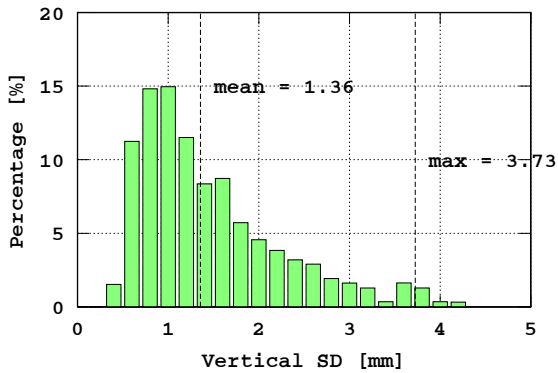

Figure 2-14: Vertical track quality distribution for entire virtual test track (VTT).

2.2.2 Vehicles and running conditions

Basis for the simulations is a validated existing model in GENSYS. This model is denoted "Reference Y25" in the following section. Two features, decisive for the track forces, that are suggested for the Sustrail bogie, double Lenoir links and enhanced primary damping, are modelled and the results from this model are denoted "Sustrail". S1002 wheel profiles are

used in combination with UIC60 rails at an inclination of 1 in 20. A value of 0.35 for the friction between wheel and rail is used for the simulations.

The vehicles are simulated at four different loading conditions, 4.7, 17, 22.5 and 25 tonnes axleload. For the tangent track section two speeds are used, 120 and 140 km/h.

2.2.3 Track quality effect on vertical dynamic forces

Standard deviation of the vertical track forces are plotted against the vertical track quality in Figure 2-15. The slope of the linear regression line is shown in Table 2-8 for all of the load cases. This shows that the dynamic performance of the vehicle at 120km/h and 140km/h are similar and there is not apparent deterioration of the ride quality at the higher speed. This also shows that the SUSTRAIL vehicle offers improved dynamic performance (and therefore reduced vertical forces) than the reference vehicle for all laden condition with the exception of the tare condition.

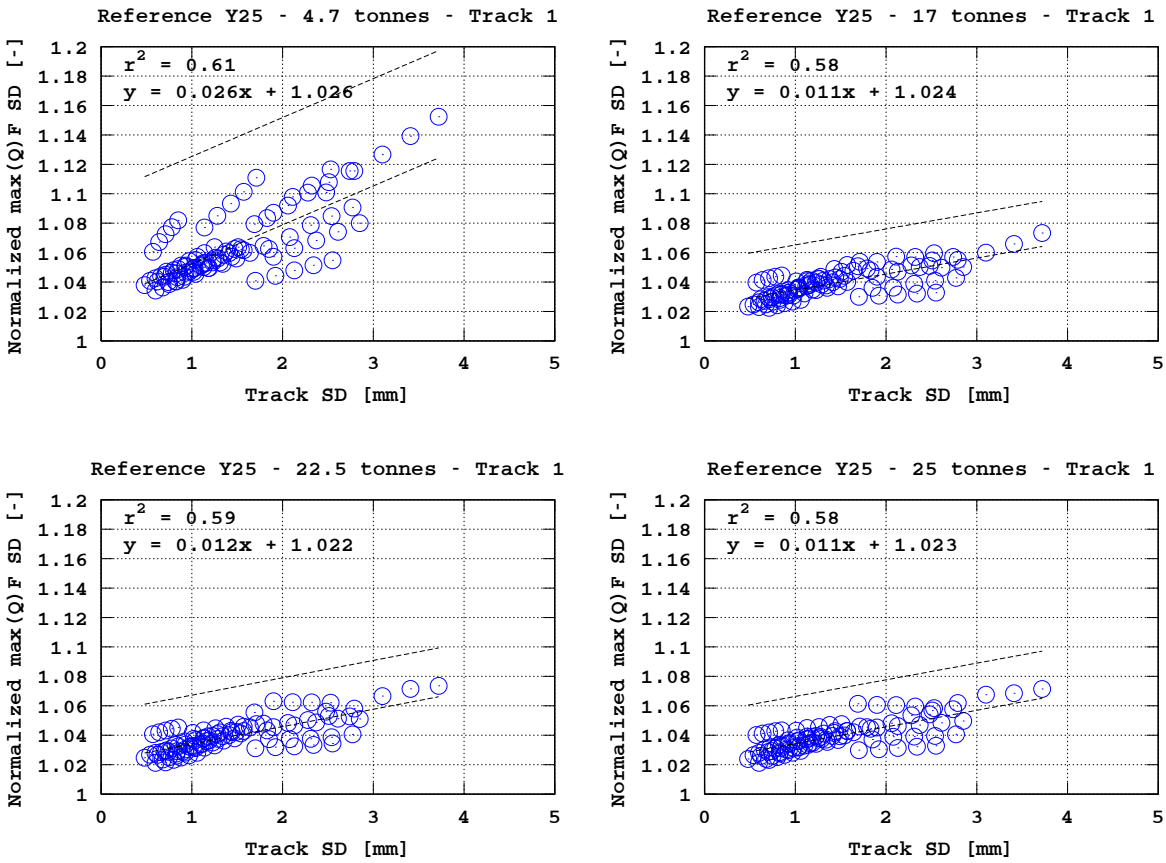

Figure 2-15: Maximum wheel dynamic force SD versus track quality SD – normalised with respect to wheel load: Reference vehicle at 4.7, 17, 22.5 and 25 tonnes axleload.

Vehicle	Axleload [tonnes]	ΔQ_{SD} 120 km/h	ΔQ_{SD} 140 km/h
Ref. Y25	4.7	2.4%	2.5%
Ref. Y25	17.0	1.1%	1.1%
Ref. Y25	22.5	1.2%	1.2%
Ref. Y25	25.0	1.2%	1.1%

Sustrail	4.7	2.6%	2.8%
Sustrail	17.0	0.8%	0.8%
Sustrail	22.5	0.8%	0.8%
Sustrail	25.0	0.9%	0.9%

Table 2-8: Pecentage of Force SD increase (wrt nominal) per unit track SD

2.2.4 Maximum and quasi-static track forces (Q_{dyn} and Y_{qst})

The track is divided in sections and the 99.85%-percentiles of the vertical track forces (Q) are calculated for each section. Maximum vertical force is calculated as the mean value plus 2.2 times the standard deviation.

$$Q_{\max} = Q_{mean} + 2.2 \cdot Q_{SD}$$

Examples of Q forces for the four different track classes in the VTT are shown in Figure 2-16.

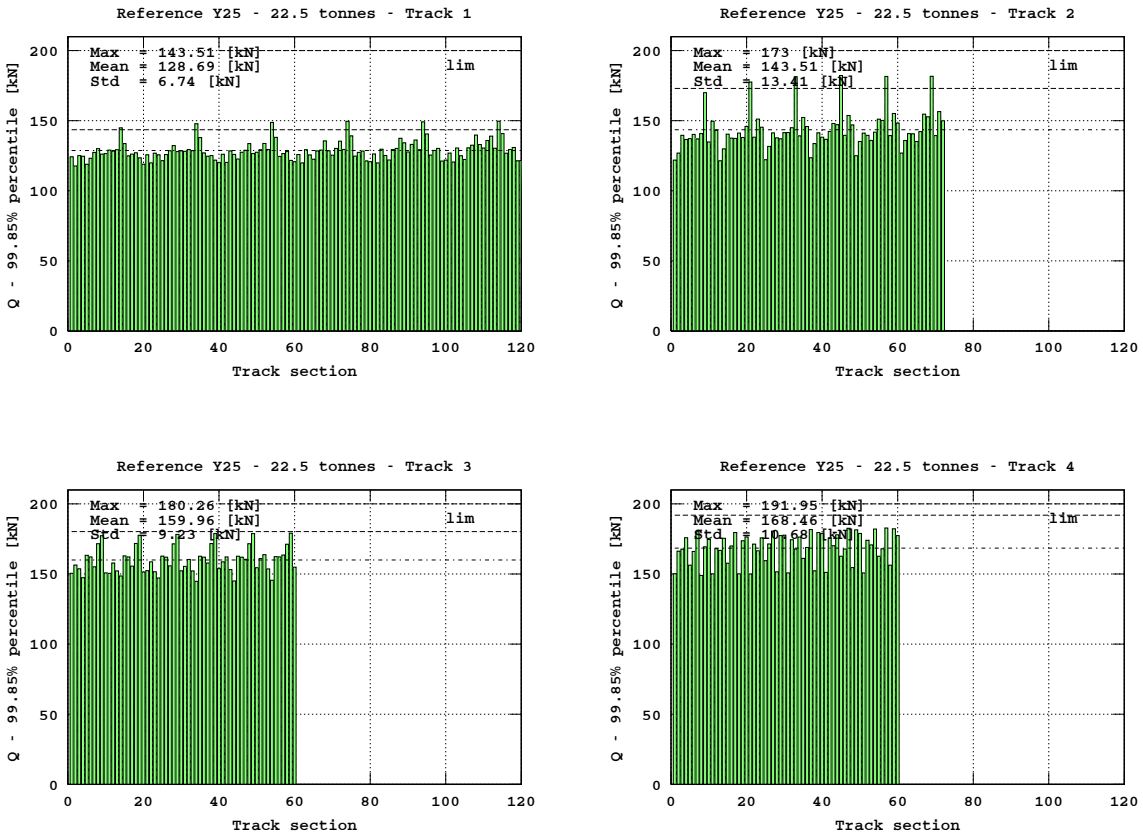

Figure 2-16: Vertical dynamic track forces, Q, for track classes 1-4. Reference vehicle at 22.5 tonnes axleload.

Quasistatic lateral force, Yqst, is shown in Figure 2-17. Comparison of the vertical and lateral forces for the Reference vehicle with respect to the Sustrail vehicle are shown in Figure 2-18 and the ratio between each vehicle in Figure 2-19.Values above 1 means that SUSTRAIL

vehicle performs better. The vertical dynamic forces are 2% lower for the Sustrail vehicle and the lateral forces are in average reduced by10-20 %.

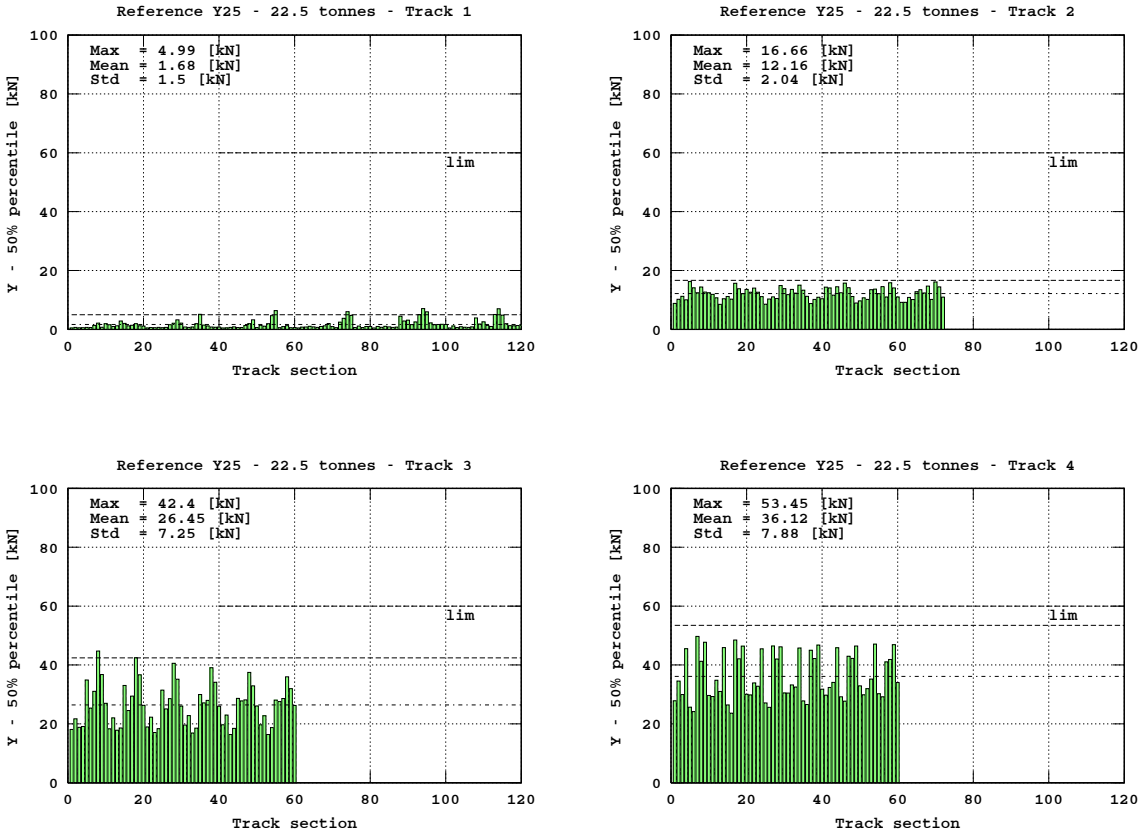

Figure 2-17: Lateral quasistatic track forces, Y_{qst}, for track classes 1-4. Reference vehicle at 22.5 tonnes axleload.

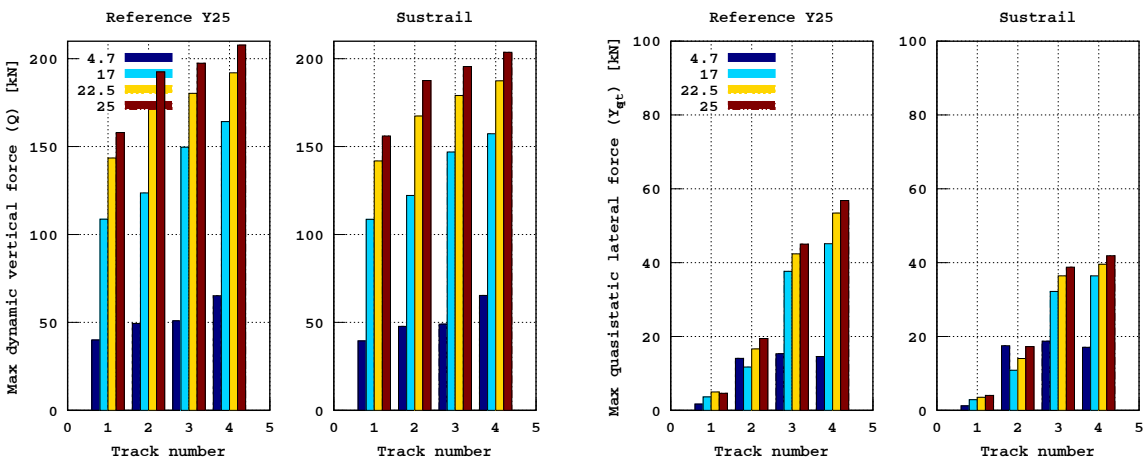

Figure 2-18: Comparison of vertical and lateral track forces between Reference and Sustrail vehicle.

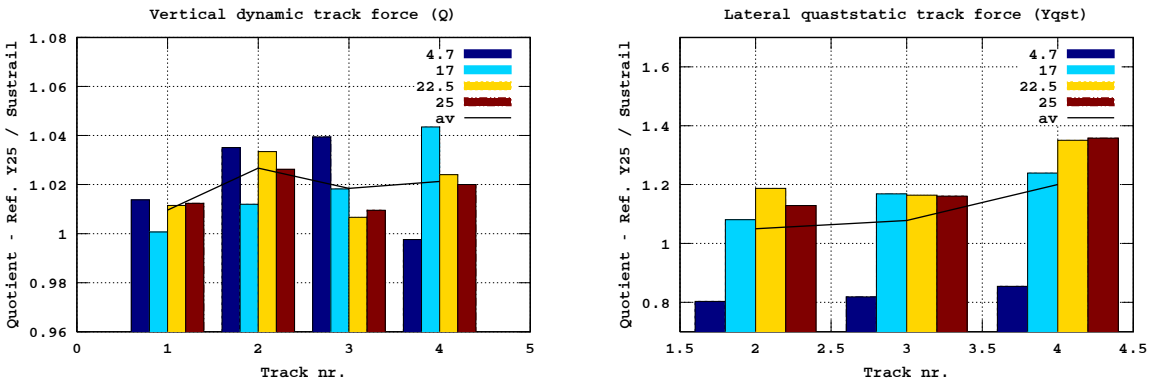

Figure 2-19: Comparison of vertical and lateral track forces between Reference and Sustrail vehicle.

2.3 Predicting the track loading and key components loading for the SUSTRAIL system limit conditions

The aim of this section is to derive an estimate of the loads generated in the main track elements: rails, fasteners, sleepers, based on the numerical simulation of train-track interaction considering a detailed Finite Element model of the track. This work was performed by POLIMI, using input from HUD and KTH regarding the loading cases to be considered.

A mathematical model of train-track interaction defined at POLIMI was used. The model is based on a Finite Element schematisation for the track and on multi-body models of the railway vehicles. A numerical procedure is defined in the time domain to simulate the dynamic interaction of the vibrating track with the passing train, considering wheel-rail contact forces and the excitation introduced by track irregularities. Tangent track running of the train and curve negotiation are both considered.

In this section, the track and vehicle models used to perform train-track interaction simulations are described and the results of the simulation cases run are presented.

2.3.1 Numerical method for the simulation of train-track interaction

Over several years, POLIMI has developed a numerical method for the simulation of train-track interaction using a finite element schematisation of the flexible track and a multi-body model of the vehicle. Below, a short description of the simulation method is provided[3].

The model is defined in the time domain to consider the non-linear effects related to wheel-rail contact and non-linear components in the vehicle suspensions. Two different sets of equations are written for the vehicle and for the track, coupled by the contact forces at wheel-rail interface, which are expressed as function of both vehicle and track coordinates. The two

[3] Diana G., Cheli F., Bruni S., and Collina A., Interaction between railroad superstructure and railway vehicles. Vehicle System Dynamics, 1993. 23 (Suppl.): p. 75-86.

Alfi S. and Bruni S., Mathematical Modelling of Train-Turnout Interaction. Vehicle System Dynamics, 2009. 47: p. 551-574.

sets of equations are solved simultaneously providing as output the motion of the vehicle, of the track, and the components of wheel-rail contact forces.

2.3.2 Multi-body model of the railway vehicles

The railway vehicles are modelled using the multi-body system formulation. The entire train set is subdivided into elementary units of the following types:

i. car body, modelled as a single rigid body;

ii. bogie assembly, modelled as a rigid bogie frame connected by primary suspensions to two (or eventually three) flexible wheelsets;

iii. other bodies attached either to a car body or to a bogie frame (e.g. motors, converters etc.), modelled as rigid.

the elementary units are connected each other by elastic and damping elements (linear and non-linear) reproducing the secondary suspensions and other elastic connections such as links between car bodies, elastic motor suspension etc. By combining the above listed elementary units, any specific train set architecture may be derived, like e.g. a composition of independent vehicles or articulated train sets.

The car bodies and standard bogies are modelled as rigid bodies, since their effect on wheel-rail contact forces is confined to the low frequency range, due to the effect of the primary and secondary suspensions. As far as wheelsets are concerned, two wheelset models with increasing complexity are defined: a first one considering the wheelsets as rigid bodies and a second one taking into account wheelset flexibility. In this study, a rigid model is used for the wheelsets.

Each rigid body in the model is assigned with 5 degrees of freedom (d.o.f.), corresponding to the vertical and lateral displacements of the centre of gravity and to yaw, pitch and roll rotations, whereas a constant speed V is prescribed for the forward motion of the centre of gravity.

The motion of each body is described with respect to a moving reference travelling with constant speed along the track centreline. The bodies are assumed to perform small displacements relative to the moving reference so that the equations of motion for the vehicle can be linearized with respect to kinematical non-linear effects only.

In this study the train is assumed to be represented by a sequence of 6 freight cars with Y25 bogies, the data used to define the model of the freight cars were taken from work done in SUSTRAIL WP3 and refer to the standard freight car model (not the one with improvements defined in WP3). No locomotive was considered, because of lack of data concerning this vehicle.

Three axle load values are considered: 17, 22.5 and 25 t/axle. These are obtained by adjusting the mass properties of the car-body, keeping unchanged the input data for the bogies and wheelsets.

2.3.3 The track model

The Finite element model of the track represents:

- the two rails as independent beams using Euler-Bernoulli beam elements;
- the sleepers as flexible bodies, also using Euler-Bernoulli beam elements;
- the rail fasteners as lumped visco-elastic elements connecting the rails and the sleepers;

- the ballast and embankment using a lumped mass placed under each sleeper and two distributed visco-elastic layers, one connecting the sleeper to the ballast mass and the other connecting the ballast mass to the fixed ground.

Track vibrations in both vertical and lateral directions are considered in the analysis.

A model of the track section is represented in Figure 2-20 below. The dots show the position of the nodes in each sleeper section; additional nodes are introduced in the two rails in between the sleeper, to have each rail divided into 4 beam elements per each sleeper bay. One lumped mass moving in vertical and lateral direction is introduced under each sleeper to represent the vibration of ballast. Ballast masses are not interconnected across neighbouring sleepers.

The complete finite element model of the track includes approximately 500 sleepers (each one modelled according to the scheme in Figure 2-20) and the beam elements representing the rails. The total number of nodes in the finite element model is approximately 7000, for a total number of degrees of freedom in the range of 40.000.

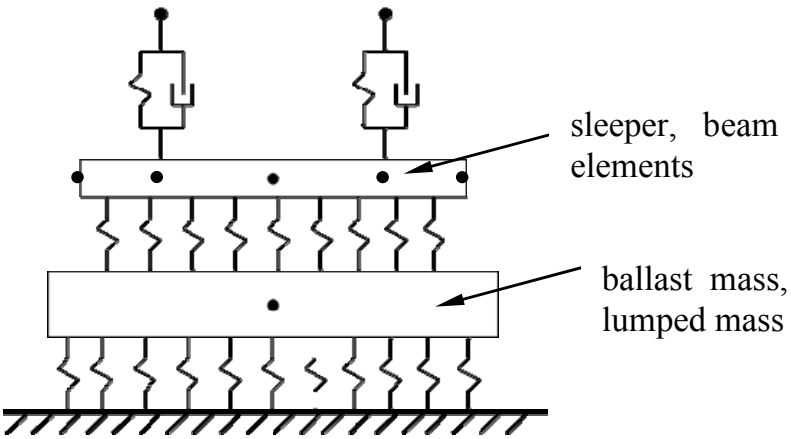

Figure 2-20: Sectional model of the track

The parameters of the track model are defined as follows.

Rail parameters: The UIC 60 section is assumed, material steel, Young modulus E=2.06 E11 N/m2, density ρ=7800 kg/m3.

Rail fasteners: stiffness and damping of the rail fasteners were defined based on values measured in the EUROBALT project, cf. Table 2.9, considering the "Typical" case.

Dynamic Values:	**Vertical Stiffness (kN/mm) per sleeper end**	**Vertical Damping (kNs/m) per sleeper end**
Soft track bed	20	50
Typical track bed	80	100
Stiff track bed	200	150
Soft rail pad	150	20
Typical rail pad	300	30
Stiff rail pad	1000	50

Table 2.9: Track stiffness and damping values from the EUROBALT project

Sleeper: The following dimensions are assumed for the sleeper:

- Length: 2.40 m
- Width: 0.300 m
- Mass: 300 kg

Ballast and embankment: The ballast and embankment model consists of:

- an upper visco-elastic layer (properties k_b, c_b) representing ballast stiffness;
- ballast inertia, partly attached on the sleepers and partly represented by a lumped mass below each sleeper;
- a lower visco-elastic layer (properties k_e, c_e) representing the stiffness of all embankment layers beneath ballast: sub-ballast, sub-grade, core embankment

The properties of these elements are chosen as follows.

Ballast stiffness: Assuming a ballast depth of 0.30 m below the sleeper and a Young modulus of 50 MPa for ballast, and furthermore assuming the stresses under the sleeper to be transferred into a portion of ballast contained in ±45 Deg from the sleeper (cf. Figure 2-21), the total ballast stiffness under one sleeper k_b is estimated to 270 kN/mm.

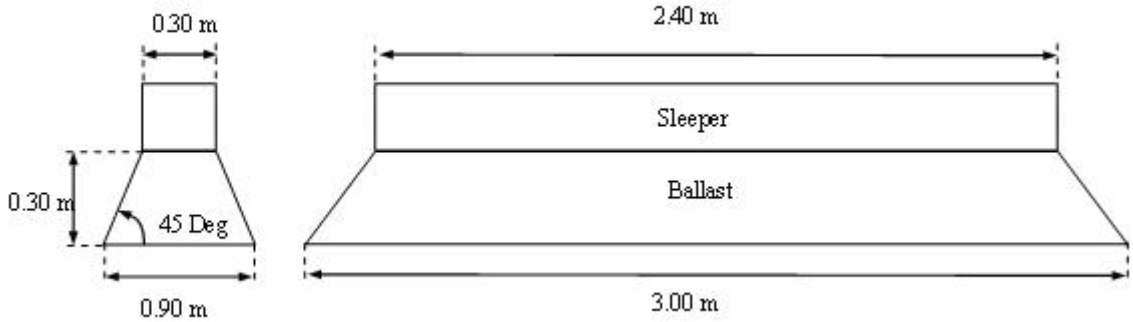

Figure 2-21: Ballast volume subject to stress transfer from the sleeper

Embankment stiffness: based on the estimated ballast stiffness obtained above, the embankment stiffness k_e is defined so that the series stiffness of k_b and k_e meets the overall track bed stiffness form the EUROBALT project, again considering the "Typical" and "Stiff" cases.

Ballast and embankment damping: these values are assumed to be proportional to the corresponding stiffness values according to a ratio:

$c_b / k_b = c_e / k_e = 1.25$

with stiffness values expressed in MN/m and damping values in kNs/m.

Ballast mass: It is assumed that the ballast volume participating in the vibration is the one shown in Figure 2-21. Assuming a ballast density of ρ_b = 2000 kg/m^3 a total ballast mass participating in vibration m_{bt} is obtained as:

m_{bt} = 2000 kg/m^3 x 1.62 m^2 x 0.3 m = 972 kg

However, the ballast mass will not be rigidly vibrating, but instead a linear gradient in the magnitude of ballast vibration amplitude with depth is expected. This leads to the assumption that the total ballast mass can be divided into three portions, as shown in Figure 2-22:

- ¼ of the total ballast mass is considered as rigidly vibrating with the sleeper, this mass (243 kg) is summed to the mass of the sleeper;
- ½ of the total ballast mass (486 kg) is assigned to the lumped mass below the sleeper, see Figure;
- the remaining ¼ of the total ballast mass is considered as attached to the fixed lower boundary shown in Figure 3.1 and hence is not considered in the model.

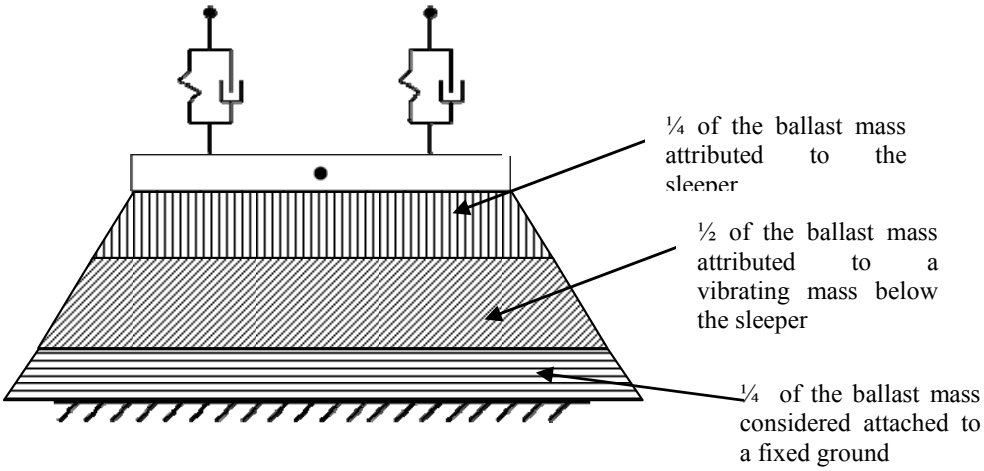

Figure 2-22: Repartition of the total ballast mass on the sleeper, lumped mass and fixed lower boundary

Track irregularity: is introduced in the simulations considering spatial realizations of the ERRI/ORE power spectral density curves[4], considering 'high level' irregularities. Additionally, irregularities provided by HUD and coming from the simulation scenarios used in SUSTRAIL WP3 were used as a term of comparison.

2.3.4 Simulation cases

The following simulation cases are considered in this study.

Nominal vehicle condition: first of all, the nominal vehicle condition is considered, for three axle load values: 17, 22.5 and 25 t/axle. For each axle load, three different vehicle speeds are considered. Here it is assumed that the maximum speed allowed for the vehicles with axle load 22.5 and 25 t/axle is 120 km/h, whereas for the vehicle with reduced axle load of 17 t/axle the maximum permitted speed is 140 km/h. The speed values considered for each axle load are detailed in Table 2.10.

These cases were run for track irregularities defined according to the ORE/ERRI "high level" spectra and for the "typical" properties of the rail pads and track bed. In Section 3 of this report the effect of changing from typical to stiff properties for the rail pads and for the track bed is studied.

	17 t/axle	**22.5 t/axle**	**25 t/axle**
Speed 1	100 km/h	80 km/h	80 km/h

[4] ORE B 176: Bogies with steered or steering wheelsets. Report No. 1: Specifications and preliminary studies, Vol. 2, Specification for a bogie with improved curving characteristics. ORE, Utrecht 1989

Speed 2	120 km/h	100 km/h	100 km/h
Speed 3	140 km/h	120 km/h	120 km/h

Table 2.10: Combinations of axle load and vehicle speed considered for the nominal vehicle condition

Effect of reduced un-sprung mass: the effect of improving vehicle design by reducing the mass of the wheelsets (i.e. the so-called un-sprung masses of the vehicle) was investigated by means of additional simulation cases in which a realistic reduction -10% of the un-sprung masses was introduced in the vehicle model. These cases were run for the same axle loads as for the nominal vehicle condition (17, 22.5 and 25 t/axle) but only for the maximum allowed speed of the vehicle, cf. last row in Table 2.10.

Effect of track irregularity: the effect of changing track irregularities from the spatial realisation of the ORE/ERRI "high level" spectra to measured track irregularities coming from SUSTRAIL WP3 was also investigated. This was done for the same three axle load values as previous analyses, limited to the maximum allowed speed of the vehicle, cf. last row in Table 2.10.

2.3.5 Simulation results: nominal vehicle condition

In this section, the results of numerical analyses performed for the vehicle in nominal condition and "typical" track stiffness values are reported, for all three considered axle load values. The results for the maximum allowed vehicle speed are first presented in full, then the effect of speed is analysed.

The analysis focussed on the following simulation outputs:

- Rail seat load, i.e. vertical force exchanged by the rails with the sleepers through the rail pads;
- sleeper-ballast contact pressure (i.e. vertical force applied by the sleepers to the ballast, divided by a nominal resisting area of ballast, cf. Figure 2-21);
- bending stress in the rails

Bending stresses in the rails are obtained as the superimposition of the stresses arising from rail bending in the vertical and horizontal plane. Stress time histories are computed in three points of the rail section, the two corners of the rail foot and the centre of the rail head, cf. Figure 2-23 and for the sake of conciseness only the maximum of these three values is considered in the analysis.

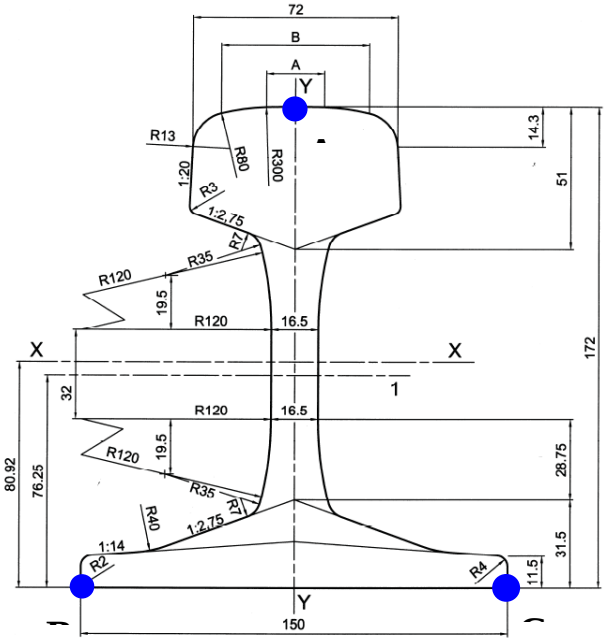

Figure 2-23: Points of the rail section at which stresses are evaluated

A preliminary analysis of results showed that the maximum loads evaluated in each sleeper bay were highly dependent upon the random distribution of track irregularity assumed in the simulation. Therefore, in order to obtain a statistically significant picture of track loading, the maximum loads were evaluated for 21 consecutive sleeper bays located in the centre of the track model.

2.3.5.1 Rail seat load

Figure 2-24 refers to the case of the vehicle in nominal condition, with 25 t/axle travelling at 120 km/h and shows the maximum rail seat force value obtained for each of the 21 consecutive sleepers analysed. These values range from 52.5 to 57 kN approximately, and should not represent a problem for the integrity of the rail fattener and of the sleeper.

Figure 2-25 shows the time history of the rail seat load for sleeper n.21, i.e. the one on which the maximum rail seat force value occurs. The rail seat forces on the left and right side of the sleeper are shown in blue and red colour respectively. A sequence of peaks is observed, corresponding to the passage of the 24 wheelsets in the composition of six freight cars considered in the analysis. The magnitude of the peak loads is comparable for all bogies/ wheelsets (as expected, given that six identical vehicles are considered here) and the differences are only to be ascribed to the effect of random track irregularities.

Figures from Figure 2-26 to Figure 2-29 show the distribution of the maximum rail seat loads obtained on the 21 examined sleepers and the time history of the rail seat load for the sleeper on which the maximum force occurs, for the axle loads of 22.5 and 17 t/axle and for the same speed of 120 km/h. As expected, the overall maximum of the rails seat force is increasing with the axle load, with a fairly linear trend. The waveform of the rail seat force time histories is not affected by the axle load, and basically consists of a sequence of peaks corresponding to the passage of the different bogies in the train composition.

Table 2.11 shows the overall maximum of the rail seat load for all speeds considered in the analysis. Vehicle speed appears not to have a major effect on rail seat forces and the small variation of this quantity observed with speed (in the range of 2-3%) is probably to be

ascribed to the random effect of irregularities, which would be a possible explanation of the fact that the trend with speed is not monotone.

	Axle load		
	17 t/axle	**22.5 t/axle**	**25 t/axle**
V=80 km/h	----	52.7 kN	56.7 kN
V=100 km/h	41.3 kN	50.6 kN	55.5 kN
V=120 km/h	39.8 kN	52.8 kN	56.9 kN
V=140 km/h	42.8 kN	----	---

Table 2.11: Overall maxima of the rail seat load forces for the nominal vehicle condition and for various speed and axle load values.

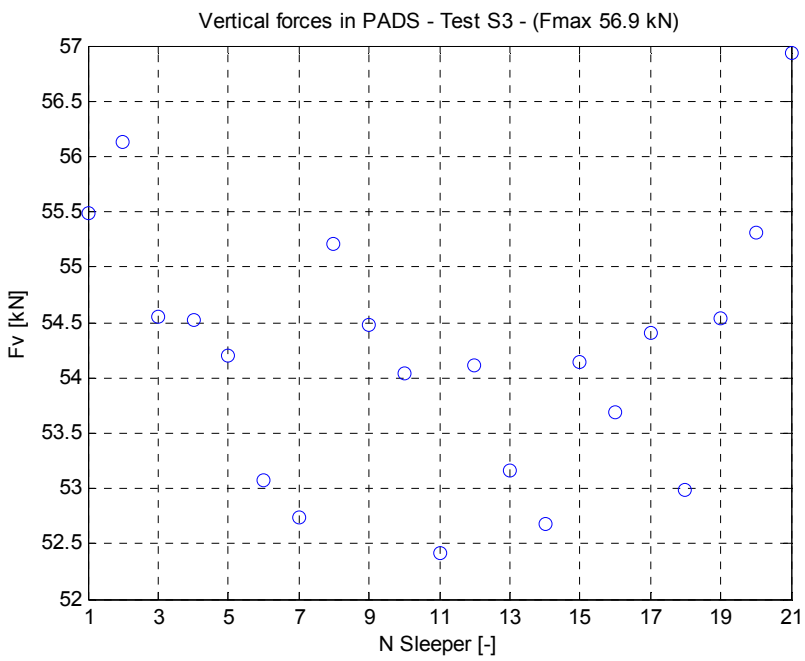

Figure 2-24: Maximum rail seat load on 21 consecutive sleepers. Nominal vehicle case, axle load 25 t/axle, speed 120 km/h.

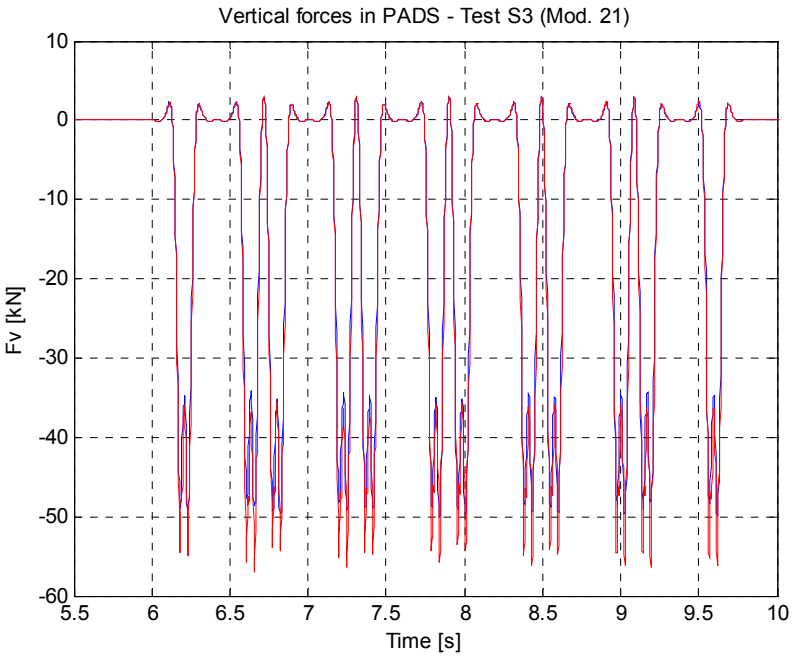

Figure 2-25: Time history of the rail seat load (left – blue, right – red) on sleeper n.21. Nominal vehicle case, axle load 25 t/axle, speed 120 km/h.

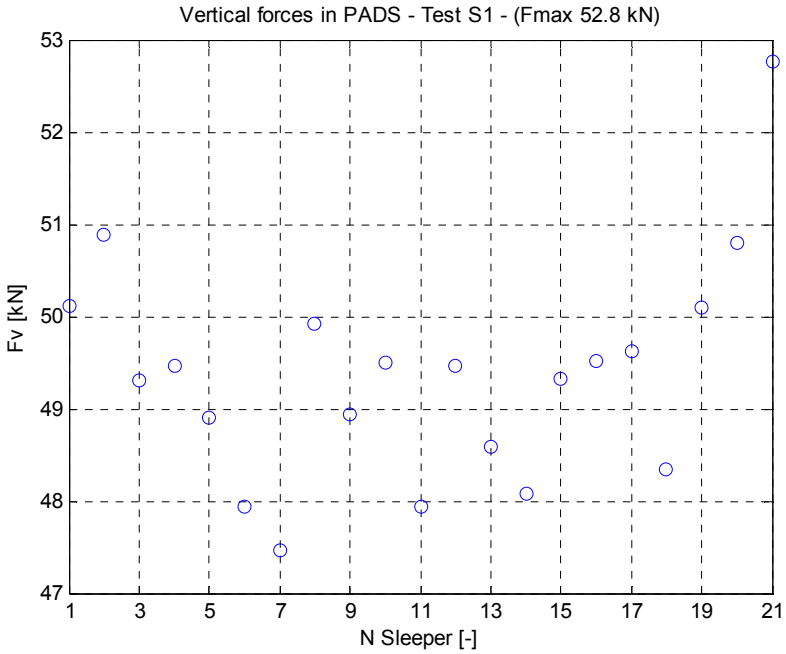

Figure 2-26: Maximum rail seat load on 21 consecutive sleepers. Nominal vehicle case, axle load 22.5 t/axle, speed 120 km/h.

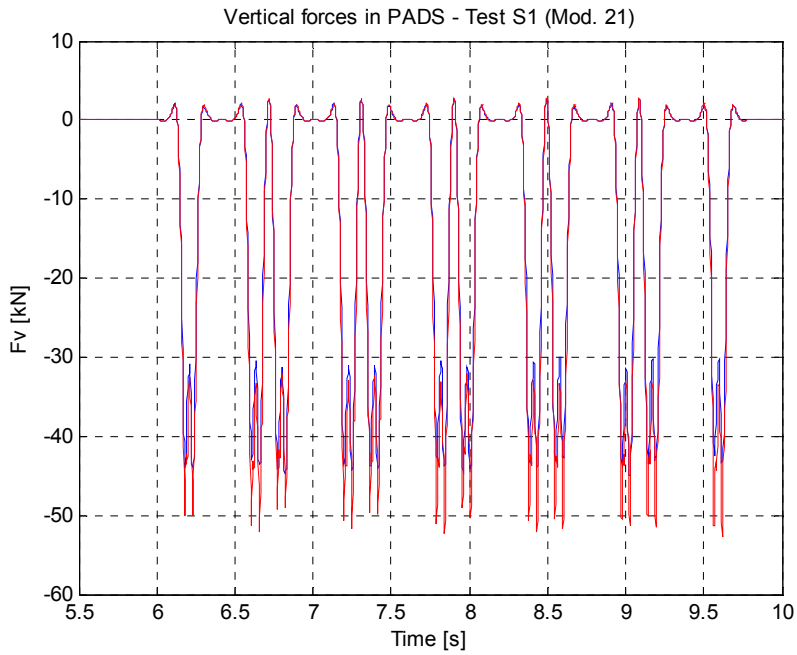

Figure 2-27: Time history of the rail seat load (left – blue, right – red) on sleeper n.21. Nominal vehicle case, axle load 22.5 t/axle, speed 120 km/h.

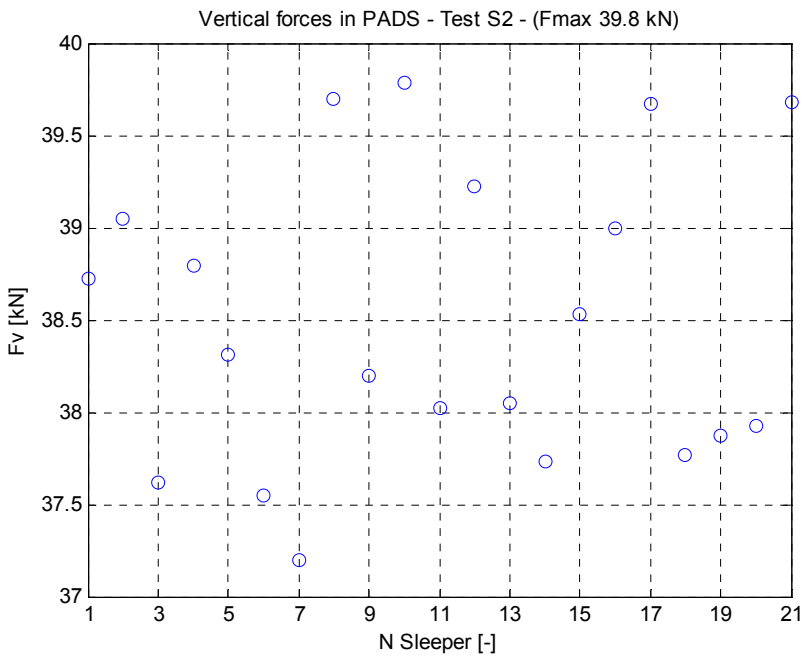

Figure 2-28: Maximum rail seat load on 21 consecutive sleepers. Nominal vehicle case, axle load 17 t/axle, speed 120 km/h.

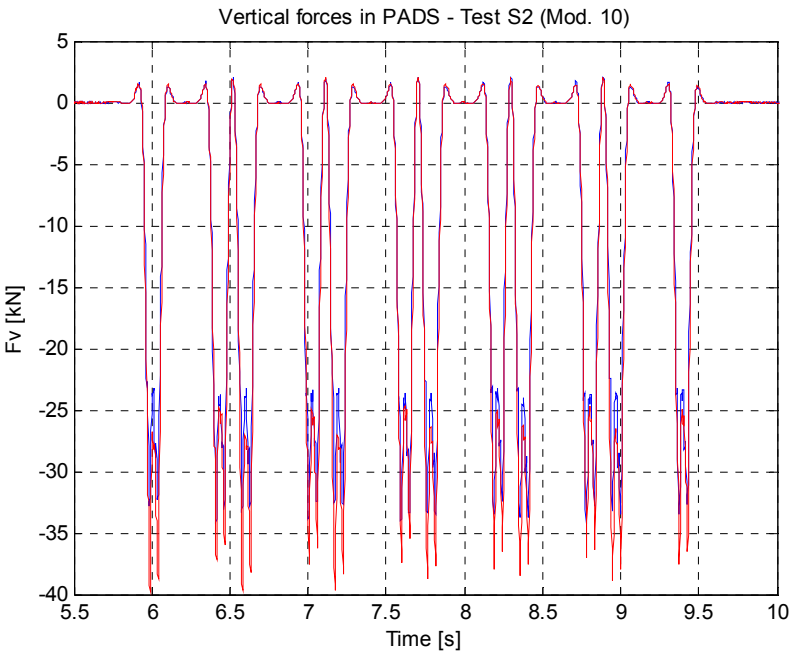

Figure 2-29: Time history of the rail seat load (left – blue, right – red) on sleeper n.10. Nominal vehicle case, axle load 17 t/axle, speed 120 km/h.

2.3.5.2 Sleeper-ballast contact pressure

The nominal sleeper-ballast contact pressure (SBCP) is computed as the ratio of the total vertical force applied by one sleeper to the ballast, divided by a nominal resisting area of ballast. This value can be used to evaluate the stresses induced in the ballast by train passage, and can be used to assess the capability of ballast to resist the loads without generating accelerated damage or settlement phenomena.

Figure 2-30 refers to the case of the vehicle in nominal condition, with 25 t/axle travelling at 120 km/h and shows the maximum SBCPs obtained for each of the 21 consecutive sleepers analysed. Like in the case of rail seat forces, significant fluctuations are observed from one sleeper to another, due to the random effect of track irregularities. The maximum value obtained is 153kPa, again on sleeper n. 21. As a term of comparison, for medium-good quality ballast, the maximum acceptable SBCP should be in the range of 250kPa.

Figure 2-31 shows the time history of the SBCP for the sleeper on which the maximum value occurs. Like in the case of rail seat forces, a sequence of peaks is observed corresponding to the passage of the 24 wheelsets considered in the simulation. The magnitude of the peak loads is comparable for all bogies/ wheelsets with slight differences caused by track irregularities.

For the other speeds and axle loads considered in the analysis, the time histories and dispersion across different sleepers of the SBCP are comparable to the case discussed above. Therefore, results are not show in detail, but the overall maxima are compared in Table 2.12. Similar considerations to those made for the rail seat forces apply: vehicle speed appears only has a minor effect on the results, whereas the SBCP values are increasing in a fairly linear trend with increasing axle load. Indeed, a high correlation is observed between the overall maxima of the rail seat force and the overall maxima of the SBCP. This is because inertial effects generated by the vibration of the sleeper are of relatively minor entity and hence most of the forces applied on the rail seats is transferred to the ballast below the sleeper, although with a re-distribution over a much larger area so that loads generated by train passage can be withstood.

	Axle load		
	17 t/axle	**22.5 t/axle**	**25 t/axle**
V=80 km/h	----	138.1 kPa	148.7 kPa
V=100 km/h	109.1 kPa	133.6 kPa	147.4 kPa
V=120 km/h	107.8 kPa	140.8 kPa	153.0 kPa
V=140 km/h	115.0 kPa	----	---

Table 2.12: Overall maxima of the sleeper-ballast contact pressure for the nominal vehicle condition and for various speed and axle load values.

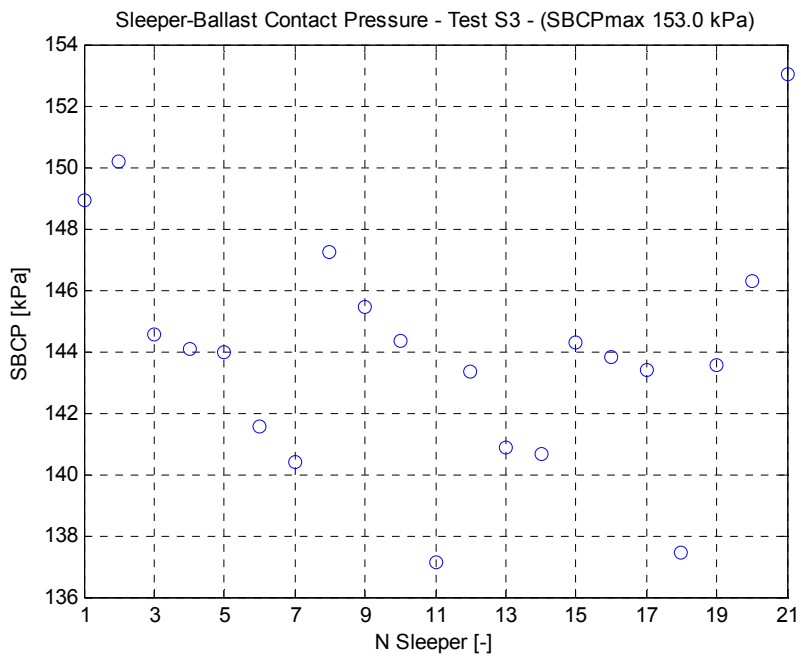

Figure 2-30: Maximum sleeper-ballast contact pressure on 21 consecutive sleepers. Nominal vehicle 7case, axle load 25 t/axle, speed 120 km/h.

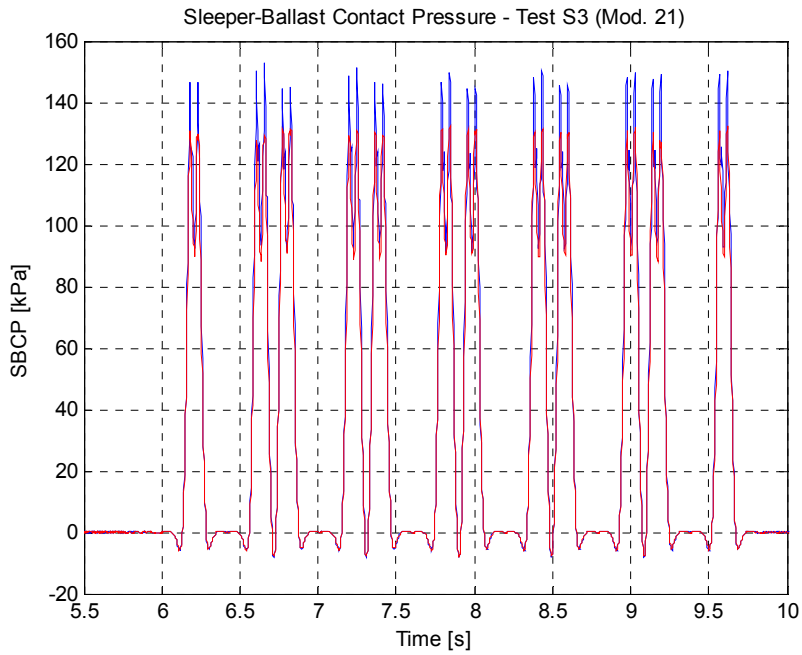

Figure 2-31: Time history of the sleeper-ballast contact pressure (left – blue, right – red) on sleeper n.21. Nominal vehicle case, axle load 25 t/axle, speed 120 km/h.

2.3.5.3 Bending stresses in the rails

Bending stresses in the rails are computed from the bending moments in the beam elements representing the rails in the Finite Element model of the track. The bending stresses presented in this section are obtained considering the effect of the two components of the bending moment, a prevailing one bending the rail in the vertical plane which is produced by the vertical component of wheel-rail contact forces, and a second one bending the rail in the horizontal plane which is mostly due to the lateral components of wheel-rail contact forces. Because of the much lower inertia of the rail section associated with rail bending in the horizontal plane compared to the inertia of the same section associated with bending in the vertical plane, the maximum stresses generated by the second component of the bending

moment are not negligible. Therefore, stresses are computed at three locations in the rail

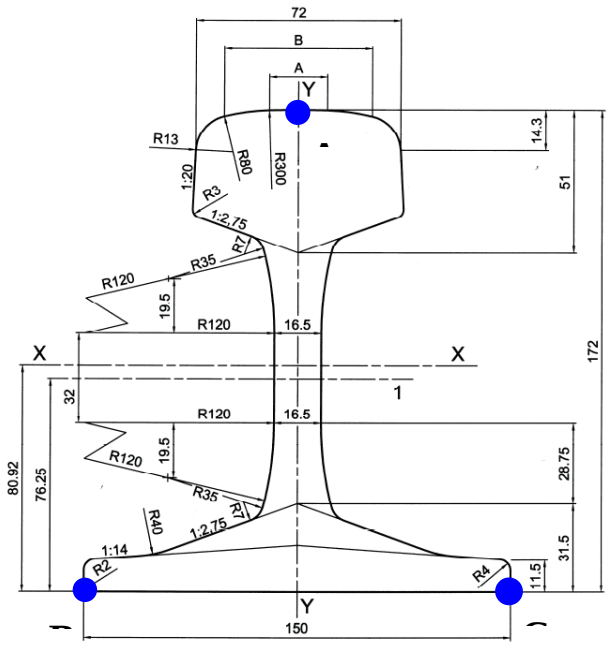

section, as shown in

Figure 2-23, but only the point giving rise to the maximum stress value is considered for subsequent analysis.

It should be noted that the rail stresses computed according to the procedure described above only consider the effect of train passage (including static and dynamic effects) but do not include other effects, e.g. those due to temperature variations in the long welded rail. Also it is worth recalling that all simulation cases presented here consider tangent track geometry, whereas additional bending stresses shall be expected in rails placed along a curve, due to the effect of load transfers caused by cant deficiency / excess and by track twist, and due to the additional lateral forces generated by centrifugal forces, creep forces, etc. Therefore, the analysis presented here is not meant to define the maximum rail stresses in absolute terms, but rather to compare different cases of vehicle speed and axle load in view of the mechanical resistance of rails.

Rail bending stresses are computed on 21 consecutive sleeper bays and, for each sleeper bay, stresses are computed in two locations: at the fastener and at mid sleeper bay. Because the stresses obtained at mid sleeper bay are significantly larger than those obtained at the fastener, the presentation of results here concentrates on the rail sections located at mid sleeper span.

Figure 2-32 shows the rail bending stresses obtained for each of the 21 consecutive sleepers analysed for the case of the vehicle in nominal condition, 25 t/axle, speed 120 km/h. For this quantity, a much larger dispersion of results is observed across the 21 sleeper bays considered. The reason for this is explained shortly below. The maximum value is obtained in sleeper bay n.3 and is 113.5 MPa. As a term of comparison the fatigue strength limits for rail steel are quantified as follows[5]:

- As-rolled rail: 300±20 MPa;
- Used rail: 220±20 MPa;
- Flash butt weld: 200±20 MPa;

[5] C. Esveld, Modern Railway Track – 2nd Edition, MRT-Productions, Zaltbommel, The Netherlands, 2001

- Thermit weld: 180±20 MPa.

Figure 2-33 shows the time history of the of the bending stress at the location where the maximum value occurs. Again, a sequence of positive peaks (traction) is observed corresponding to the passage of one wheelsets over the considered section of the rail. Each positive peak is preceded and followed by two negative peaks having minor amplitude, these are generated when a wheelset is located in one of the sleeper bays neighbouring the one considered. The dispersion of the positive peaks across the 24 wheelsets is quite large, despite the fact that the wheelsets and freight cars are identical in terms of their parameters. In particular, a high peak is observed during the passage of the first wheelset in the 6th and last freight car. This is due to a short duration flange contact occurring on this wheelset which produces a peak in the bending moment component related with lateral rail displacement.

Similar comments apply for the bending stresses obtained for other values of speed and axle load considered in the analysis. The overall maxima of the bending stresses for all simulation cases with the vehicle in nominal configuration are compared in Table 2.13. As could be expected, for the same vehicle speed the bending stresses are monotonically increasing with the axle load, but there is not a linear relationship between the two parameters, due to the unequal importance of dynamic effects in the different cases considered. Also, the dependence of results on vehicle speed for the same axle load is significant, with higher speed giving rise to a significant increase of the peak bending stress. This is clearly due to the increased importance of dynamic effects at higher speeds. It should be noticed that the maximum stress at 140 km/h for the vehicle with reduced axle load of 17 t/axle is significantly larger than the stress generated by the vehicle with standard axle load (22.5 t/axle) at 120 km/h. Also the maximum stress generated by the vehicle with increased axle load of 25 t/axle at 120 km/h is significantly higher than the stress generated by the vehicle with standard axle load at the same speed. These results indicate that both an increase of axle load and an increase of speed up to 140 km/h for a reduced axle load of 17 t/axle are likely to lead to increased stresses in the rails, and might require appropriate countermeasures, such as using steel grades with improved mechanical properties.

	Axle load		
	17 t/axle	**22.5 t/axle**	**25 t/axle**
V=80 km/h	----	87.1 MPa	93.7 MPa
V=100 km/h	84.9 MPa	86.8 MPa	94.2 MPa
V=120 km/h	73.0 MPa	90.5 MPa	113.5 MPa
V=140 km/h	98.8 MPa	----	---

Table 2.13: Overall maxima of the rail bending stresses at mid sleeper bay for the nominal vehicle condition and for various speed and axle load values.

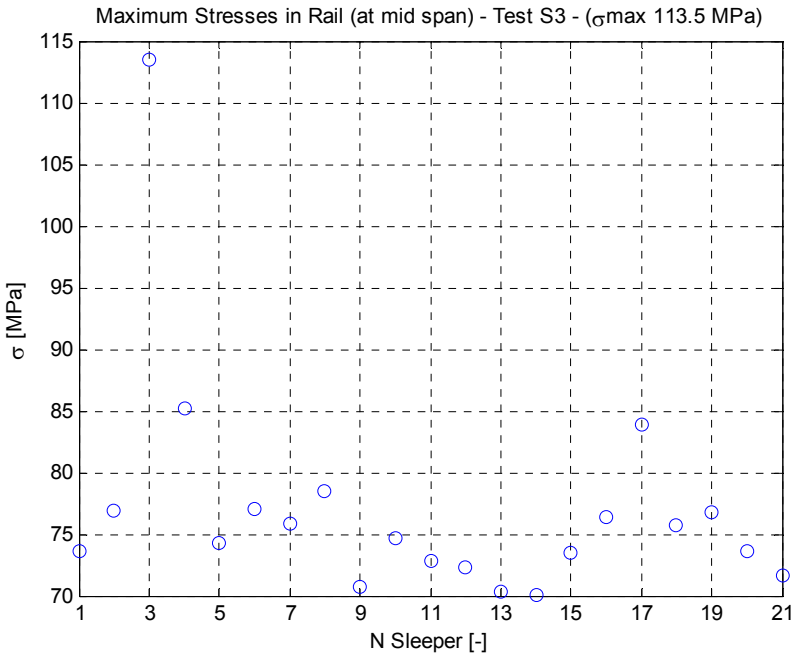

Figure 2-32: Maximum bending stresses at mid sleeper bay evaluated on 21 consecutive sleeper bays. Nominal vehicle case, axle load 25 t/axle, speed 120 km/h.

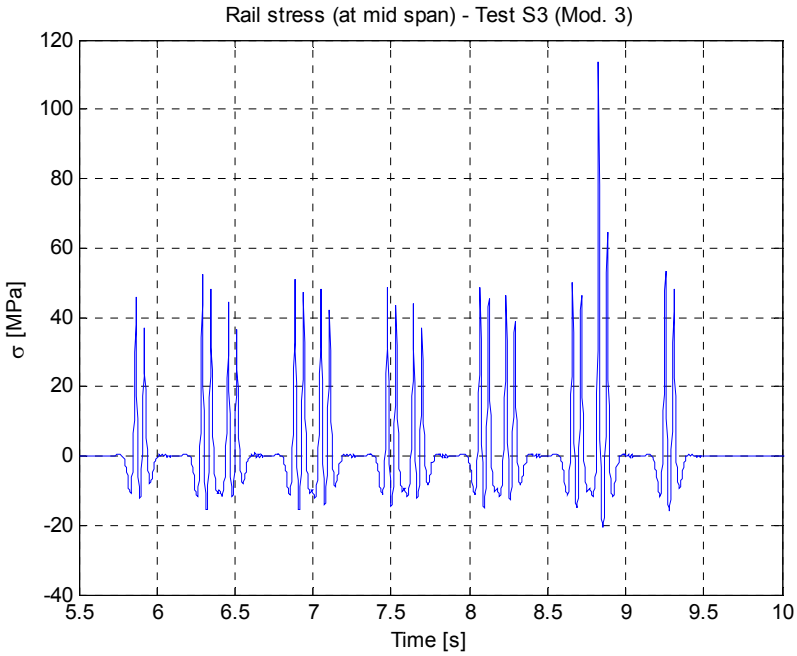

Figure 2-33: Time history of the bending stress at mid sleeper bay, sleeper bay n.3. Nominal vehicle case, axle load 25 t/axle, speed 120 km/h.

2.3.6 Simulation results: effect of reduced un-sprung mass

In this section, the effect of a reduction by 10% in the un-sprung masses of the freight car is evaluated. To this aim, the same cases presented in section 2.3.5 for the nominal vehicle condition were run also for a modified model of the vehicles, in which the mass of all wheelsets was reduced by -10%. Only the maximum vehicle speed was considered in this analysis, given that the reduction of the un-sprung masses is expected to affect mostly the

dynamic loading of the track, and hence the largest benefits are expected to occur at high speed.

Table 2.14 summarises the comparison of results for the nominal vehicles and the vehicles with reduced un-sprung mass, in terms of overall maxima of the quantities observed. It is observed that the reduction of the un-sprung mass affects only by a minor amount (1.5-3%) the rail seat forces, as these are mostly due to the static and quasi-static effect of axle loads moving along the track. Also the sleeper ballast contact pressure values are affected by the reduction of un-sprung masses by a similar percentage amount. On the other hand, the reduction of the rail bending stresses is much more noticeable, and is approximately -16% for the vehicle with 17 t/axle load travelling at 140 km/h, more than 9% for the vehicle with 22.5 t/axle load and more than 12% for the vehicle with 25 t/axle load. As could be expected, the reduction is even more noticeable for the vehicle running at higher speed.

As a consequence of the important beneficial effect of the reduction of un-sprung masses, the faster vehicle with reduced axle load generates a lower rail stress at 140 km/h than the nominal vehicle with axle load 22.5 t travelling at 120 km/h, whereas even with reduced un-sprung mass the vehicle with increased axle load of 25 t generates higher rail stresses than the nominal vehicle with 22.5 t axle, but with an important mitigation of stresses.

It is therefore confirmed that the reduction of the un-sprung mass plays a pivotal role in mitigating track loads for increased speed and axle load, even in case the reduction is relatively small e.g. 10% as considered here.

		17 t/axle V=140 km/h	**22.5 t/axle** V=120 km/h	**25 t/axle** V=120 km/h
Rail seat load	Nominal	42.8 kN	52.8 kN	56.9 kN
	90% unsprung mass	41.5 kN	51.7 kN	56.0 kN
SBCP	Nominal	115.0 kPa	140.8 kPa	153.0 kPa
	90% unsprung mass	112.5 kPa	138.3 kPa	150.5 kPa
Rail stress	Nominal	98.8 MPa	90.5 MPa	113.5 MPa
	90% unsprung mass	83.1 MPa	82.2 MPa	99.7 MPa

Table 2.14:Comparison of maximum rail seat loads, sleeper-ballast contact pressure (SBCP) and rail stresses for the nominal vehicle condition and for reduced (-10%) un-sprung mass.

2.3.7 Simulation results: effect of track irregularity

In this section, the effect of a different track irregularity profile on the results of the simulation is assessed. The same cases presented in section 2.3.5 for the nominal vehicle condition and limited to the highest speed were run again considering a measured irregularity profile provided by HUD and referring to a UK line, instead of the previously considered irregularity profile derived from the ORE/ERRI spectra “high level”.

Figure 2-34 compares the two irregularity profiles in terms of their PSD curves for vertical profile and lateral alignment. For the sake of comprehensiveness, the ORE/ERRI spectra are shown in the figure for both “low level” and “high level” irregularities. The PSD of the measured irregularity profile shows some dispersion but the trend and overall level is in first approximation comparable to the ORE/ERRI spectra.

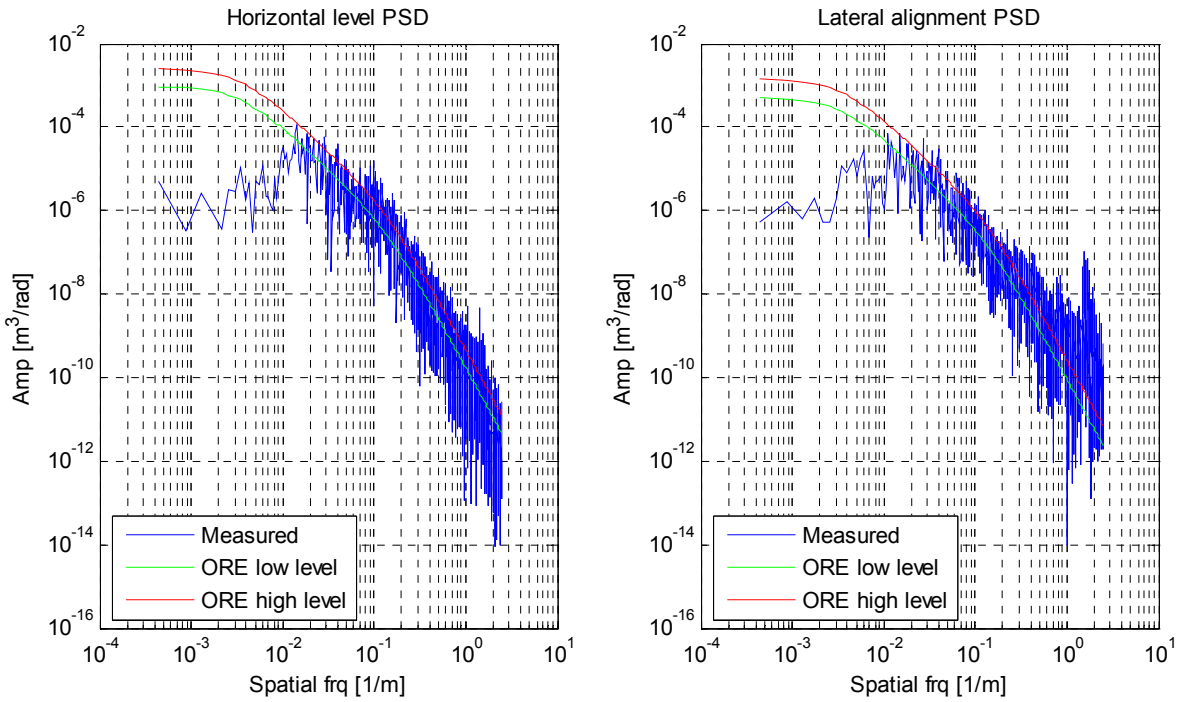

Figure 2-34: Comparison of measured irregularity PSD curve vs ORE/ERRI low and high level (left: vertical profile, right: lateral alignment).

Table 2.15 summarises the comparison of results for the two irregularity profiles, in terms of overall maxima of the quantities observed. The overall maxima of the rail seat load, SBCP and rail bending stress are all lower for the measured track irregularity, confirming that the use of ORE/ERRI high level irregularities in the analysis represents a conservative assumption.

		17 t/axle V=140 km/h	**22.5 t/axle** V=120 km/h	**25 t/axle** V=120 km/h
Rail seat load	ORE/ERRI	42.8 kN	52.8 kN	56.9 kN
	Measured	37.7 kN	47.7 kN	52.7 kN
SBCP	ORE/ERRI	115.0 kPa	140.8 kPa	153.0 kPa
	Measured	102.7 kPa	125.9 kPa	139.1 kPa
Rail stress	ORE/ERRI	98.8 MPa	90.5 MPa	113.5 MPa
	Measured	53.5 MPa	67.2 MPa	74.2 MPa

Table 2.15: Comparison of maximum rail seat loads, sleeper-ballast contact pressure (SBCP) and rail stresses for ORE/ERRI "high level" and measured track irregularities

3. TASK 4.1.2 - INFLUENCE OF TRACK STIFFNESS ON THE DYNAMIC LOADS CAUSED BY WAGONS ON TRACKS AND ON KEY COMPONENTS

3.1 Introduction on track stiffness

Track stiffness is an important parameter in railway track design and maintenance. However it remains an open point in the current technical specification for interoperability (TSI) relating to infrastructure[6]. It is well recognised that modern track construction especially for high speed require a good quality of sub-ground preparation in order to achieve a consistent and sufficiently rigid base for the track sub-ballast, ballast layers and superstructure (rails, pad/fastenings, sleepers) to be laid on. Good control of the global track stiffness allows keeping the forces distribution on the track elements (e.g. rail pads, sleeper-ballast interface) and the stresses in rails at a desireable level. Stiff tracks essentially allow keeping the rail stresses under control but they increase the load bearing on any of the dsicrete supports (rail pads and ballast layer), while low stiffness tracks allow a better distribution and therefore a reduced loads on every single bearing elements while increasing the bending stresses in rails. Understanding the balance between these two conflicting requirements is therefore paramount both in track design and maintenance.

Another important aspect of track stiffness is its the variation along the length of the track which can be significant on old and degradaded lines even from one sleeper to the next. This variation leads to increased dynamic interaction between vehicle and track and the resulting variation in vertical forces leads to differential settlement along the track.

The studies presented in this chapter are providing further insight into the effect of the stiffness variation based on numerical simulation of different vehicle and track configuration and based on measured stiffness variation at several sites.

3.2 The effect of track support stiffness on track behaviour based on UK measurement

The scope of this work is to analyse the influence of the variability of the support conditions on the vehicle track dynamic interaction. The approach taken is to use a vehicle-tack coupling model in which the sleeper ballast stiffness interface can be modified on every individual sleeper to reflect ballast stiffness values obtained from measurements.

The model used is a vertical vehicle-track coupling model, as shown in Figure 3-1.

[6] European Commission, *technical specification for interoperability relating to the 'infrastructure' sub-system of the trans-European high-speed rail system*, 2008/217/EC

European Commission, *technical specification for interoperability relating to the 'infrastructure' sub-system ofthe trans-European conventional rail system*, 2008/217/EC

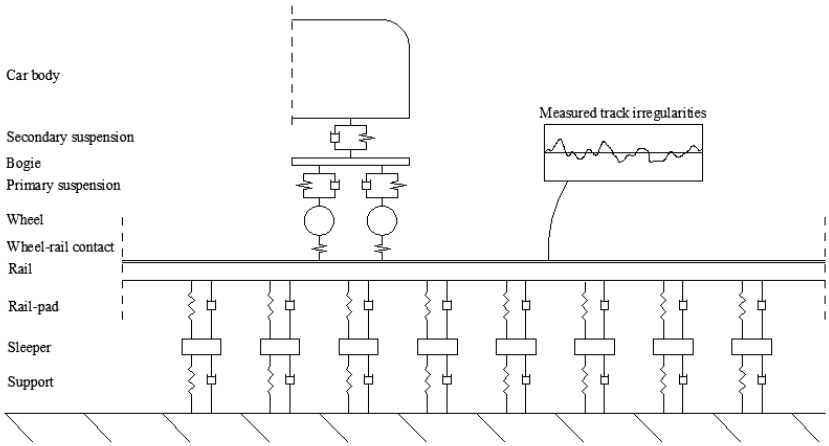

Figure 3-1: Vertical vehicle-track coupling model.

In particular, the track is modelled as a two-layer ballasted track, including the rail-pad layer, the sleeper mass and the support layer. The rail is represented as a Timoshenko beam to include the shear effects. Four beam elements are considered within each sleeper-spacing in order to achieve a good resolution of results in the frequency range of interest.

Fixed track parameters used fo the models are:

- 60E1 rails section and mass properties
- Rail pad dynamic stiffness is 270MN/m, representative of medium-hard rail pad.
- Sleeper mass is 308kg representative of a typical concrete sleeper
- Sleeper spacing is 0.65m

Note that the track includes no irregularities so as to isolate the effect of support stiffness from the permanent deformation of track on the vehicle-track dynamics.

3.2.1 Measurement data for the sleeper support stiffness

Four sets of measured sleeper support stiffness have been used, whose main characteristics are reported in Table 3.1. The data was measured using Falling Weight Deflectometer (FWD) equipment at four UK sites. Figure 3-2 shows the support stiffness values along the track for all four sites and the corresponding curve fitting distributions for each site are shown in Figure 3-3. The values reported in the EUROBALT project for 'soft', 'typical' and 'stiff' are also shown for comparison. This highlights the fact that the mean values for all site are representative of typical situation, i.e. situated around 80kN/mm. Some of the extreme low values are just above 'soft' while the extreme high values are approaching 160kN/mm. This data is therefore well representative of typical track but not of very stiff type of track. However it is mostly the degree of variability from one sleeper to the next at a same site which is of interest for this simulation task.

SITE	N. of sleepers	Support stiffness mean value [kN/mm/sleeper end]	Support stiffness SD [kN/mm/sleeper end]
1	155	84.6	14.4
2	70	68.0	18.1
3	80	110.4	16.2
4	81	71.0	8.6

Table 3.1: Main characteristics of the analysed sites

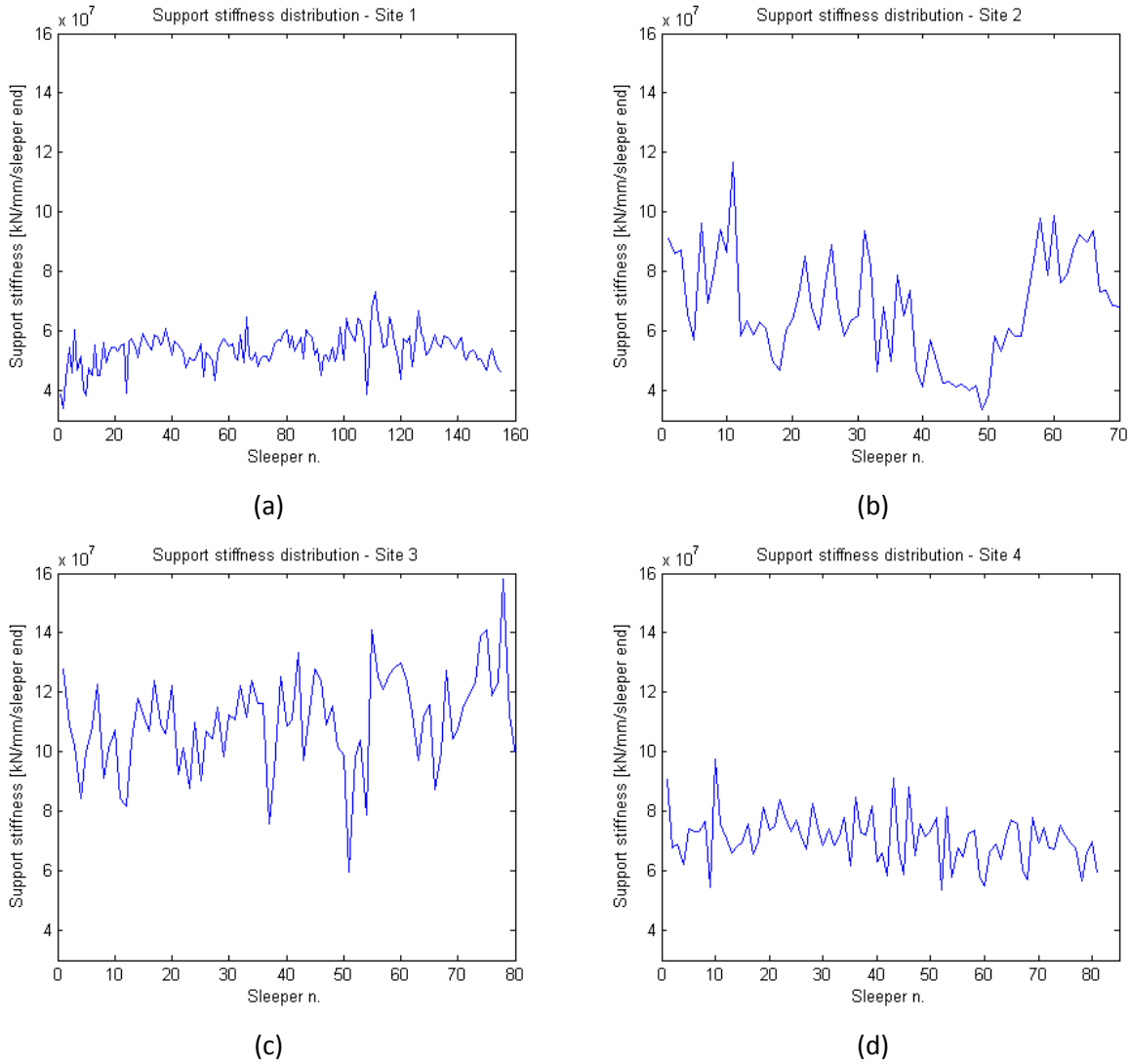

Figure 3-2: Support stiffness distribution in case of (a) site 1, (b) site 2, (c) site 3, (d) site 4.

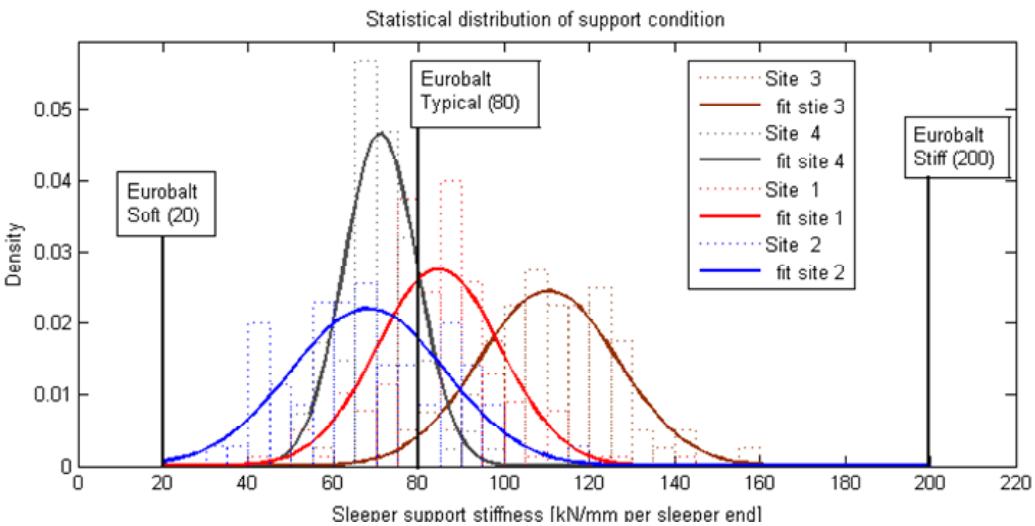

Figure 3-3: Curve fitting for the four sites considered

3.2.2 Vehicle and running conditions

The vehicle model is that of a quarter vehicle with assumed linearised suspension characteristics. The wheel load is 110kN (22.5t axle load) and the wheelset unspring mass is 700kg.

Three vehicle speeds are considered: 80, 120, and 140km/h.

3.2.3 Simulation results

3.2.3.1 Ballast force

The ballast forces quoted hereafter are for one rail as the model is that of a half track, assuming symmetrical vehicle-track configuration and loading. Figure 3-4(a) shows the distribution of the ballast force versus speed per each site and Figure 3-4(b) the percentage difference with respect to the mean value of all site at each speed (see Table 3.2 for the mean values). From both graphs in Figure 3-4 it can be observed that there is an increase in ballast force as speed increases at all sites. Force fluctuation between -5% and +8% of the average value are quoted with the higher values observed at site 3 (highest average support stiffness) and the lowest values observed at site 2 (lowest average support stiffness). Figure 3-5 confirms the force dependence on sleeper support stiffness with a very strong correlation coefficient between all the mean values.

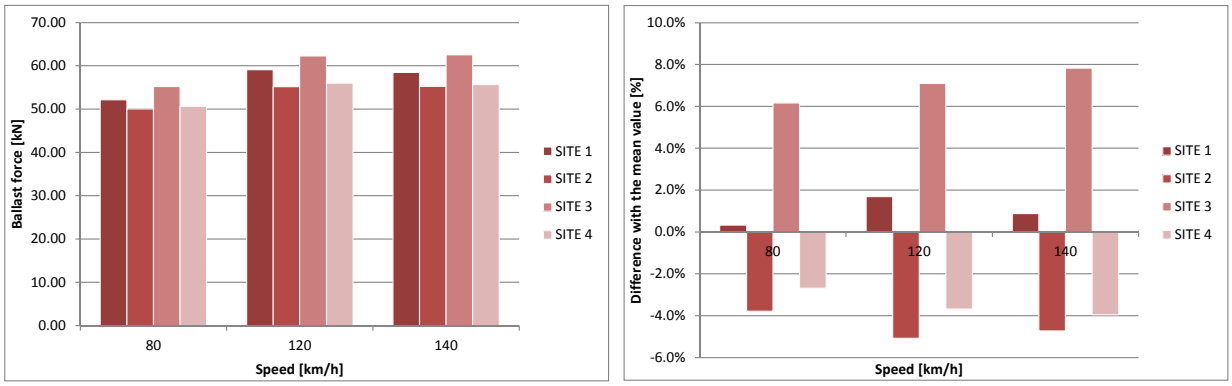

Figure 3-4: (a) Ballast forces versus speed varying the site; (b) Percentage difference of ballast force with the mean value versus speed varying the site.

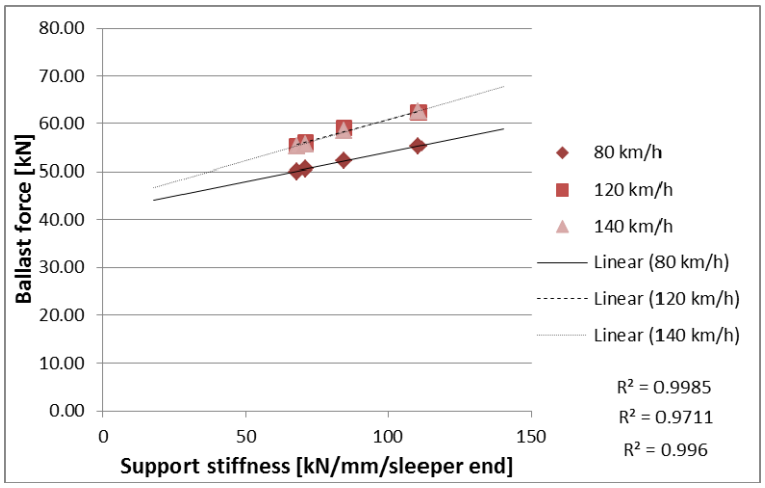

Figure 3-5: Mean ballast force response as a function of site mean support stiffness

Speed [km/h]	Ballast force mean value [kN]
80	52.00

120	58.12
140	57.96

Table 3.2: Mean values of ballast force as a function of speed

In Figure 3-6 an example of distribution of ballast force in the space domain is presented, showing the variation of forces along the track as a function of the sleeper support stiffness. It is visible that the higher speeds lead to the highest ballast forces.

A detailed analysis of this data allows verifying that the variation of ballast force attributed to support stiffness can lead to an increase of up to 30% (25% on average) with respect to the case where stiffness is considered homogeneous. At the same time certain sleepers can see a reduction of force by up to 26% (-23% on average). This result is important in showing that due to the large difference observed at different sites and more importantly at different sleepers on the same site, this will lead to differential settlement of the ballast layer.

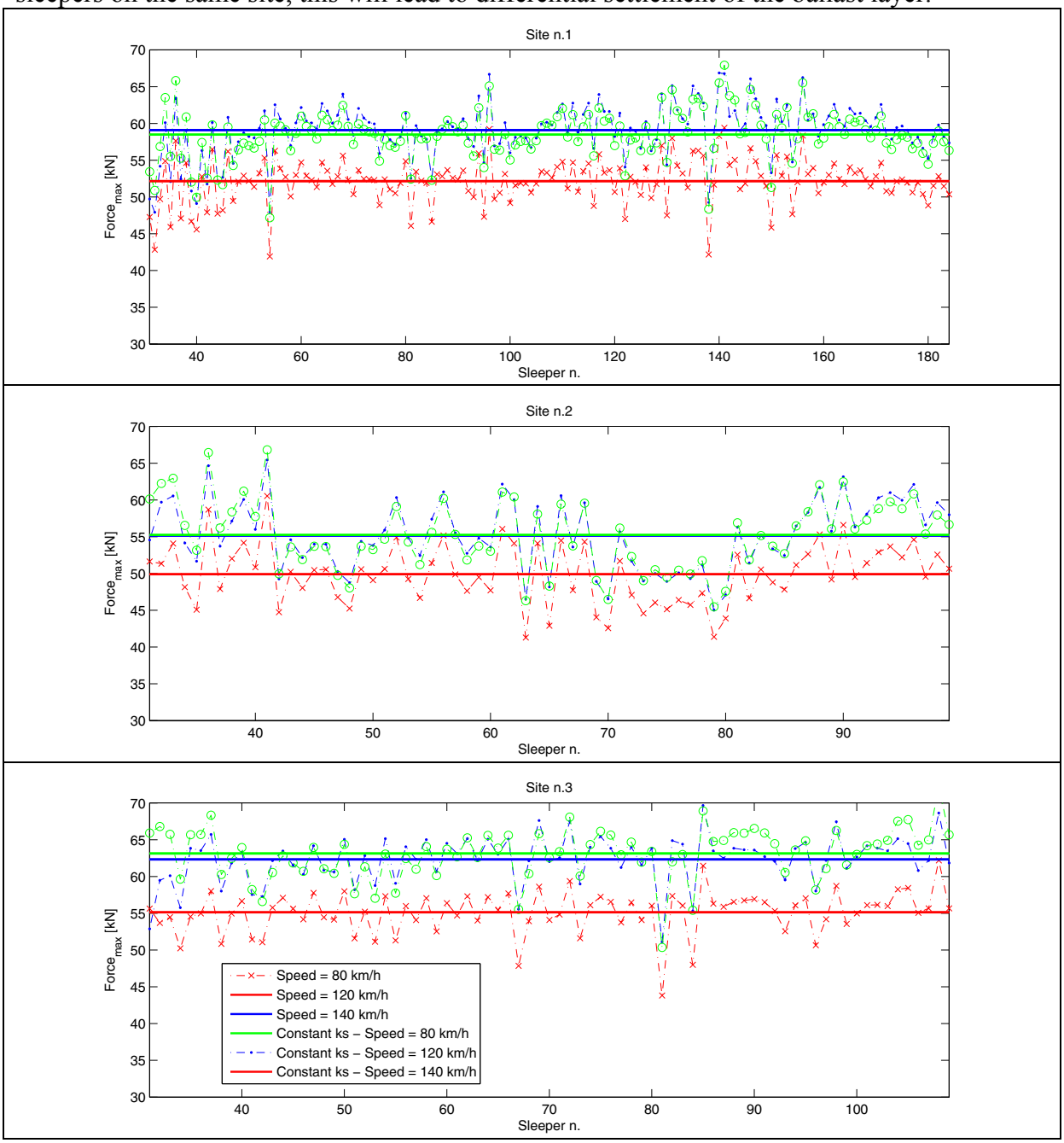

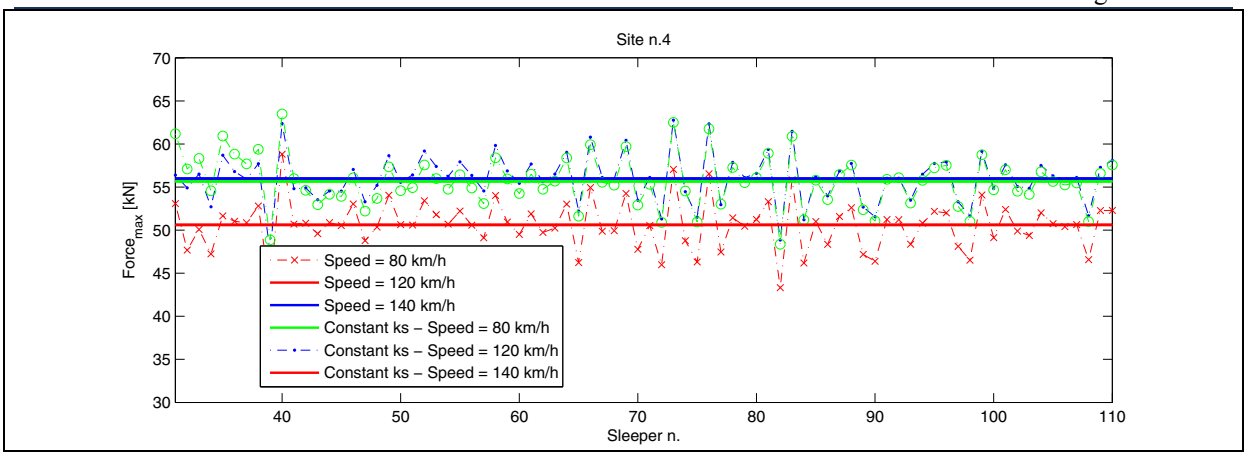

Figure 3-6: Selected distribution of the ballast force for site 1, 2, 3 and 4 (from top to bottom)

In Figure 3-7 the ballast forces versus support stiffness varying the site and the speed value are shown. On the side / bottom of each plot, there is the statistical distribution of the ballast force / support stiffness as well as the correlation between those two quantities and the correlation coefficient between the two sets of data is also given on each plots.

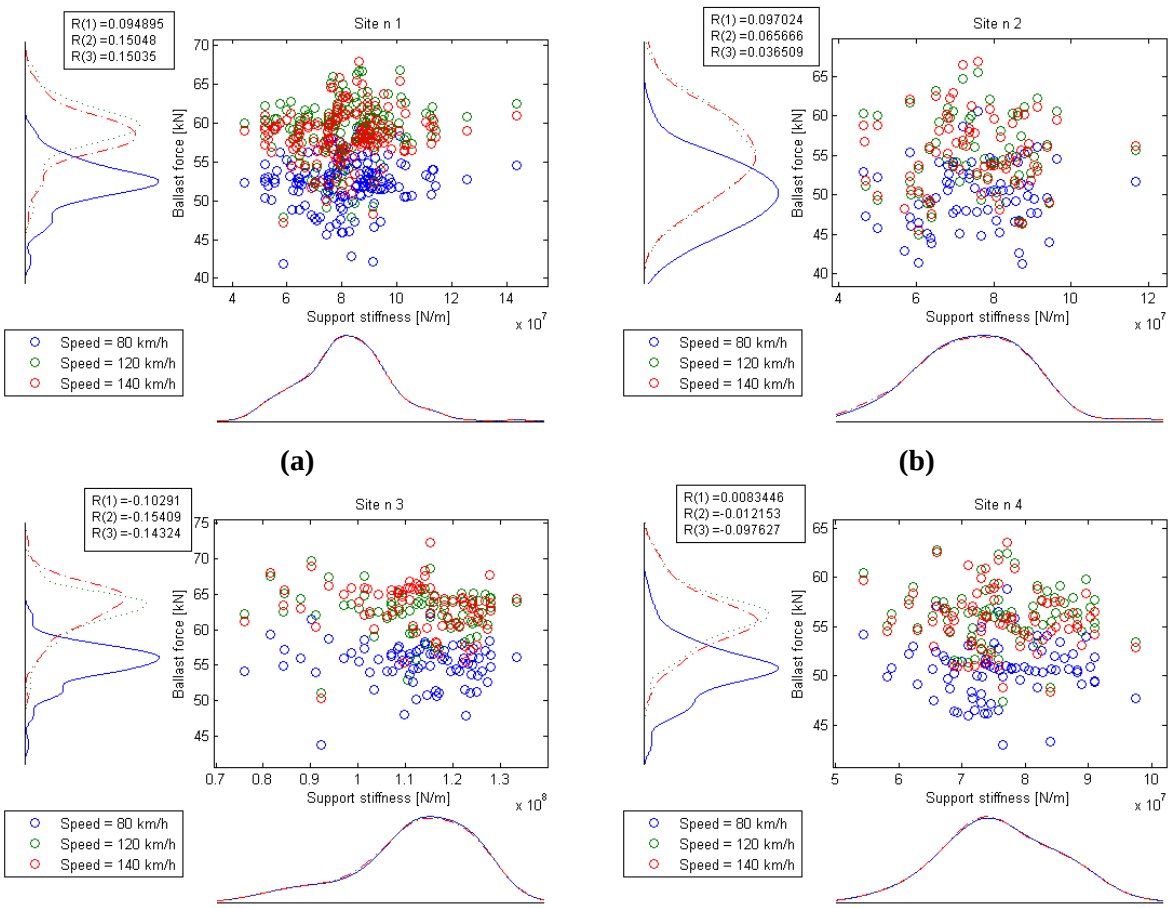

Figure 3-7: Distribution of the ballast force versus distribution of stiffness support ((a) site 1; (b) site 2; (c) site 3; (d) site 4).

Figure 3-7 is used to try and identify a correlation between the sleeper support stiffness and the ballast force response. The expectation would be that as the support stiffness increases the ballast force would also increase, however based on these results the correlation between the

two sets of data is fairly low (r^2 up to 10-15% only) and the correlation is not as evident. Some of the high response forces are often found for average sleeper stiffness because statistically these are the dominant population.

3.2.3.2 Sleeper displacement

Figure 3-8(a) shows the distribution of the sleeper displacement versus speed per each site considered and Figure 3-8(b) the percentage difference with the mean values, which are reported inTable 3.3.

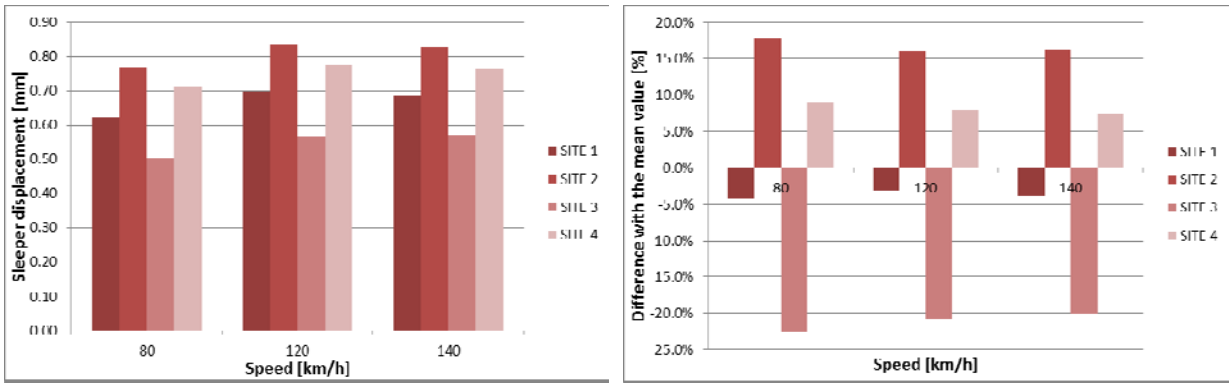

Figure 3-8: (a) Sleeper displacement versus speed varying the site; (b) – Percentage difference of sleeper displacement with the mean value versus speed varying the site.

Table 3.3: Mean values of sleeper displacement depending on the speed.

Speed [km/h]	Sleeper displacement mean value [mm]
80	0.65
120	0.72
140	0.71

Figure 3-8(a) shows an increase of sleeper displacement with increasing speed in all cases. As expected the site with the lower stiffness (site 2) shows the largest displacement while the site with the highest stiffness (site 3) shows the lowest displacement on average.

In Figure 3-9 a sequence of distribution of sleeper displacement in the space domain is presented, highlighting the large variation in vertical displacement along the track.

A more detailed analysis of the full data shown Figure 3-9 shows that the vertical deflection may increase by up to 20% with respect to the average support condition at any one site. Such variation will also highly influence the bending stresses in rail along the track and highlight the importance of consistent support stiffness.

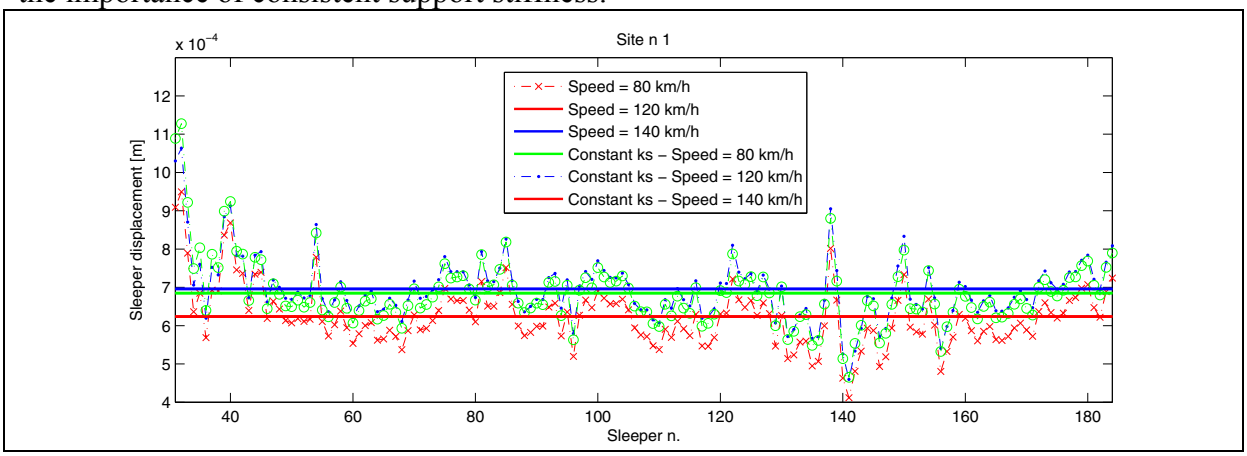

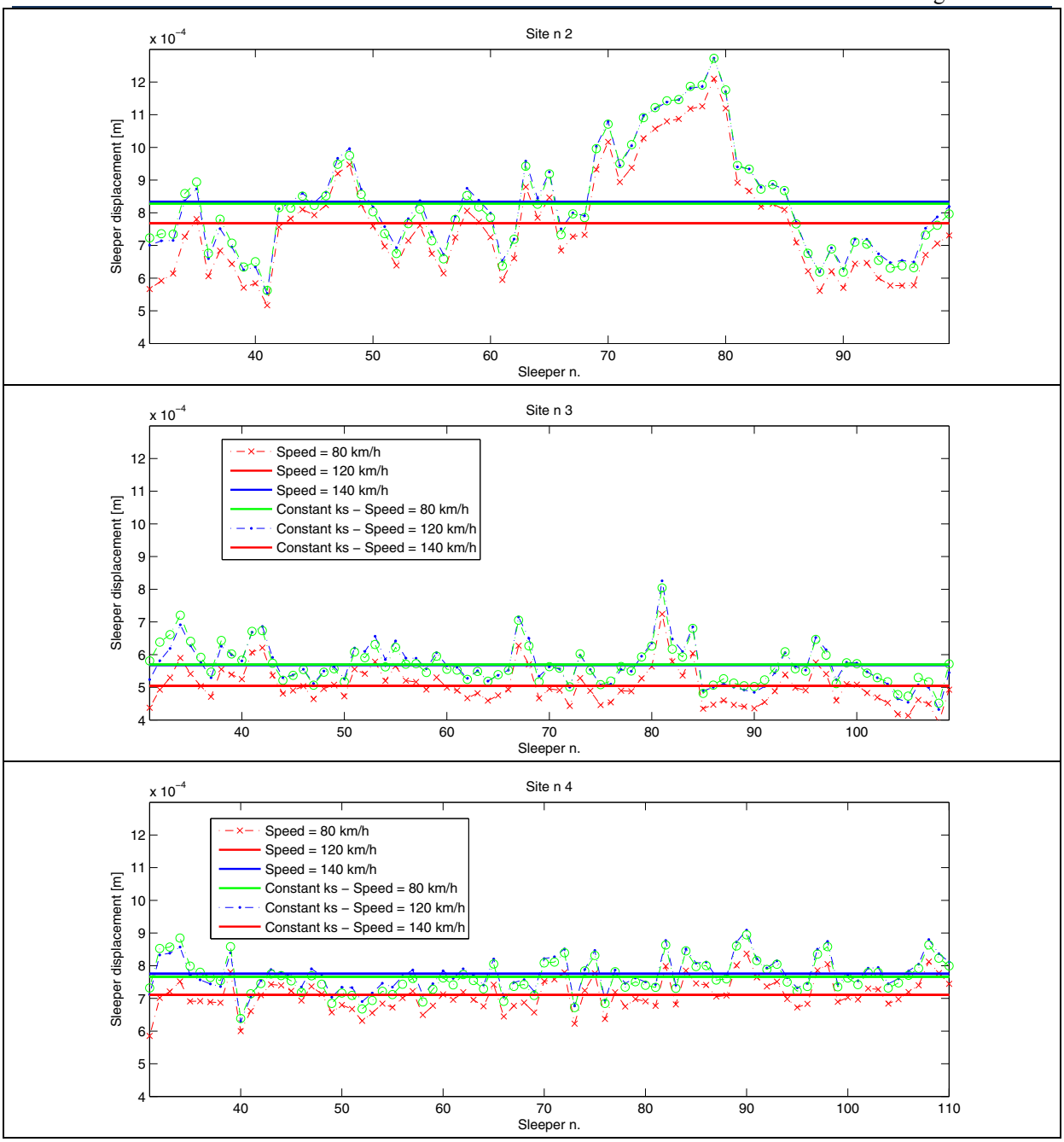

Figure 3-9: Selected distribution of the sleeper displacement for site 1, 2, 3 and 4 (from top to bottom)

In Figure 3-10 is used identify a correlation between the sleeper support stiffness and the sleeper displacements. The expectation is that as the support stiffness increases the sleeper displacement decreases, and this is mostly true for sites where the stiffness tends to be low (site 2 and site 4) which both show a correlation coefficient up to 22 and 26% respectively. For the stiffer sites the correlation is very low but the displacement is also very low, so that a correlation is mathematically difficult to achieve. It has to be noted that at any sites the maximum displacement does not necessarily coincide with location of low/poor support but the high points are often occurring at location of average support. In reality the correlation can be quite non-linear as there could be a spatial shift between low support and observed maximum deflection depending on adjacent sleepers support configuration, rail bending stiffness and also vehicle speed.

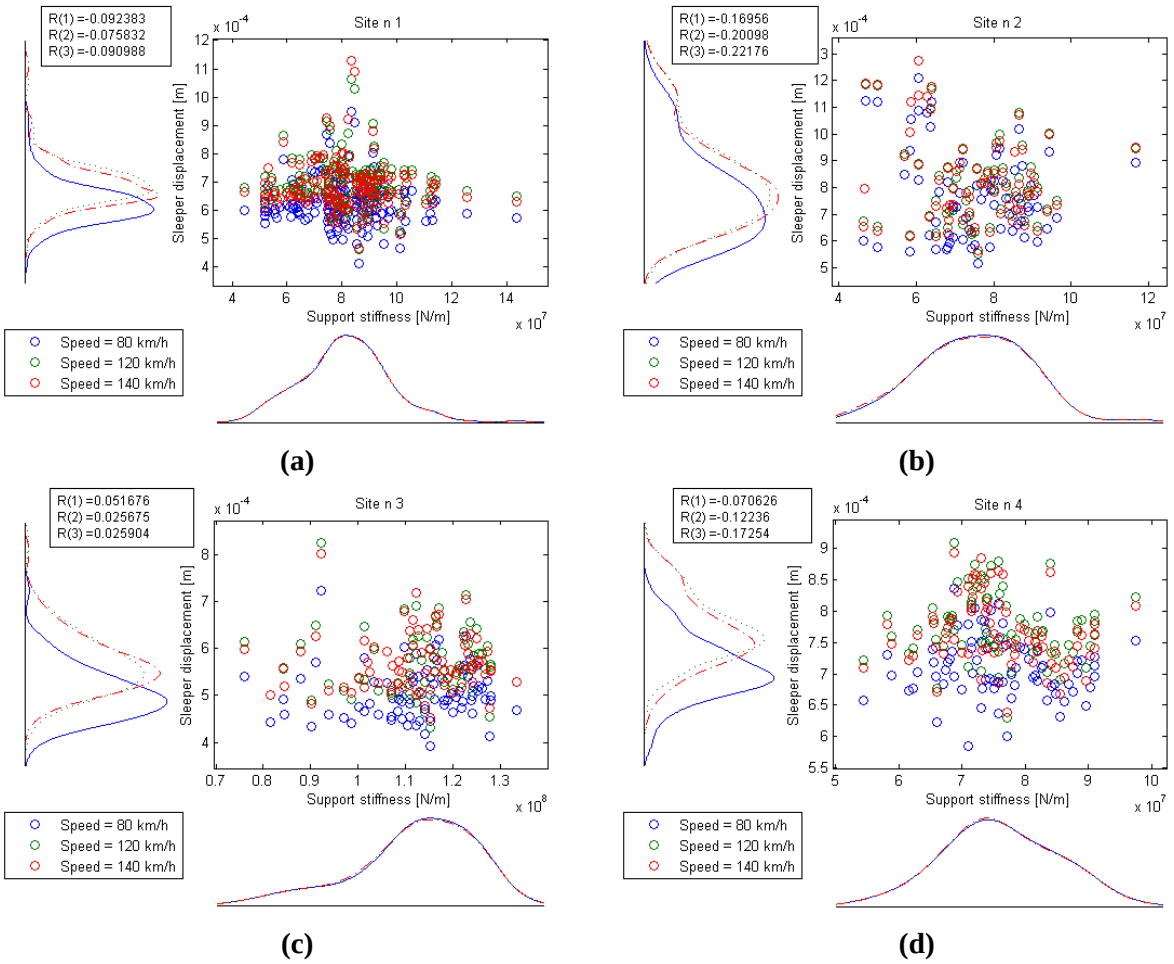

Figure 3-10: Distribution of the sleeper displacement versus distribution of stiffness support: (a) site 1; (b) site 2; (c) site 3; (d) site 4

3.2.3.3 Sleeper acceleration

Figure 3-11(a) shows the distribution of the sleeper acceleration versus speed per each site considered and Figure 3-11(b) the percentage difference with the mean values, which are reported in Table 3.4.

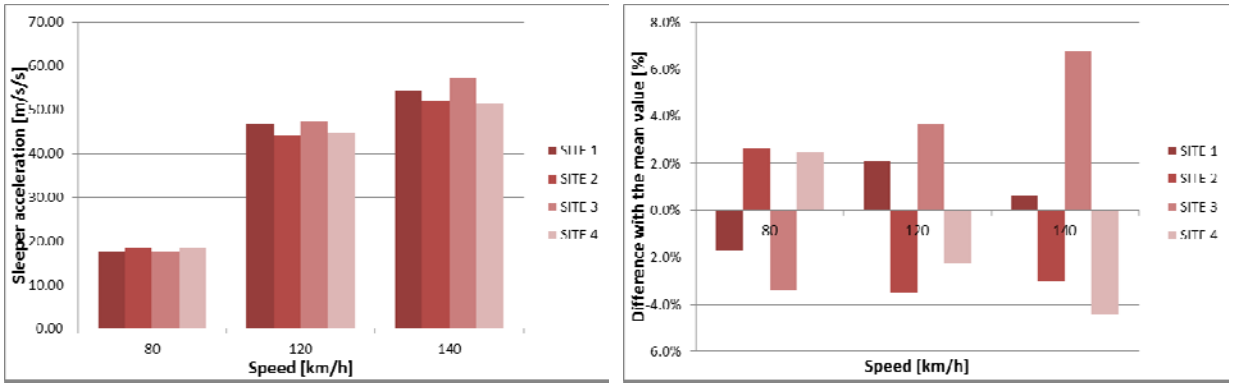

Figure 3-11: (a) Sleeper acceleration versus speed varying the site; (b) Percentage difference of sleeper acceleration with the mean value versus speed varying the site.

Speed [km/h]	Sleeper acceleration mean value [m/s/s]

80	18.07
120	45.78
140	53.88

Table 3.4: Mean values of sleeper acceleration depending on the speed

There is an obvious increase of sleeper acceleration with increasing speed, and rising the speed from the lowest value (80 km/h) to the highest (140 km/h) there is an increment of circa 200% in the rail acceleration. On the other hand, the differences observed due to the site support stiffness characteristics not as pronounced (between -4% and +8%), as shown in Figure 3-11(b).

In Figure 3-12 a sequence of distribution of sleeper acceleration in the space domain is presented, highlighting the large variation in vertical acceleration along the track.

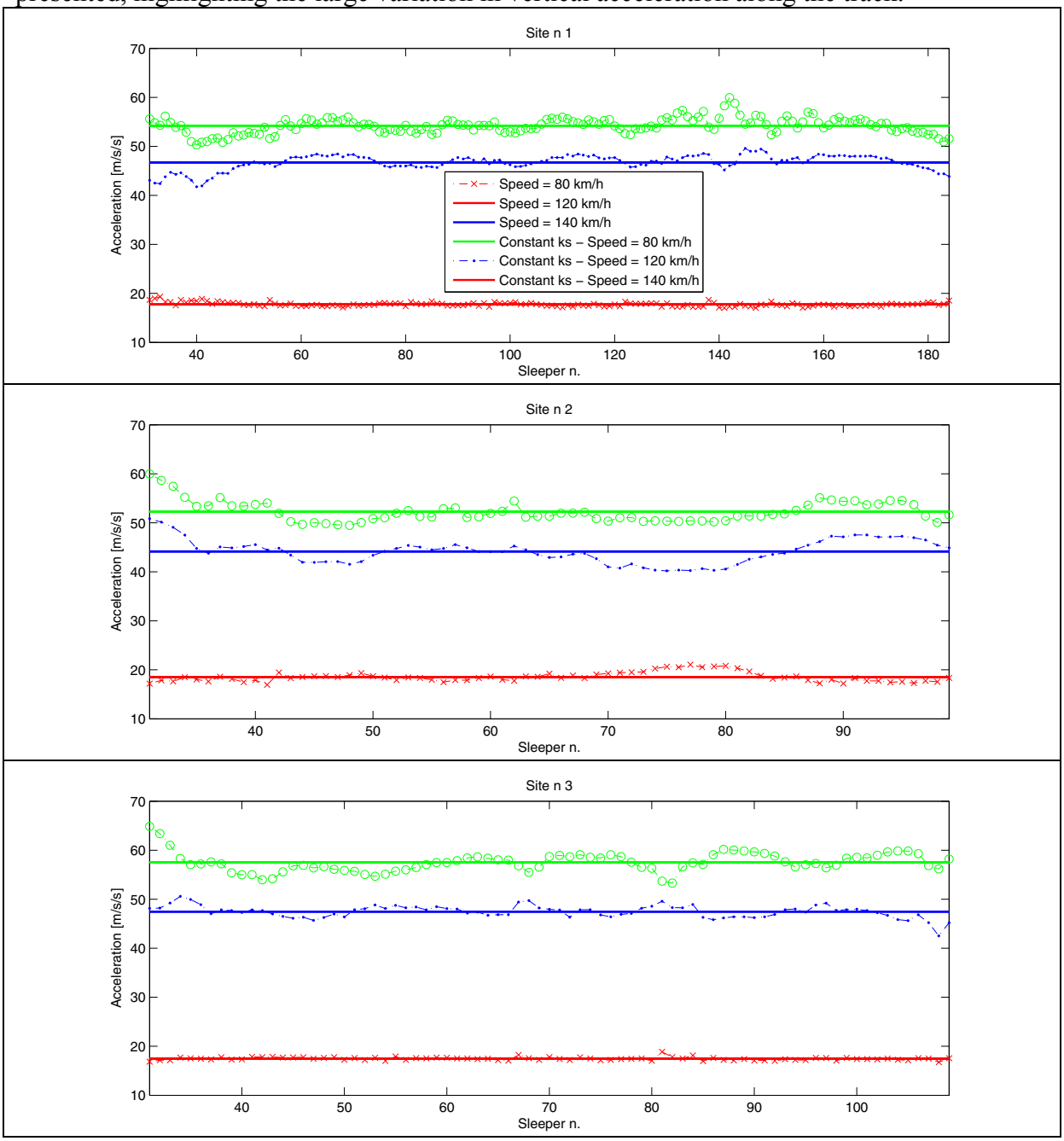

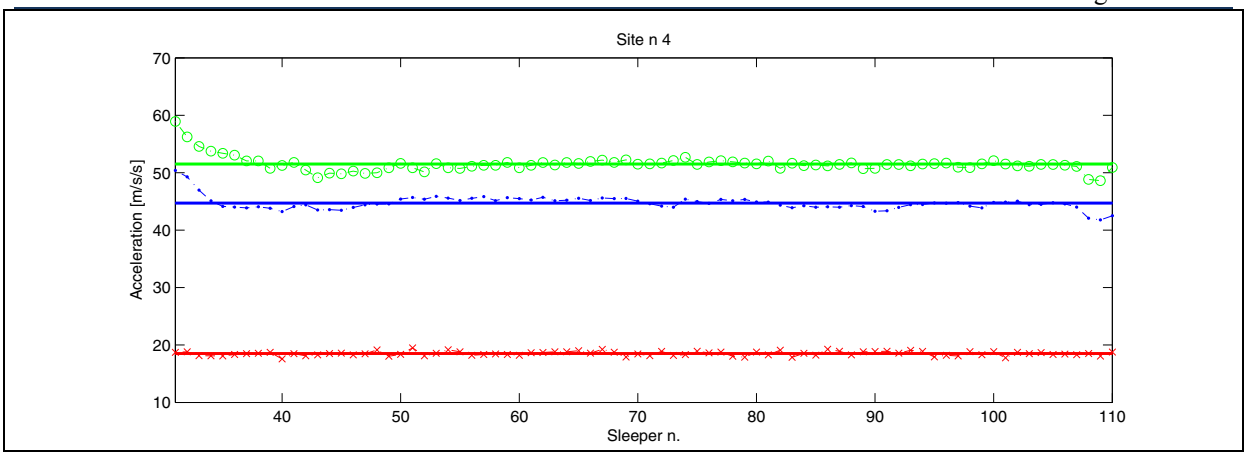

Figure 3-12: Selected distribution of the sleeper acceleration for site 1, 2, 3 and 4 (from top to bottom)

Figure 3-13 is used identify a correlation between the sleeper support stiffness and the sleeper accelerations. As explained before the acceleration are mostly a function of the vehicle speed rather than the support stiffness and the peak acceleration. It can however be observed that as the speed increases the variation in acceleration level also increases (higher SD value).

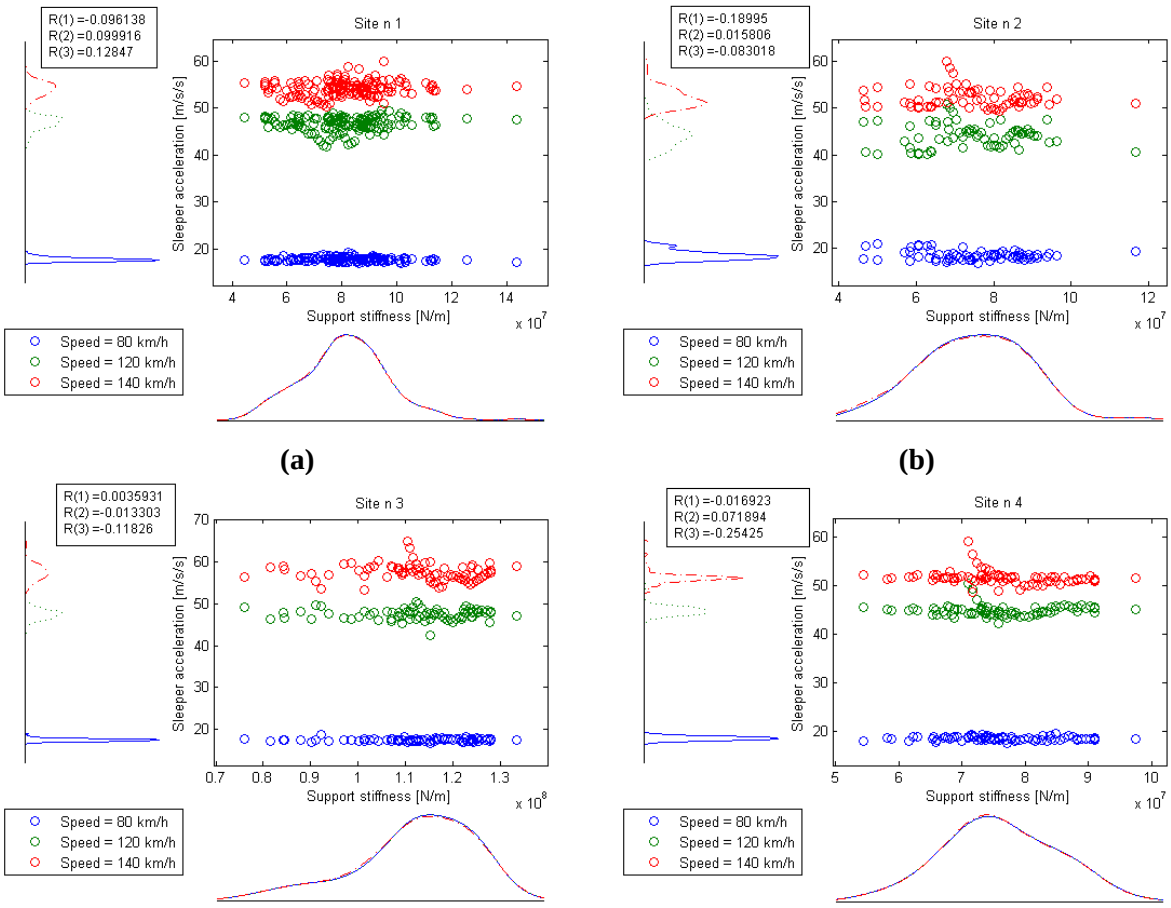

Figure 3-13: Distribution of the sleeper acceleration versus distribution of stiffness support: (a) site 1; (b) site 2; (c) site 3; (d) site 4

3.2.3.4 Rail stresses

In this paragraph, a quick calculation of rail stresses is presented. Even if the Timoshenko beam theory has been applied to establish the system model, in this section the more simple bending theory by Euler-Bernoulli has been used and the longitudinal bending stresses are given as[7]:

$$\sigma_{xx} = -\frac{M \cdot Z}{I}$$

Where M is the bending moment, expressed in function of the bending beam properties and the bending angle, Z the distance between the neutral axis and the foot and I the section inertia. This methodology has been validated against the Beam on Elastic Foundation (BOEF) equation using a single moving load on an equivalent constant support. The predicted stresses are very similar, with a maximum difference of about 0.75%.

Figure 3-14 show an example from site 2 of rail bending stress plot. The maximum negative and positive stress values are recorded, as well as the maximum differential stress Δσ, which is considered in the following.

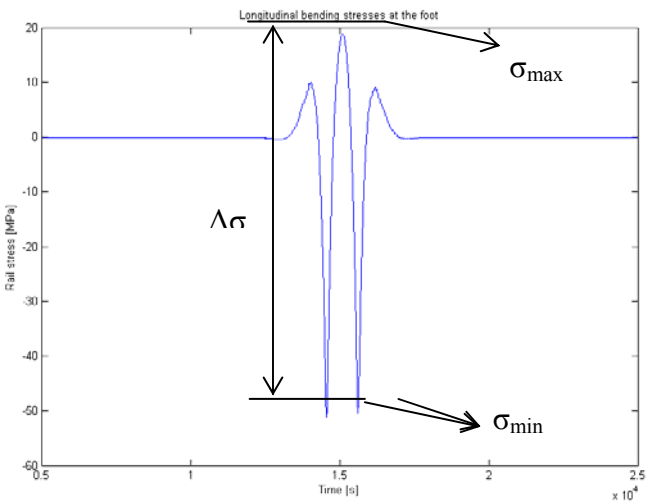

Figure 3-14: Example of rail bending stress.

Figure 3-15(a) shows the distribution of the rail stress versus speed per each site considered and Figure 3-15(b) the percentage difference with the mean values, which are reported in Table 3.5.

[7] Y. Bezin (2008), "An integrated flexible track system model for railway vehicle dynamics", PhD thesis, Manchester Metropolitan University, p. 92.

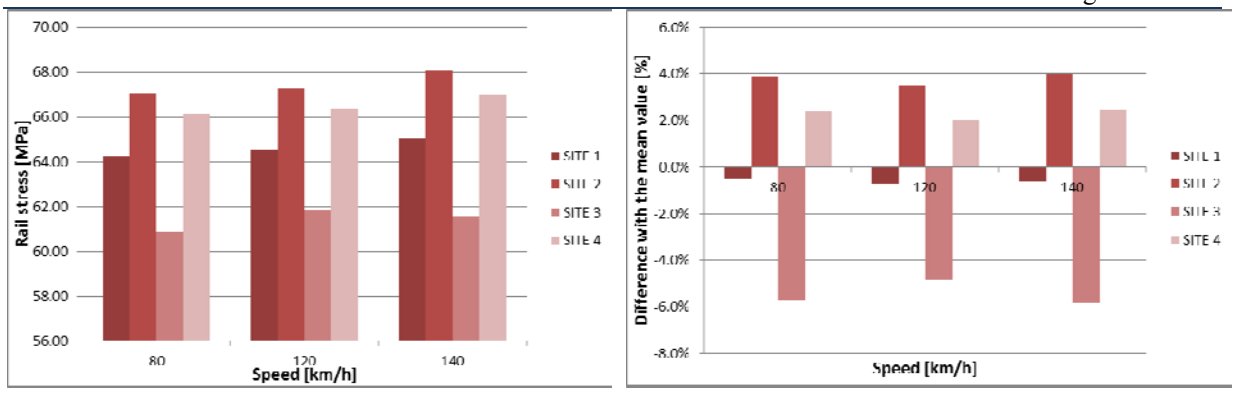

Figure 3-15: (a) Rail stress versus speed varying the site; (b) Percentage difference of rail stress with the mean value versus speed varying the site.

Speed [km/h]	Rail stress mean value [MPa]
80	64.55
120	65.02
140	65.42

Table 3.5: Mean values of rail stress depending on the speed

Little variation in rail stresses is observed as a function of the increasing speed. On the other hand the maximum bending stresses are significantly affected by the support conditions as expected, with increase stresses on lower support stiffness.

In Figure 3-16 a sequence of distribution of rail stress in the space domain is presented. It can be observed from this that the rail bending stresses are more constant that other quantities observed so far.

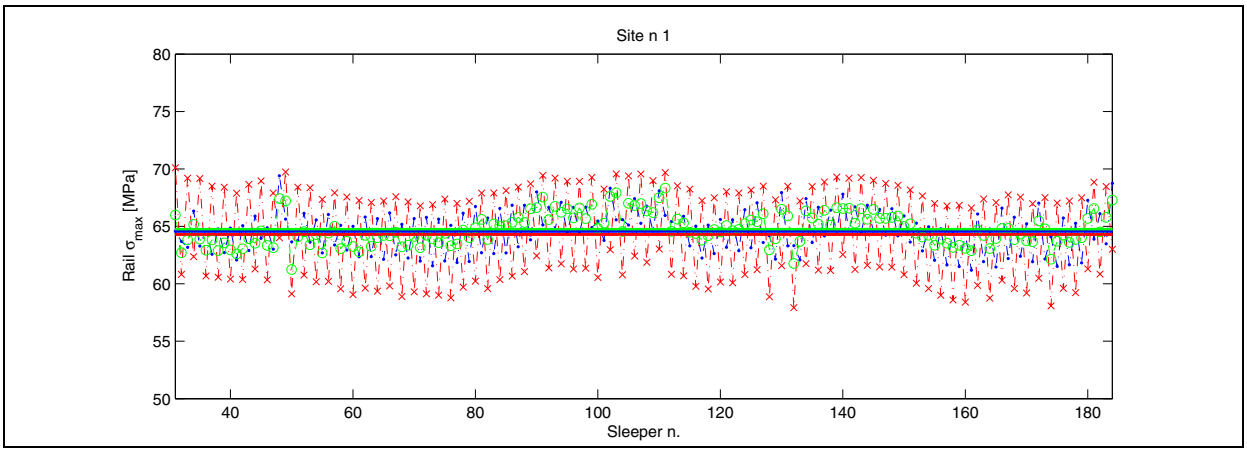

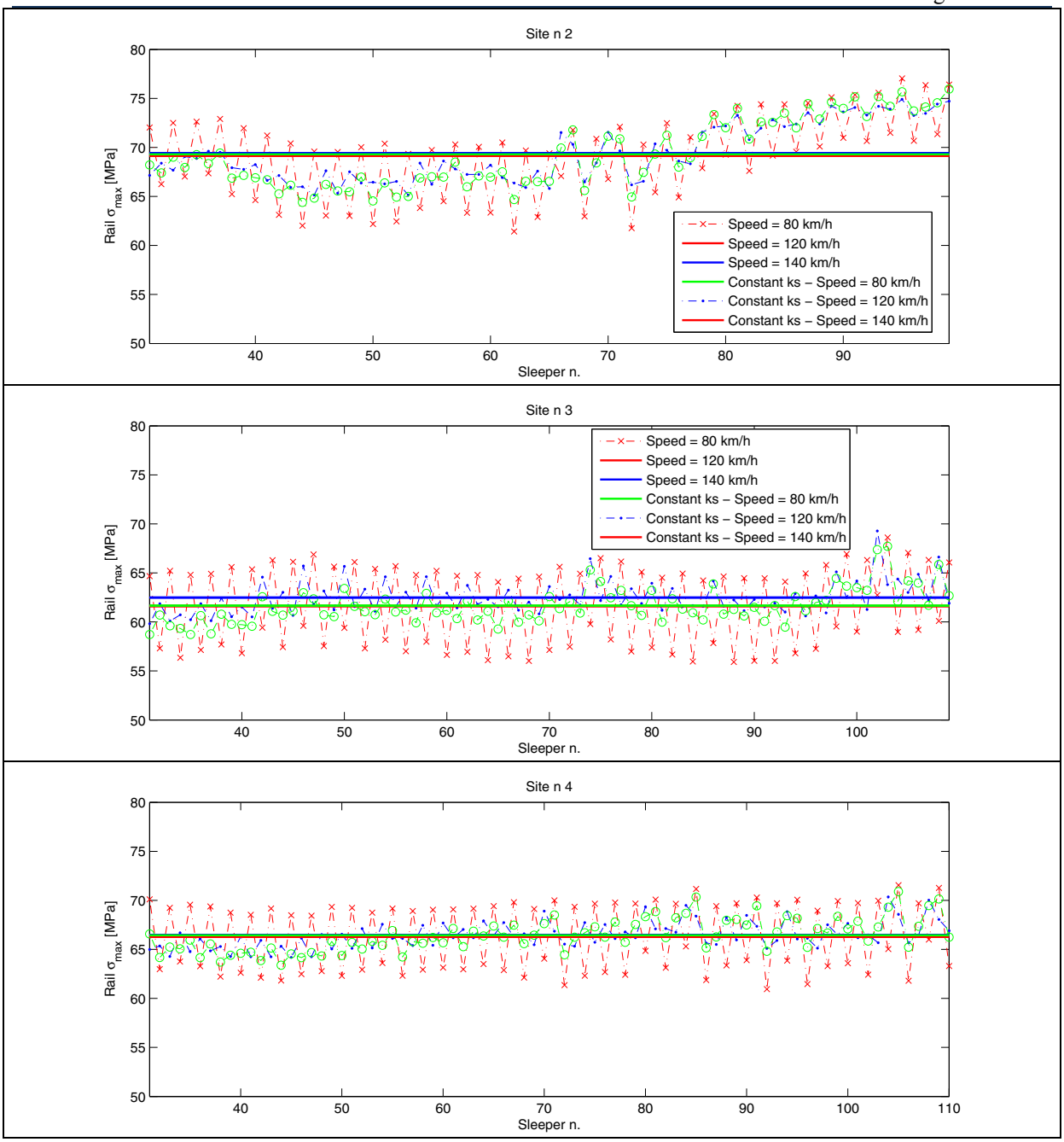

Figure 3-16: Example of distribution of the rail stress for site 1, 2, 3 and 4 (from top to bottom)

Figure 3-17 is used identify a correlation between the sleeper support stiffness and the rail bending stresses. One oddity observed with respect to previous quanities is that in the case of low speed (80 km/h) there are two main peaks in teh data distribution. The highest corresponds to the nodes between two sleepers while the lowest corresponds to the nodes above sleeper. This phenomena can be explained with the fact that the low speeds allow the rail to bend more in the unsupported space, so that the stresses are higher. Reciprocally as the speed increases the vehicle wheel tends to see a more homogenous support as the unsprung mass inertia 'flies' over the unsupported sleeper bay. In case of low support stiffness (site 2) the same oberservation can be made also at the higher speeds.

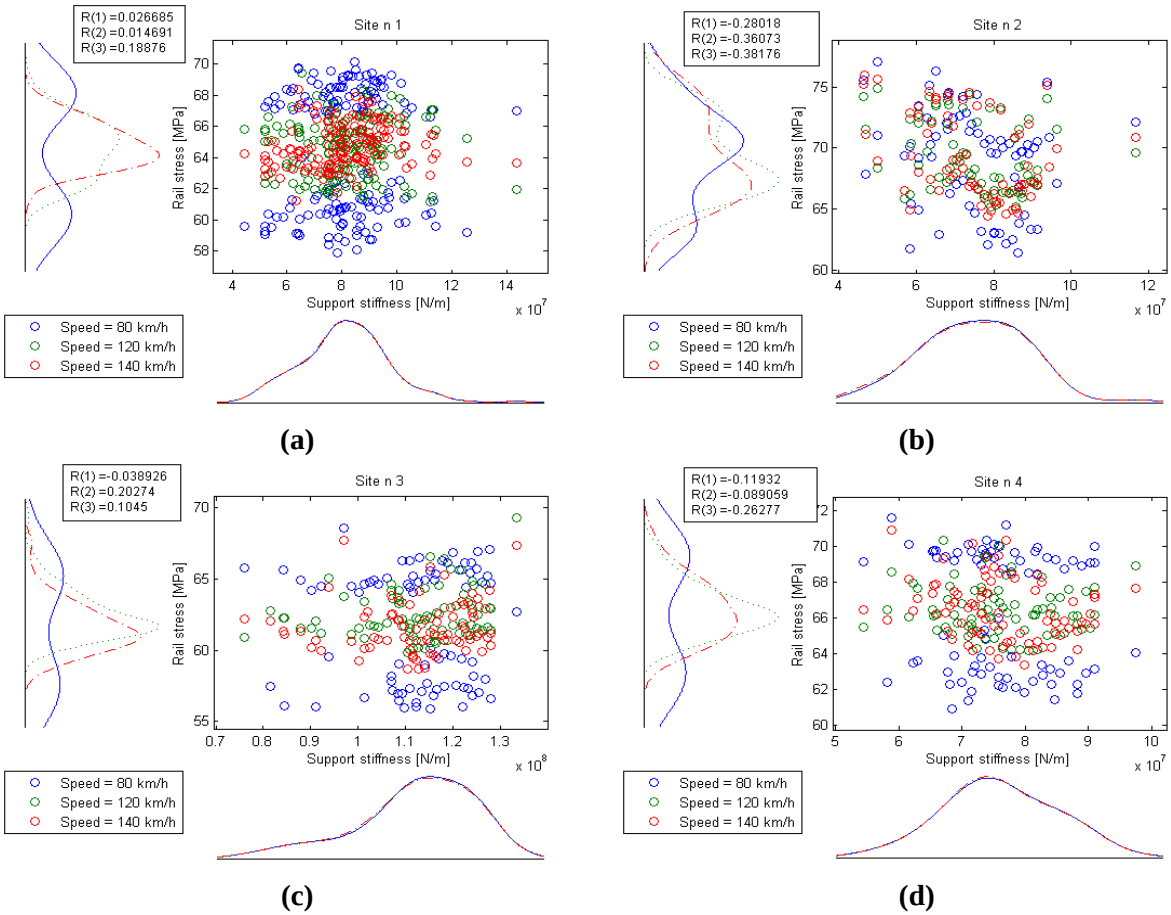

Figure 3-17: Distribution of the rail stress versus distribution of stiffness support: (a) site 1; (b) site 2; (c) site 3; (d) site 4

3.2.4 Conclusions on section 3.2

In this section a vehicle-track interaction model has been used to determine the influence of track support stiffness on track response using variuous quantities of interest: ballast force, sleeper displacmeent, sleeper acceleration and rail stresses. It has been shown that degraded support leads to increased rail bending stresses and risk of rail break as well as higher sleeper accelerations. On the other hand the increased sleeper stiffness has a direct link to increased ballast force and pressure wich can increase the ballast degradation. More importantly this study has shown that variation in support stiffness over the lenght of the track can leads to a high variation in ballast force and acceleration and therefore give rise to differential settlement of the track (i.e. degradation of top level). Finally it has been show to be imporant to manage the consistency of ballast support stiffness as the vehicle speed increases, in order to manage the rate of degradation and the differential settlement.

3.3 The effect of track support stiffness on track behaviour and key components based on Eurobalt reference values

Aim of this section is to analyse the effect of changes in the track stiffness on the loads generated in the main track elements: rails, fasteners, sleepers. In the same way as done in Section 2.3 for a “typical” track. This analyses is carried out based on the numerical simulation of train-track interaction considering a detailed Finite Element model of the track. This work was performed by POLIMI, using input from HUD and KTH regarding the loading cases to be considered.

Due to the limited resources available, this analysis is confined to comparing the results of the typical case presented in 2.3 with a "stiff track" case according to data available for the EUROBALT project. The comparison is carried out for the nominal vehicle condition and for the maximum vehicle speed, i.e. 140 km/h for 17 t axle load and 120 km/h for 22.5 and 25 t axle load.These results in combination with thoses presented in the previous sub-section 3.2, allows a better interpretation of the effect of stiffness support for a wider range of representative values from soft to stiff.

3.3.1 The model of train-track interaction

The models used for the analysis reported here are the same as already described in 2.3. However, some parameters of the Finite Element model of the track were modified to consider the "stiff" track case instead of the "typical" track case as done in2.3.

To this aim, the following data were modified:

Rail fasteners: stiffness and damping of the rail fasteners were defined based on values measured in the EUROBALT project, cf. Table 2.9, considering the "Stiff" case. Therefore, the rail pad is assumed here to have a stiffness of 1000 kN/mm and a viscous damping of 50 kNs/m.

Ballast and embankment: The ballast and embankment stiffness parameters k_b and k_e were obtained from those used in 2.3 by applying a scaling factor of 2.5, which is the ratio of the trackbed stiffness for the "stiff" and "typical" track according to EUROBALT data. The damping parameters for ballast and embankment c_b and c_e were obtained from k_b and k_e respectively using the same proportionality ratio as used in 2.3:

$c_e / k_e = 1.25$

with stiffness values expressed in MN/m and damping values in kNs/m.

The ballast mass parameter was not changed.

3.3.2 Results

In this section, the results obtained for the "stiff" track are compared to the results for the "typical" track already presented in Section 2.3. The comparison is limited to the maximum speed considered in association with each axle load value.

Table 3.6 summarises the comparison of in terms of overall maxima of the quantities observed. The increase of track stiffness leads to a significant increase of the rail seat loads and sleeper-ballast contact pressure, in the order of +16 – 20%. This is due to the fact that a stiffer track is less efficient than a more deformable one in distributing the wheel loads on a relatively large portion of the track. Therefore, the amount of load applied on the sleeper directly interested by the presence of a wheel is increasing for increasing track stiffness. On the other hand, from a quasi-static point of view, a stiffer sleeper support leads to lower bending moment in the rails. This is the reason why the bending stresses in the rail are lower for the stiff track case, especially for the 22.5 and 25 t axle load.

		17 t/axle V=140 km/h	**22.5 t/axle** V=120 km/h	**25 t/axle** V=120 km/h
Rail seat load	Typical track	42.8 kN	52.8 kN	56.9 kN
	Stiff track	51.0 kN	61.6 kN	67.9 kN
SBCP	Typical track	115.0 kPa	140.8 kPa	153.0 kPa

	Stiff track	136.6 kPa	163.0 kPa	179.1 kPa
Rail stress	Typical track	98.8 MPa	90.5 MPa	113.5 MPa
	Stiff track	96.7 MPa	86.4 MPa	93.9 MPa

Table 3.6: Comparison of maximum rail seat loads, sleeper-ballast contact pressure (SBCP) and rail stresses for a "typical" track and "stiff" track.

Conclusion on section 2.3

In conclusion, it is shown by this analysis that changes in the track stiffness may lead to significant differences in the mechanical behaviour of the track at train passage. A more resilient sleeper support is beneficial to reduce sleeper loading and to achieve a better distribution of train loads on the ballast and on the lower layers of the track substructure. However, a decrease of the sleeper support stiffness results in higher bending stresses in the rail, and therefore the use of very flexible sleeper support should be carefully checked against this potential problem.

The analysis presented here considers the stochastic effect caused by track irregularity, but assumes a uniform stiffness for the track, with the aim of defining the trend of some indicators for track loading with changes in the track stiffness. However, further variability of track loads can be expected as the result of non-uniform track stiffness, as investigated in Section 3.2.

4. TASK 4.1.3 - DEVELOP MINIMUM ACTION RULES APPROACH TO OTHER DEFECTS AND FOR NEW TECHNOLOGIES (TATA STEEL)

4.1 Scope of Work

The scope of work for this portion of the Sustrail project was to expand the Minimum Action methodology into additional defects/rail regimes.

In the following sections, the choice of new defect, background and details of the Minimum Action model and the results of work are discussed.

4.1.1 Problem Statement

Due to its importance in track maintenance, foot corrosion was chosen as a suitable defect to apply the Minimum Action model to.

Corrosion defects can have a large bearing on the life of a rail. For example fatigue cracks can be initiated by pitting on the rail foot as seen in Figure 4-1.

Figure 4-1 - An example of a fatigue crack in the foot of a rail

In addition to this, corrosion can cause a reduction in the area of the foot of the rail (see Figure 4-2), thereby changing the cross-section.

Figure 4-2 - Loss of foot area from corrosion

This cross section change results in modifications to the moment of inertia and other physical properties of the steel, which influence crack growth.

The final key aspect of corrosion related foot defects is that they are extremely hard to detect, only being visible through the web of the rail from the head. Therefore any opportunity to predict the life of rails in a corrosion prone environment is beneficial.

As such the effects on crack growth of this reduction in area, caused by corrosion, will be investigated using the Minimum Action model.

4.2 Introduction to Minimum Action Model

The Minimum Action program was developed as part of the INNOTRACK project. The software calculates the wheel impact force and predicts the breakage risk associated with cracks in rail foot[8]. The program looks at the growth rate of an existing crack initiated under traffic and correlates it with the inspection cycle to yield the probability that the crack will be detected and the size of the crack at failure or detection. To better demonstrate what the program can do, Section 4.2.1 specifies the input values required and Section 4.2.2 explains the output of the program.

4.2.1 Input

The most recent version of the program is Minimum Action II version 0.4. The required data to run the simulation are:

- Track type including moment of inertia, Young's modulus, fracture toughness, sleeper stiffness and sleeper spacing are required.
- Traffic pattern, which is the amount of vehicle running through the track per day. The type of vehicle is described by the number of axles, the axle position and the axle load.
- Inspection period and the probability of detection curve: Inspection period is the number of days in which the track is inspected routinely. The probability of detection

[8] Smith, L; Allen, R.; Jaiswal, J; "A scientific approach to Minimum Action", 2009, 8th International Conference on Contact Mechanics and Wear of Rail/Wheel Systems, Italy

curve is a graph showing how likely an inspector can detect a crack at a certain size, see 4.2.3.3.

- The initial defect size, including depth ‘a’ and size ‘c’ in millimetres (see Figure 4-3 . The program will calculate the changes in size of this existing crack in the rail foot through time. This initial defect could in fact be a corrosion pit, whereby the localised stress is increased due to the defect, acting as a stress raiser leading to crack growth.

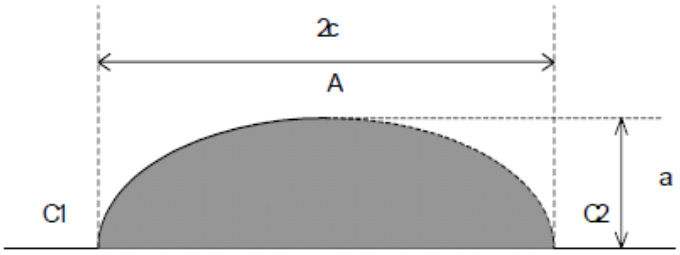

Figure 4-3 - Crack geometry

The user can request the program to run the simulation a number of times. This function is useful when ‘Randomisation’ is chosen. This Randomisation option is detailed below.

A database of common track type, sleeper and vehicle type has been built in to allow the user to pick from the dropdown boxes their scenarios. In the case of uncommon input values, users can add the values in themselves.

4.2.2 Output

Detailed results are listed in a commentary file available for viewing (see Figure 4-4). The most important output of the program is the crack size ‘observed’ through each inspection period. At the end of the commentary file, a summary of all the repetition is included.

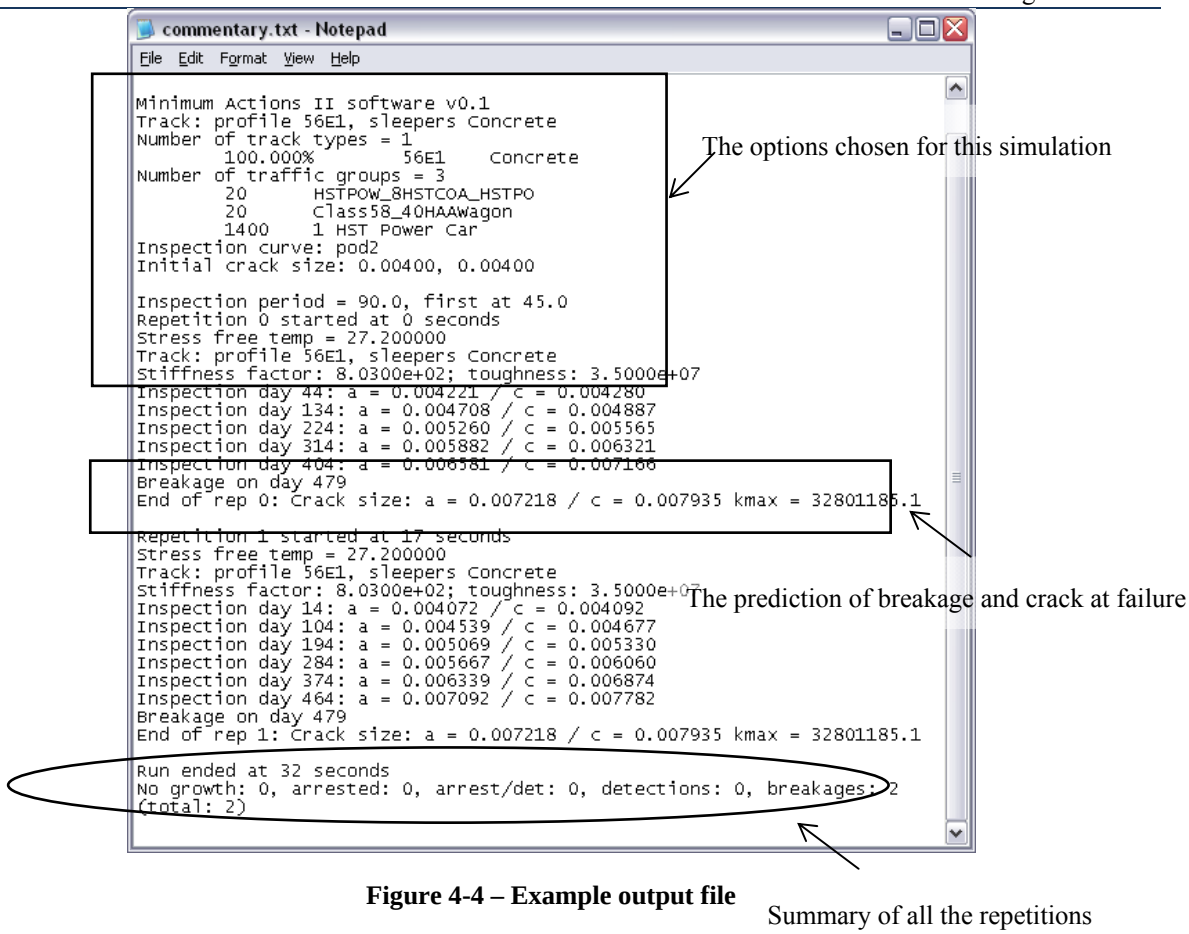

Figure 4-4 – Example output file

4.2.3 Other aspects of the program

4.2.3.1 Randomisation

Randomisation option if chosen will enable the probability based randomisation on a number of variables such as traffic sequence and standard deviation of the input values for every repeated run. As a result, although the result is not repetitive, it will reflect a more realistic estimation of the track behaviour. This is a fundamental part of the theory behind the Minimum Action model, and is used to produce a "statistical distribution of residual life… and thus the risk associated with specific inspection regimes and minimum action timescales"[1].

4.2.3.2 Simulating a complex route with different track types

In reality, a route of interest would consist of various rail grades and/or a mixture of sleeper type. The Minimum Action program allows these differences to be taken into account in the calculation.

4.2.3.3 Crack Probability of Detection

The Probability of Detection (PoD) is a critical parameter in the model. It provides the model with the data to determine whether a crack has been detected or not. A large amount of research can be found on PoDs[9] from many different industries. A PoD curve describes the relationship between a crack size and its probability of detection. This can be influenced by

[9] RR454 - Probability of Detection (PoD) curves Derivation, applications and limitations, HSE Report 2006. Available from http://www.hse.gov.uk/research/rrhtm/rr454.htm

many things such as material type or inspection tools or techniques (e.g. magnetic particle inspection). For the Minimum Action model, a curve was produced that matches the experience of Tata Steel during track inspection. The curve used can be seen below.

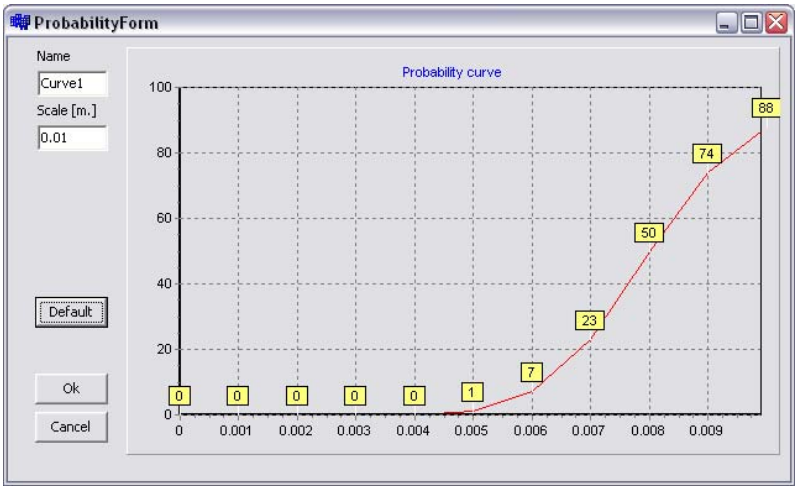

Figure 4-5- Probability of Detection Curve for Minimum Action Model

When a crack is simulated in the model this curve is used to determine the likelihood of its detection at each inspection.

4.3 Methodology

Foot corrosion causes reduction in the foot area, which affects the moment of inertia of the rail profile. Depending on the level of corrosion, the moment of inertia of the track can be recalculated and entered in the track values. An example of reduction in foot area due to corrosion is illustrated in Figure 4-6.

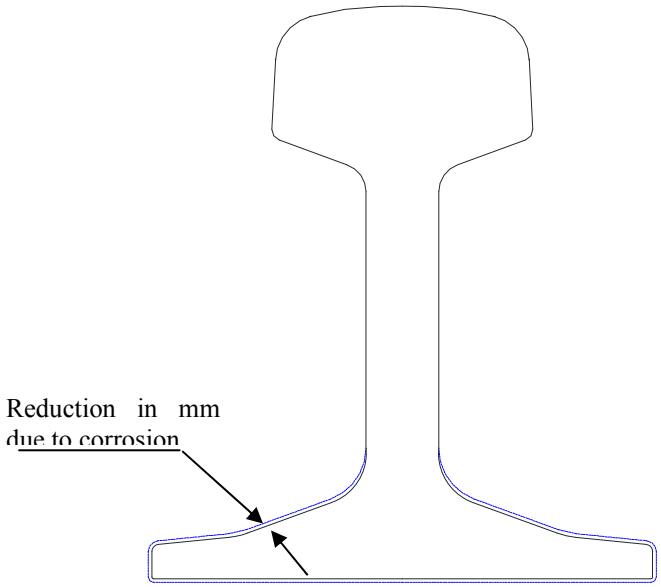

Figure 4-6 - Example of modelled foot corrosion

To model the effects of a reduction in foot area, three rail profiles were built in CAD, with varying corrosion levels of 0.5, 1 and 2mm. The physical properties of these new profiles were calculated and entered into the program. While these corrosion patterns are simplified,

comparison between the four states should provide insight into the influence of corrosion on crack propagation.

4.3.1 Test Parameters

To enable a simple comparison of the different foot profiles, a basic set of test parameters was used to enable quick comparisons.

Parameters	Value input	Justification
Vehicle type	Single axle train with 15 kN wheel force. For ease of communication, this vehicle type is called 'Static Test' train during the test case.	This vehicle type was chosen for simplicity. With the single axle train, the axle spacing and inter-axle interaction can be ignored
Track grade	220	
Sleeper type	Concrete	Typical track construction
Traffic pattern	2000 of Static Test train per day	
The initial crack size	0.002 x 0.002 metre	All values were input using SI units.
Inspection period	90 days	Three-month period is reasonable to monitor the growth of a 2 mm crack
Randomisation	Off	To enable fast runs

Table 7 - Basic input parameters

4.4 Results

4.4.1 Simulation result of 56E1 track

The simulation results of 56E1 track are shown in Figure 4-7.

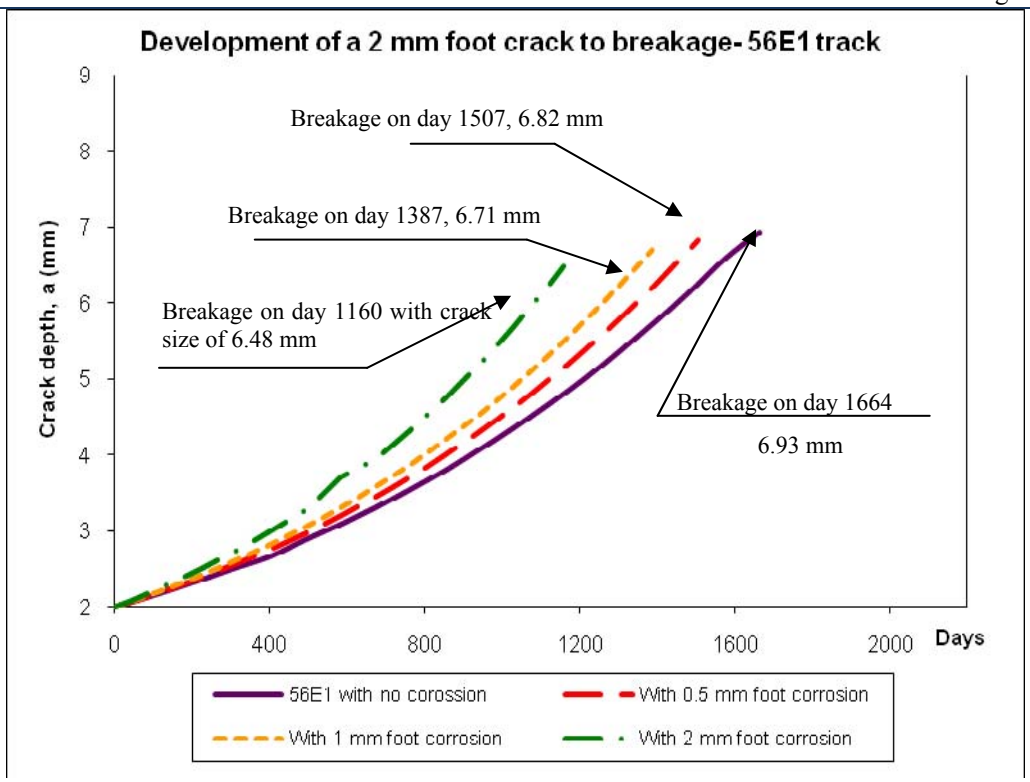

Figure 4-7 - The growth of a 2 mm crack on 56E1 track with different levels of reduction in foot area due to corrosion

It was predicted that in this test case, the track would break when the crack depth was less than 7 mm, which has less than 25% chances of being detected (see 4.2.3.3).

The result shows that the crack grows faster with increased level of foot corrosion. Rail tracks with greater amount of foot corrosion would break earlier than a normal track. With 2000 StaticTest trains per day, a 56E1 track with 2 mm foot reduction due to corrosion could break over a year sooner. In the case of severe wheel impact, the track life will be shorter.

Foot corrosion reduces the moment of area of the track, which in turn increases the stress force on the remainder of the track. This explains why the crack size at failure for corroded track will also be smaller.

Results of the test case are summarised in Table 8.

Reduction in foot area due to corrosion	**Crack size at failure (mm)**	**Life from 2 mm crack (day)**	**Reduction in life comparing to no foot corrosion (from 2mm crack)**	
			Days	%
0	6.93	1664	0	0%
0.5 mm	6.82	1507	157 (more than 5 months)	6.43%
1.0 mm	6.71	1387	277	16.65%

			(more than 9 months)	
2.0 mm	6.48	1160	504 (more than 15 months)	30.29%

Table 8: Summary of test case result showing the crack size at failure and the reduction in life of 56E1 track with different level of foot corrosion

4.4.2 Simulation result of 60E2 track

The simulation was repeated with the same parameters for 60E2 track with different level of foot corrosion. Figure 4-8 illustrated the effect of foot corrosion on the crack growth and the overall track life of 60E2 track.

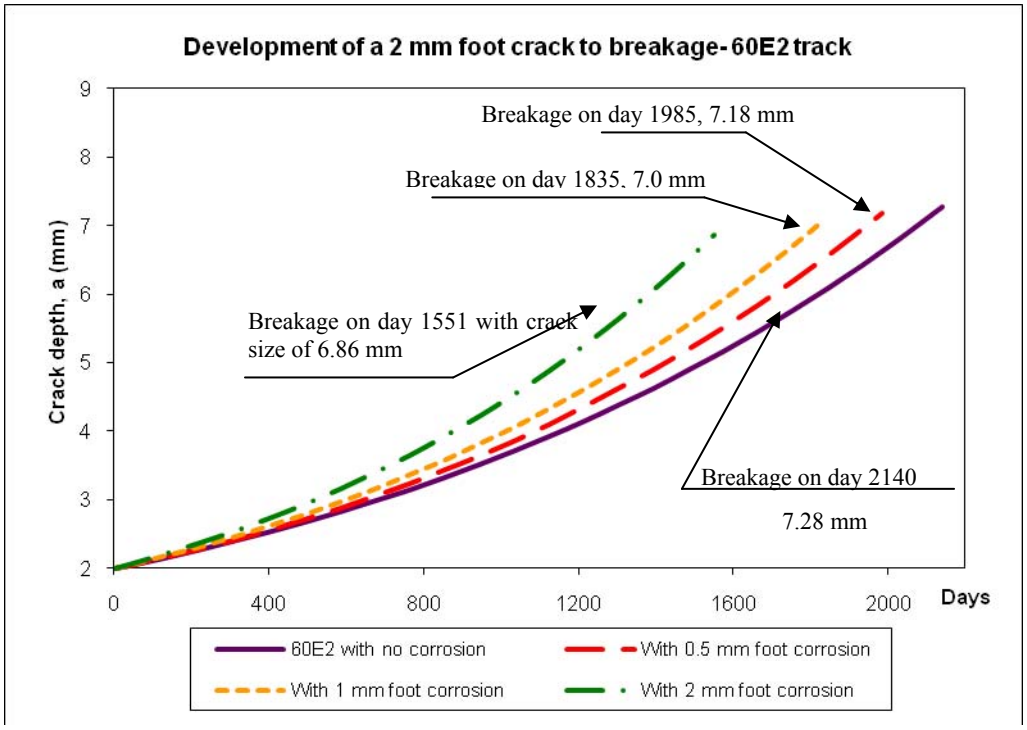

Figure 4-8 - The growth of a 2 mm crack on 60E2 track with different levels of reduction in foot area due to corrosion

Similarly to 56E1 track, 60E2 track also experiences breakage at a crack depth with less than 25% chance of detection. The trend of crack growth rate under the influence of foot corrosion level is the same as with 56E1 track. Results of the test case were summarised in Table 9.

Reduction in foot area due to corrosion	Crack size at failure (mm)	Life from 2 mm crack (day)	Reduction in life comparing to no foot corrosion (from 2mm crack)	
			Days	%
0	7.28	2140	0	0%
0.5 mm	7.18	1985	155 days (more than 5 months)	7.24%
1.0 mm	7.08	1835	305 (more than 10 months)	14.25%
2.0 mm	6.86	1551	589 (more than 1.5 years)	27.52%

Table 9: Summary of test case result showing the crack size at failure and the reduction in life of 60E2 track with different level of foot corrosion

4.5 Discussion

4.5.1 56E1 and 60E2

The simulation predicts that in this test case, 60E2 track would last longer than 56E1 track. This can be explained by comparing the cross section of the two rail profiles. Table 10 summarises the measurement of the two rail profiles. It is noticeable that the head and foot of 60E2 is much wider, making it more resistant to wheel load forces and reducing the effects of the corrosion factor due to the larger starting cross sectional area. Increase height also reduces bending stress for the same axle load.

Section	56E1	60E2
Height	158.75	172
Width of rail head	70.663	72.918
Width of rail foot	140	150

Table 10: Comparison between 56E1 and 60E2 profile

4.5.2 Probability of detection

The probability of detecting a crack depends on both the defect and the inspection system. The foot area is nearly impossible to inspect in service and the defect can only feasibly be found via ultrasonic means directly beneath the rail web. Any defect that does not lie centrally

in the foot, including corrosion pits and blemishes are very difficult to detect. Furthermore, factors of inspection system such as procedure, equipment, software, and operator capability also contribute in the low probability of crack detecting.

Minimum Action uses a probability curve based on Tata Steel experience in track monitoring and rail break investigations. Based on this curve, most of the simulations result in breakages with low chances of detection. This emphasises the benefit of using a simulation program to forecast the track health for a better and more accurate maintenance schedule.

4.5.3 Expansion to include randomisation

As discussed previously, the intrinsic power of the Minimum Action model comes from its use of statistically controlled random variables in repeated model runs, to produce a distribution of potential outcomes and associated risks of breakage.

An example of this can be seen below, where the randomisation option was enabled and 500 repetitions were carried out.

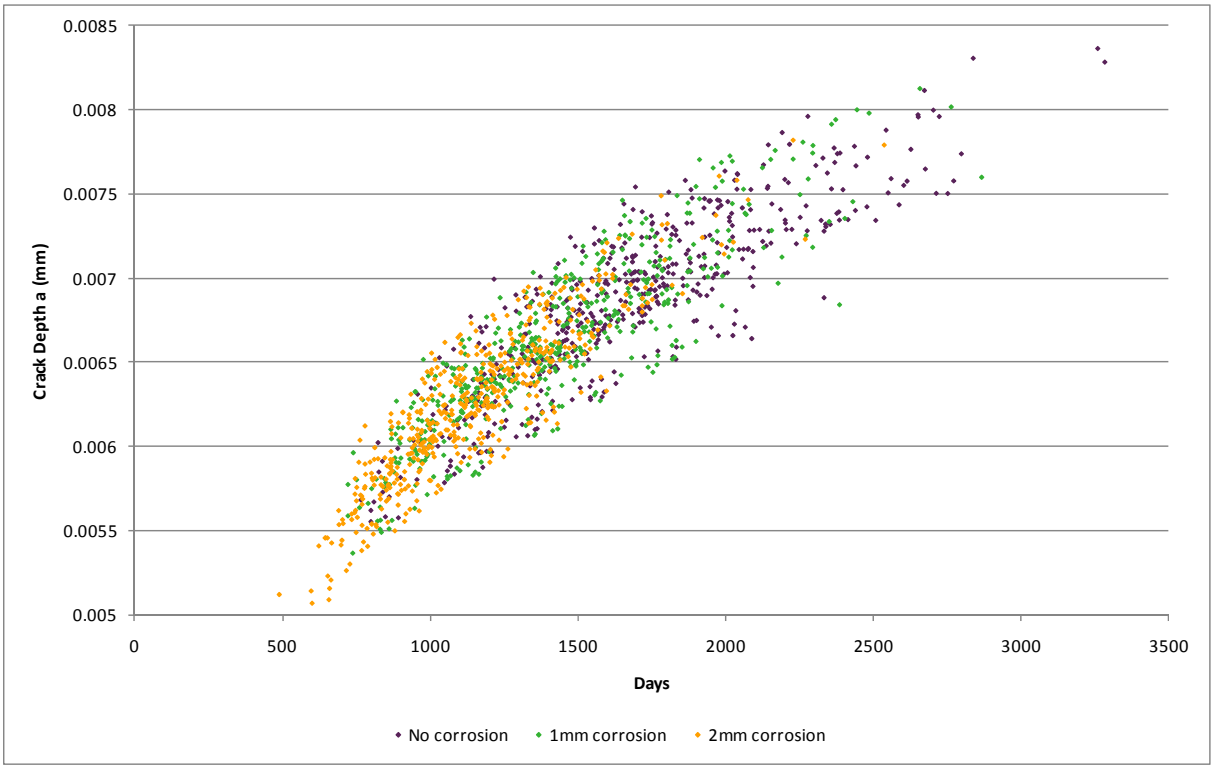

Figure 4-9 - Distribution of outcomes for varying corrosion levels

Figure 4-9 shows the distribution of crack depth and days to breaking for the 500 model runs with varying corrosion levels. This data is not used on its own, but combined with the inspection regime and probability of detection to determine an associated risk

It can be seen that the increase in corrosion level moves the distribution of results down and left, reducing both life before failure and crack length achieved before failure. This correlates well with the simple, unrandomised discussion above.

To compare the full results of the 500 randomised runs against the single unrandomised run, the data from all 500 runs is collated, and then averaged to give an average crack growth trend. This can be seen in Figure 4-10.

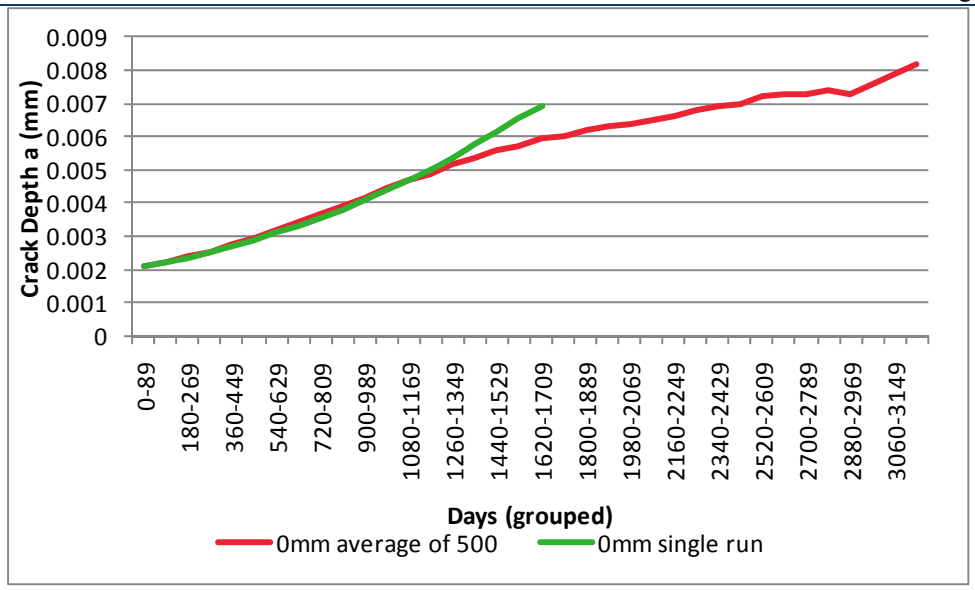

Figure 4-10 - Crack growth for randomised and unrandomised model runs with 0mm corrosion

Figure 4-10 shows the crack depth against the number of days. The inspection period is also a randomised element so the data must be grouped to avoid scatter.

It shows that at lower days passed and crack lengths, the single unrandomised run correlated very well to the full randomised data set. However at around 5mm crack depth the single run starts to deviate, suggesting a faster crack rate. This is evidence of the variability that the randomisation element is bringing to the model. Work in Innotrack[1] noted that in crack growth tests there can be a factor of 2 difference between replica tests. Minimum actions uses the 500 run data to statistically provide the risk associated with specific inspection regimes.

However the analysis in Figure 4-10 can be used to verify the above results by trending the data for the differing corrosion levels.

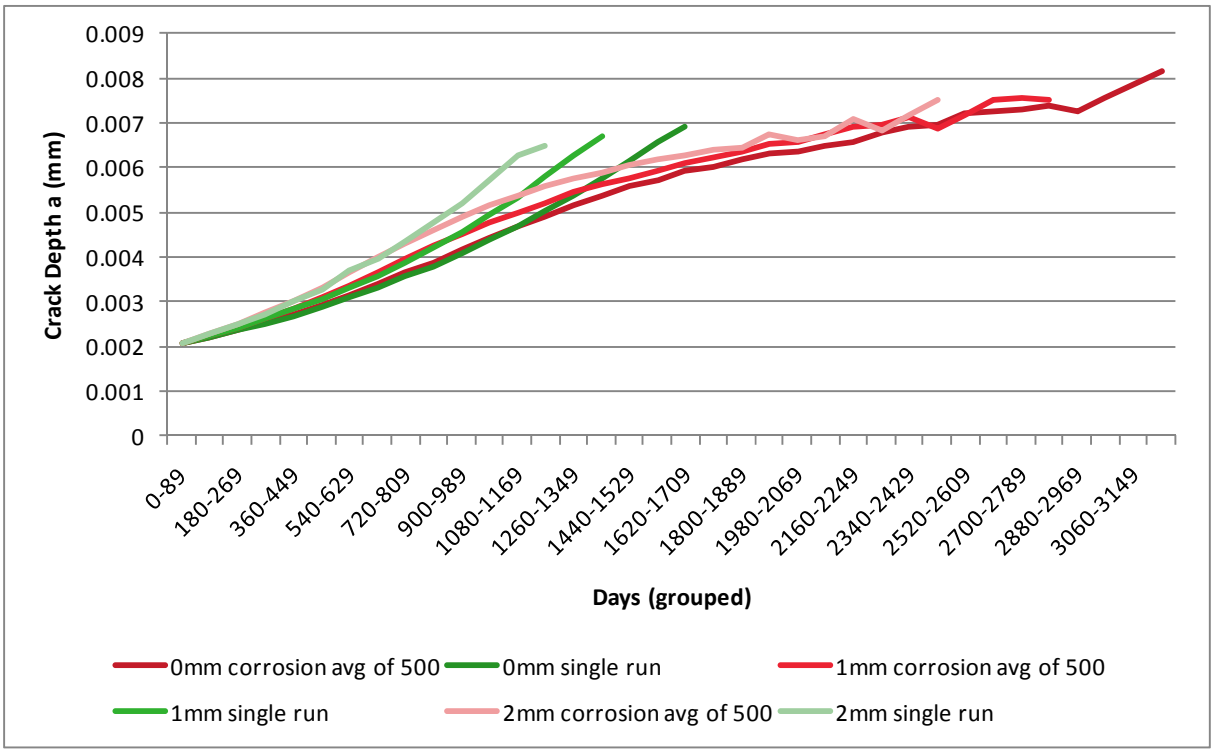

Figure 4-11 - Crack growth for randomised and unrandomised model runs with varying levels of corrosion

Figure 4-11 again shows that the single run data deviates from the full randomised set at medium time scales. It also shows that at higher corrosion levels the rate of crack growth, final crack length and time until the rail breaks all match the previous results.

Scattering effects of the randomisation can be seen at very high timescales, this is partially due to the fewer results in the data set at these time as only the most long lived runs achieve this number of days.

4.6 Conclusions

In the work detailed above, the effects of corrosion on the foot of the rail has been analysed using the Minimum Action model. To fully realise this three corrosion levels were modelled and results reported using unrandomised single model run data to provide exact figures. Additionally, a larger randomised variable run is detailed to show the validity of the single run data. The following points are reported:

- Corrosion of even 0.5mm all around the foot has a significant influence on the lifetime before failure
- Increasing levels of corrosion show more severe reduction in rail lifetime, up to 30% in some instances
- 60E2 profile shows more resistance to these effects, due to the increased cross sectional area
- Comparisons between the single unrandomised and large scale randomised test runs were detailed and showed good correlation between the result sets at low timescales
- At high timescales some deviations between the methods were shown, highlighting the variability in real life testing. However the relationship with corrosion was still noted as significant.
- The Minimum Action model can be utilised to assist in planning inspection routines or remedial action required following the detection of a defect

5. TASK 4.1.4 - MECHANICAL TESTING OF TRACK COMPONENTS (USFD)

5.1 Introduction

The work reported in SustRail deliverable D2.5[10] concluded that it was important to improve the performance of insulated rail joints (IBJ). A series of physical tests and numerical modelling work has been undertaken at the University of Sheffield to investigate a series of parameters that were thought to be significant in the performance of these joints.

A typical insulated joint is shown in Figure 5-1. Failures can be electrical or mechanical. Electrical failures occur when the insulation is breached or when there is excessive plastic deformation of the running rail (sufficient to extend across the gap filled by the endpost). Mechanical failures can occur when bolts come loose or when a fishplate breaks. Joints are typically less stiff than plain rail so the passage of rail vehicles is associated with dynamic forces; additionally, wheel impacts occur as they traverse the endpost.

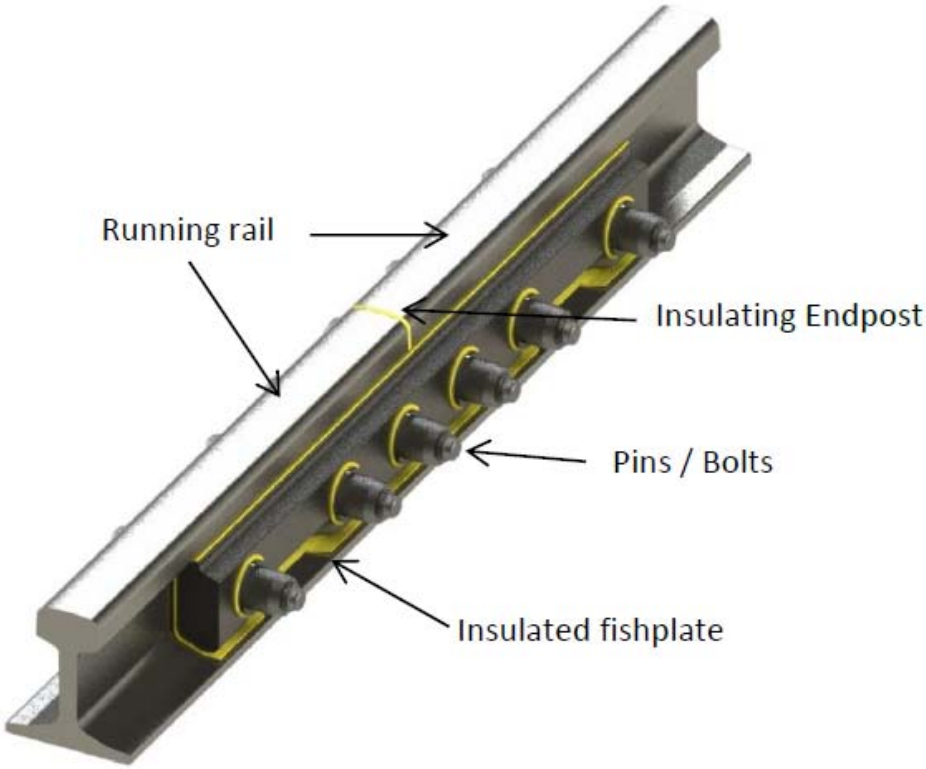

Figure 5-1: A typical insulated joint

5.2 Testing

The work reported in this section was undertaken by Phil Beaty as part of his MSc project "Experimental Testing Procedures to Investigate and Improve Insulated Block Joint Design and Life Cycle" at the University of Sheffield, 2014. His help and that of his sponsoring company, LB Foster, is gratefully acknowledged.

[10] "D2.5: Holistic approach to the vehicle-track system", SustRail consortium, 2012

5.2.1 Lipping

To investigate lipping (plastic flow of rail steel across the end-post) slots were introduced into one of the discs in the Sheffield University ROlling and Sliding (SUROS) twin disc test machine shown in Figure 5-2. This machine simulates rail-wheel contact by pressing disks of appropriate materials together, each rotated by an independent motor.

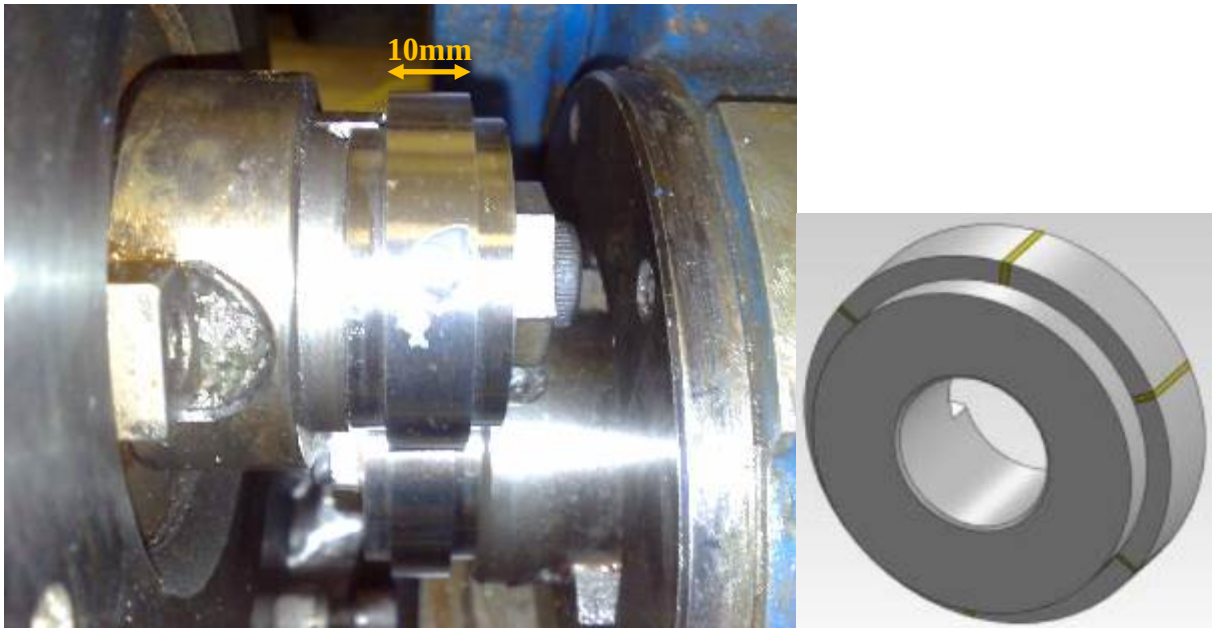

Figure 5-2: Typical test pieces in SUROS machine and rail disc with endpost inserts

For these tests the disks were 47mm in diameter, had a contact width of 10mm, and were pressed together to produce a maximum contact pressure of 1.5GPa (a typical value for wheel-rail contact of heavily loaded freight vehicles). The rig was run at 400rpm (corresponding to about 2mph, appropriate for a joint near a loop) with a slip of 0.5% (appropriate for a driven wheel). A range of 3mm-deep slot-widths (0.5, 0.75 and 1mm) were considered and these were filled with either an Epoxy-glass composite material, used mostly in glued IBJs, or a polyamide (PA6) used more commonly in non-glued IBJs. The effect of different rail steels was also considered, R260, R350, and R260 laser-clad with a hard surface.

It was found that the test method was able to assess different combinations of rail steels and endpost materials and that (in these tests which didn't include the effect of impacts):

- width of slot had a small effect on the rate of lipping, so it is predicted that across larger gaps it would take longer for the steel to bridge the gap (time approximately proportional to width)
- softer polyamide provided less resistance to lipping than the harder epoxy (surface layers wore away rapidly providing negligible benefit)
- harder steel provided more resistance to lipping (rate was approximately halved for R350 compared to R260), the laser-clad surface having a rate of lipping slightly slower than that for R350

5.2.2 Glues and liners

Two types of tests were undertaken to assess the performance of different glues and liners. The first, small-scale tests used the set-up shown in Figure 5-3. Four types of glue were assessed, Huntsman araldite adhesive, Temperange II, Edilon Dex-L 2k tix, and Permabond; these are all two-part epoxy systems made from a resin and a hardener that were developed by

the respective manufacturers for use in IBJ's. These were combined with either: a pultruded glass reinforced polyester resin liner (a stiff liner material), a glass fibre sheet (flexible woven mat), a Kevlar sheet (flexible woven mat), or no liner. These liners are used in various IBJ around the world; no installations without a liner have been identified.

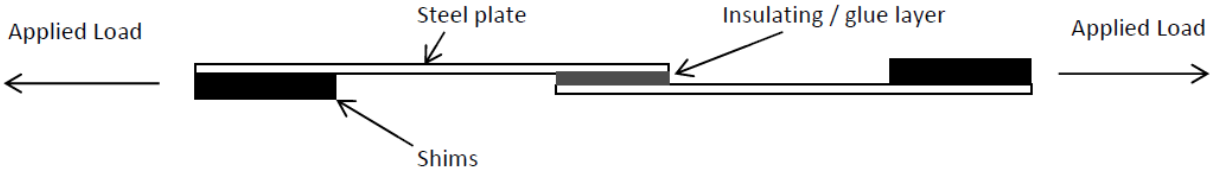

Figure 5-3: Small-scale glue and liner shear tests

It was found that:

- for all adhesives, the presence of a liner reduced the shear strength of the joint, with the Huntsman and Permabond adhesives supporting at least twice as much load when there was no liner than when a liner was present, possibly because there were twice as many interfaces to fail
- the Temperange II adhesive supported higher shear stresses with all (or no) liners
- the pultruded glass reinforced polyester resin liner supported only about two thirds of the applied force of the other liners (tested with Huntsman adhesive only)

The second tests of glues and liners used sections cut from assembled joints. These sections were tested in the test set-up shown in Figure 5-4. Load was applied at a rate of 100kN/minute until the ultimate shear strength of the glue/liner combination was reached.

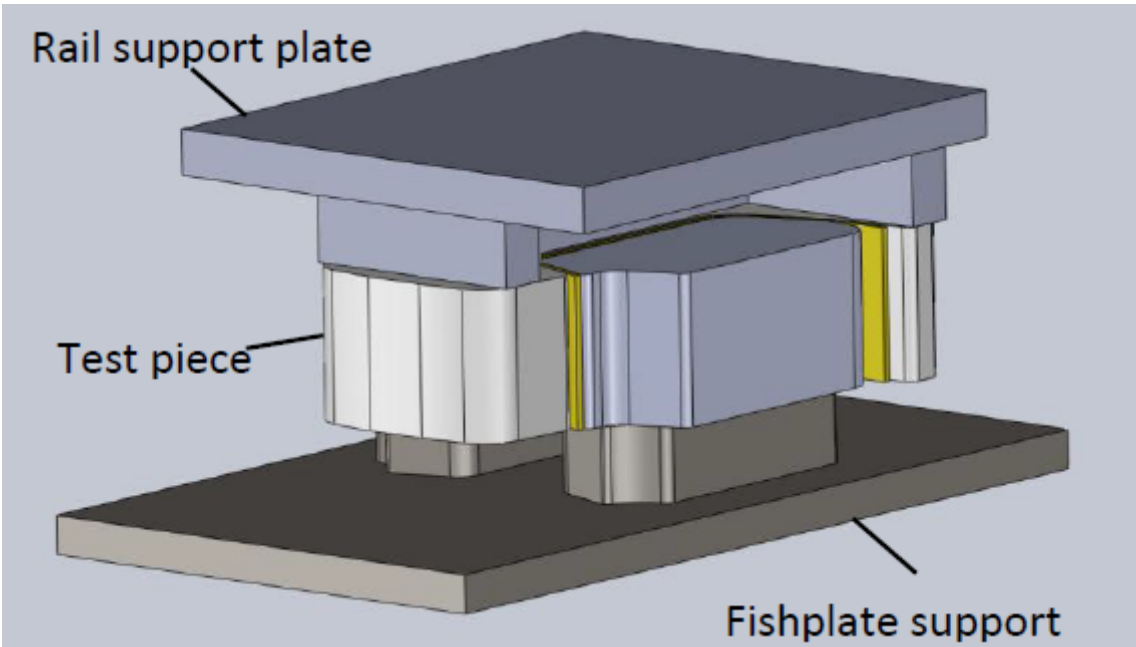

Figure 5-4: Shear test of joint section

Five different joint types were tested (four specimens of each). Two designs were used: standard (wedge-fit) fishplates, not fitted to the web, and 'full fit' joints, with a more uniform glue thickness. Three 'full fit' joints with Kevlar liners had different fastening torques applied to assess the effect of different glue thickness (it had been expected that higher torques would produce thinner layers). The fourth 'full fit' joint had a pultruded glass fibre liner while the standard joint had a glass fibre mat.

In these tests it was found that:

- increased torque hadn't decreased the glue thickness so the observed similarity of the results of the torque tests was expected
- the glass-fibre liner survived a higher shear stress than the Kevlar one
- the wedge-fit and full-fit joints had survived similar shear stresses

5.2.3 Full scale tests

Two designs of IBJ were tested in the four-point bending rig shown in Figure 5-5. Both designs survived half a million cycles of 67kNm (the maximum qualification test requirement, that from Australia), and both failed before 250 thousand cycles of 101kNm (representing extreme dynamic train loading on track). The failed specimens are shown in Figure 5-6 (standard) and Figure 5-7 (modified).

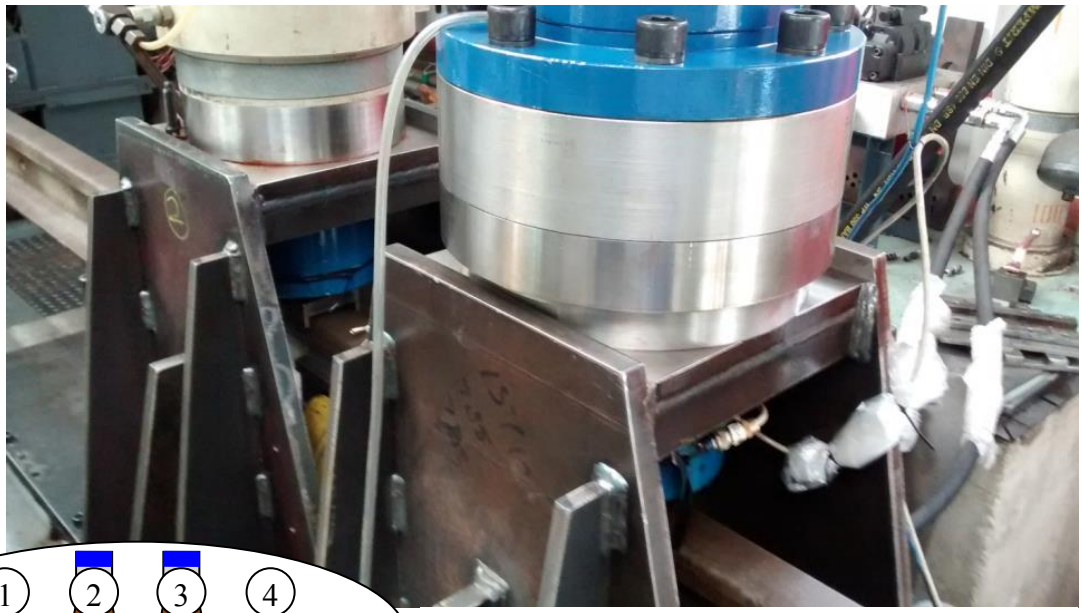

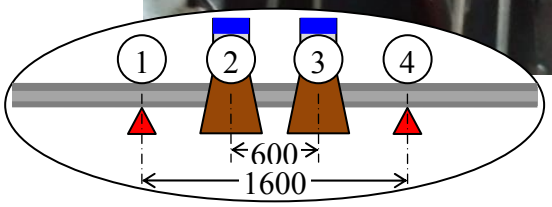

Four point bend: rail is supported at points 1 & 4; actuators 2 & 3 provide equal force. Section of rail between 2 & 3 experiences constant bending.

Figure 5-5: Four-point bending rig

Figure 5-6: Standard rail joint failure

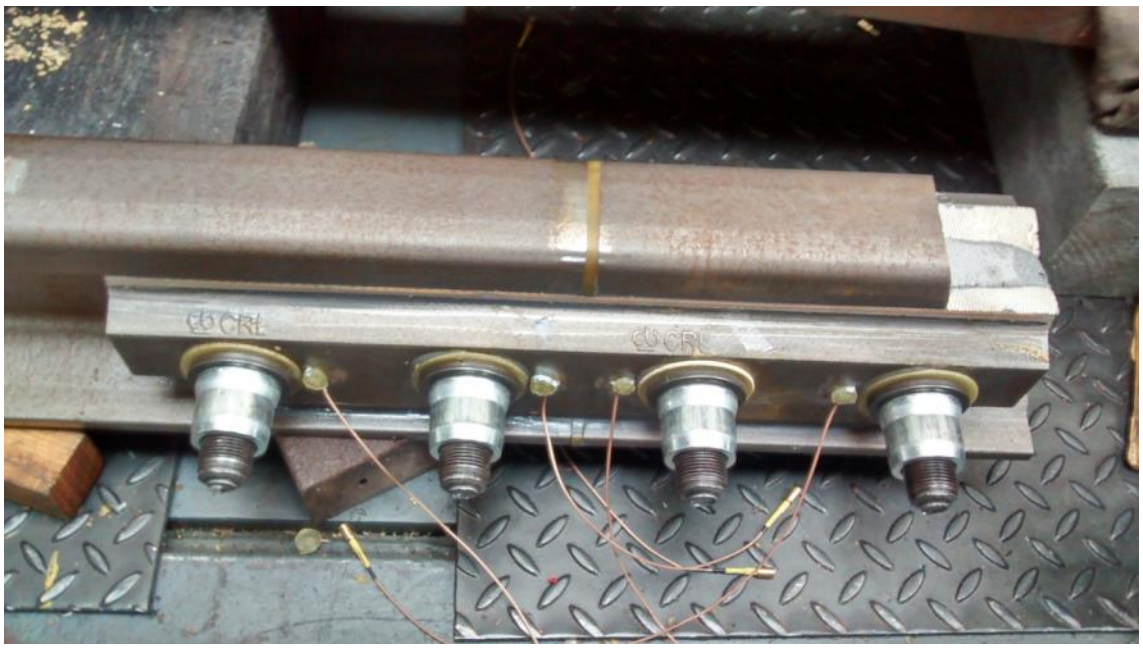

Figure 5-7: Modified rail joint failure

The standard design failed by fracture of the fishplates, whereas the modified design remained intact with failure occurring in the rail adjacent to the joint. These results suggest that

- the modified design is better than the standard one
- it should be ensured that the foot of the rail adjacent to IBJ has no defects that could initiate fatigue cracks
- there is scope to improve the design to remove the stress concentration at the end of the fishplate (see also finite element results in Figure 5-12)

5.3 Finite element modelling

Finite element models of the rail joints were established using geometry defined in Network Rail's drawing RE/PW/268 D, "BS113A BR Mk III Glued Insulated Joint 4 & 6 Hole Type". The model was created in ANSYS and used mainly 8-noded hexahedral elements; a small

volume around the spherical-ended cut-out for rail clips was meshed with tetrahedral elements and the bolts, apart from the heads, were cylindrical beam elements. Due to symmetry only a quarter of the joint needs to be modelled.

The model is shown in Figure 5-8 (note that the elements' mid-side nodes lie on relevant circular arcs, but this plot shows straight facets). The elements of the liner (LINER), bushes around bolts (BUSHE, these elements are not visible in Figure 5-8 as they are inside the joint), insulating washers (WASHE), and endpost (ENDPOST) were assigned elastic material properties of epoxy[11] (E=45GPa, ν=0.19), with all other elements being steel (E=207GPa, ν=0.3). Relevant symmetry conditions were applied to symmetry planes and the rail was supported (fixed vertical, y-direction, displacements) at the base of the remote end (800mm from the centre).

Two load steps were used: In the first the bolt load was applied as a tension of 200kN in the bolts; in the second the bending moment was applied, a point force on the top of the rail at 300mm from the centre.

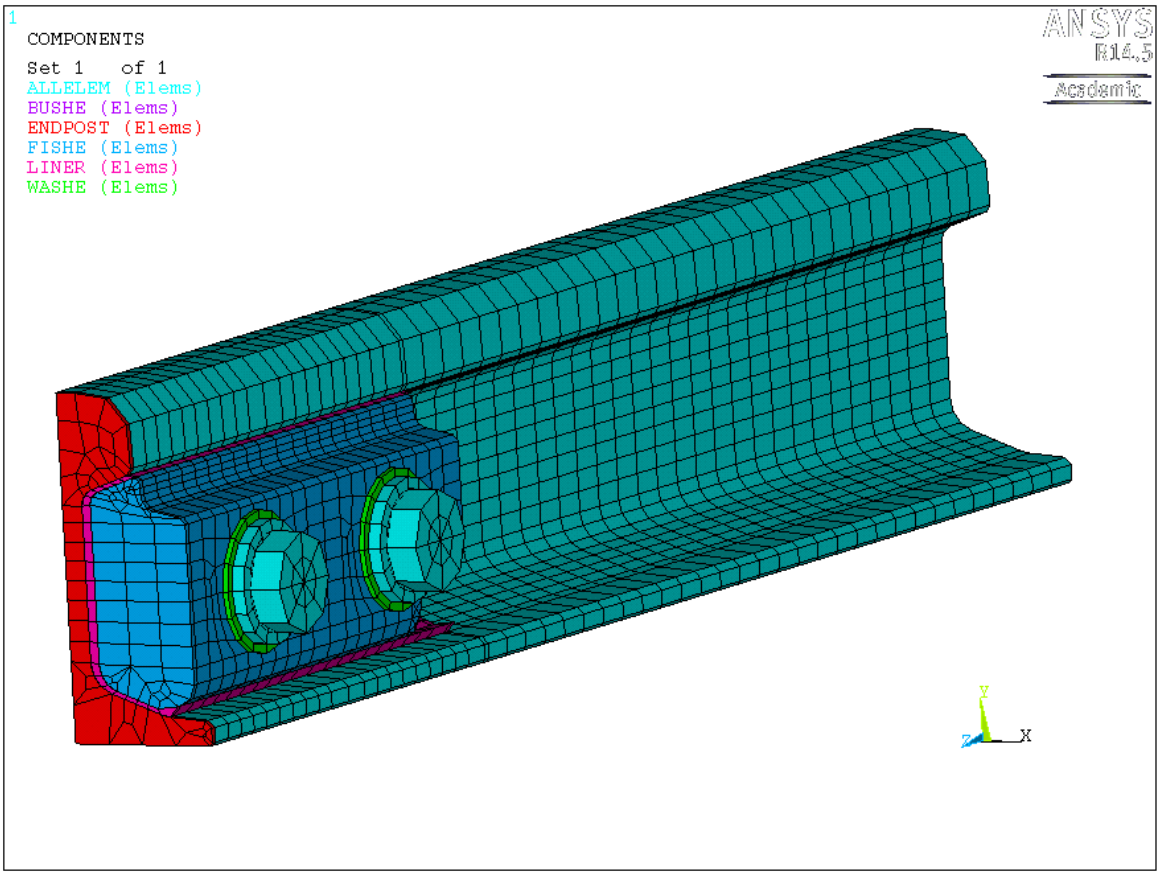

Figure 5-8: Finite element mesh of rail and IBJ

Two situations were modelled: the glue fully supporting the interface (modelled by sticking the elements together) and glue having debonded from the surfaces (modelled using contact algorithms that calculate amount of sliding).

[11] Y.-C. Chen and J. H. Kuang, Contact stress variations near the insulated rail joints, Proc IMechE Part F, vol. 216, no. 4, pp. 265–273, 2002

The results for the principal stress in the fishplate for the two cases are shown in Figure 5-9 and Figure 5-10. It can be seen that the principal stress (and hence risk of fatigue failure) reduces marginally when the glue debonds.

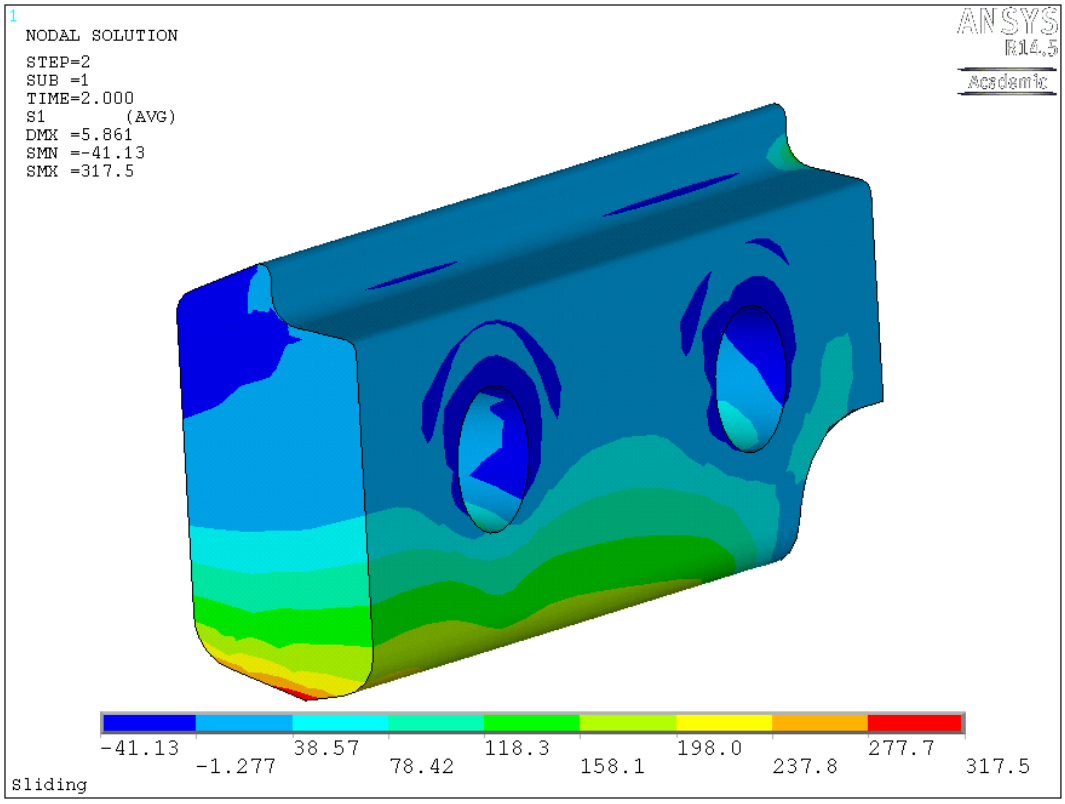

Figure 5-9: Major principal stress in fishplate for debonded glue

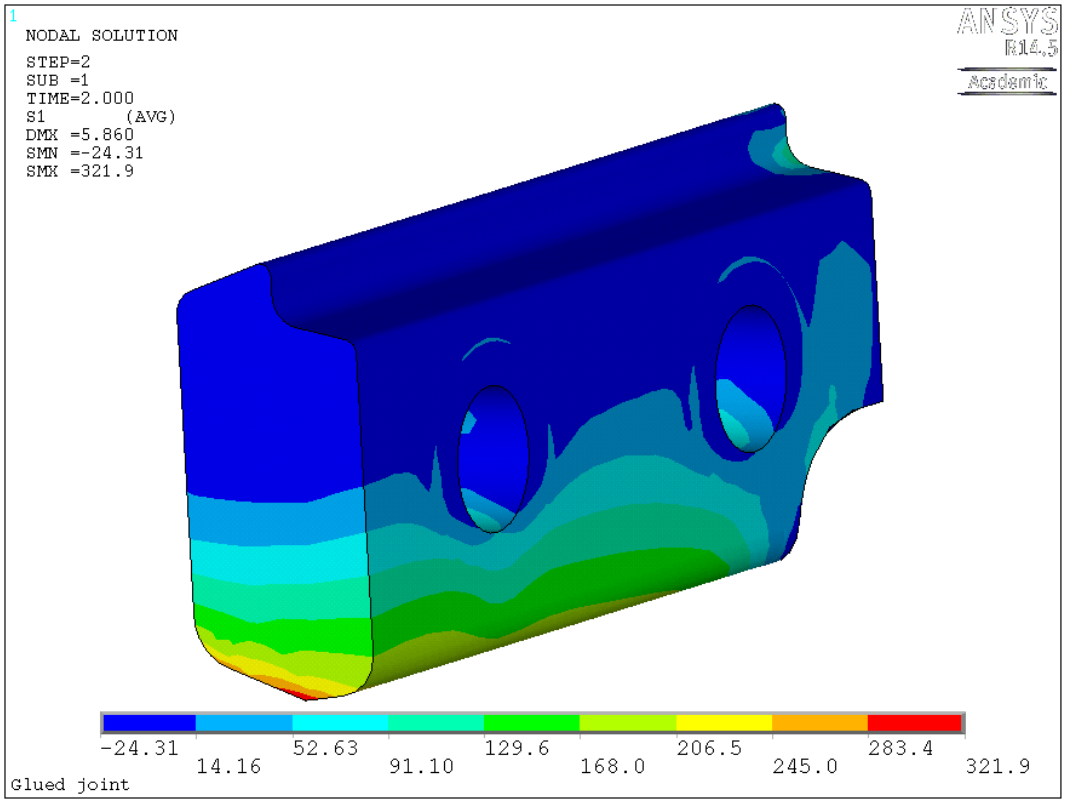

Figure 5-10: Major principal stress in stuck fishplate

The effect on the stress in the endpost is insignificant, as seen from results in Figure 5-11, the maximum tensile stress in the debonded (sliding) model drops to 235.0MPa from 235.6MPa for the glued model.

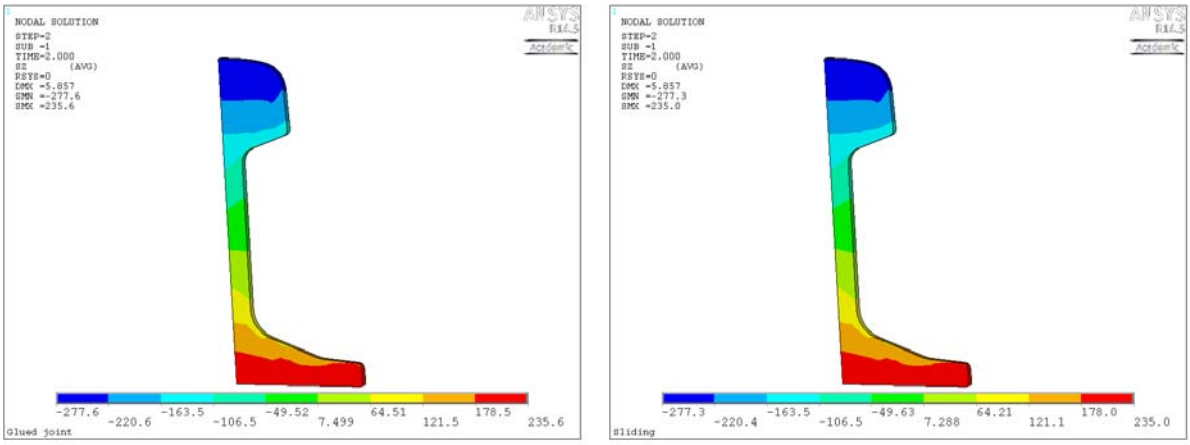

Figure 5-11: Longitudinal (z) stress in endpost

The stress in the rail is predicted to be at its maximum near the location that the crack initiated in the testing (at the foot of the rail near the end of the fishplate) so the testing supports the modelling results.

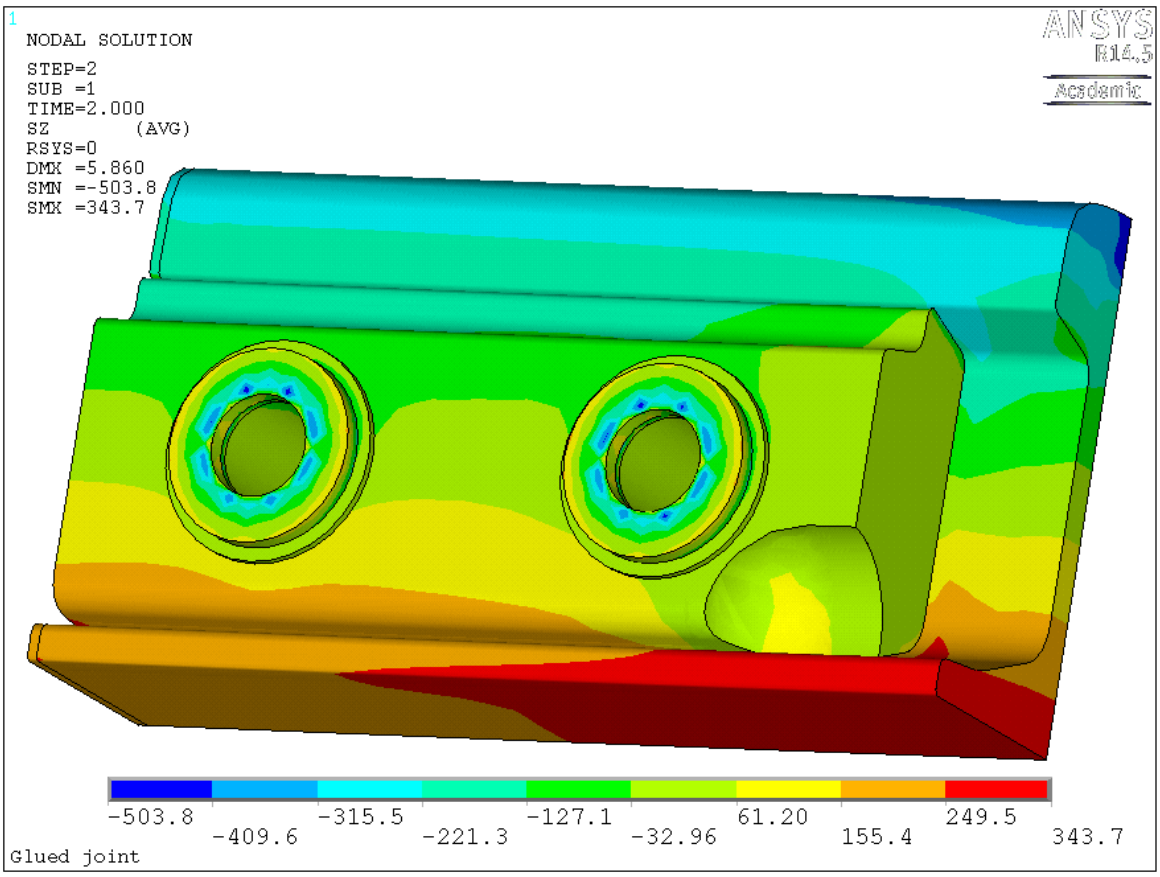

Figure 5-12: Longitudinal stress in glued joint assembly

5.4 Conclusions

A range of tests have been undertaken to investigate the effect of varying properties on the performance of rail joints. Some novel tests have been undertaken and have the potential to be

used to investigate the behaviour of different materials and geometries for insulated joints. The physical testing has been supported by finite element modelling.

It was found that the use of absorbant liners increases the shear capacity of the glued joint.

A significant finding is that it is important to check the underside of rails adjacent to joints as high stresses here can lead to failure of the rail. A redesign of the ends of fishplates could reduce the stress concentration at these locations.

It was also found that hard endpost materials are less prone to failure by lipping, and that (in these tests) the rate of lipping is not affected by the thickness of the endpost.

The finite element results suggest that the mechanical strength of joints is not adversely affected by debonding of glue in the joint, but there may be adverse electrical effects if debonding reduces the resistance of the insulation.

6. TASK 4.1.5A - RISK ANALYSIS IN THE DESIGN AND OPERATION PHASE (LTU, NR, TRAIN)

This section describes a method for risk analysis in the design and operational phase for a railway system.

6.1 Engineering analysis

An essential aspect, of sustainable railway vehicle and track system, is effective engineering analysis and assessment of the system at the different life cycle phases. The demand on present vehicle and track system requires that systematic engineering analyses of railway network at relevant level should be done to support high performing and resilient track system in the design and operation phase. Figure 6-1 shows the system breakdown structure of a railway network and the relevant analyses useful for the improvement or modification of the functional performance of the network.

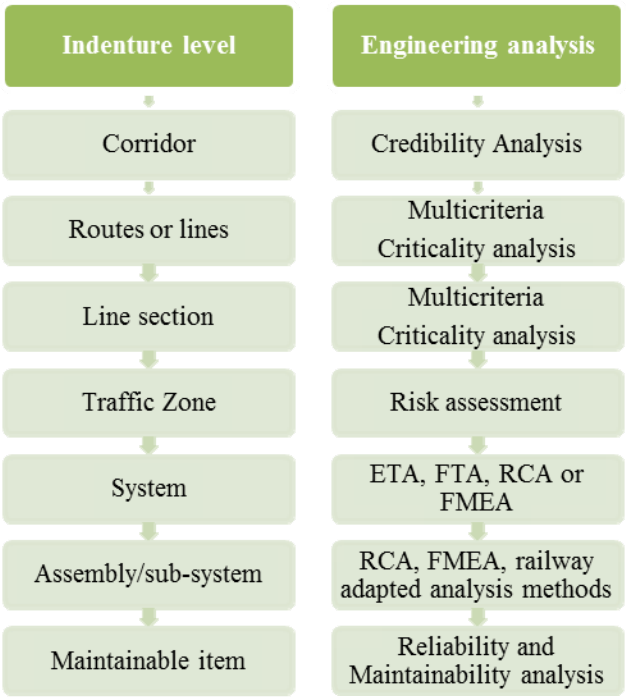

Figure 6-1: Engineering analysis for high performing track system

Risk assessment provides infrastructure manager and other stakeholders with an improved understanding of risks that could affect the achievement of overall business objectives. Risk assessment is a standardize technique that can be used to identify, analyse and evaluate risk against the expected performance or resilience of the track system. Risks can be assessed at different hierarchical levels of the infrastructure configuration besides the level shown in the figure. Even the risk of individual design action or maintenance task can be assessed. Risk assessment provides evidence-based information to make informed decisions. The information helps to understand risks, their causes, consequences and their probabilities and gives input into decisions such as:

- whether a design, operation or maintenance action should be undertaken;
- how to maximize opportunities;

- whether risks need to be treated;
- choosing between options with different risks;
- prioritizing risk treatment options;
- the most appropriate selection of risk treatment strategies that will bring adverse risks to a tolerable level.

Detailed procedure for risk identification, analysis and evaluation is described in IEC 31010 standard[12]. Risks analysis methods can be qualitative, semi-quantitative or quantitative. The choice of the method to be used will depend upon the specific application, the availability of reliable data and the need or purpose of the procedure.

a. Qualitative method expresses consequence, probability and level of risk using qualitative terms such as "high", "medium" and "low", which can be regarded as significance levels. In this method the aggregation of consequence and probability is done and the resultant level of risk is evaluated against qualitative criteria.
b. Semi-quantitative methods adopt numerical scales to grade consequence and probability and then combine them to produce a level of risk using a formula. The scales used may be linear or logarithmic or have some other relationship, depending on the application.
c. Quantitative method estimates practical values for consequences and their probabilities, and produces values of the level of risk.

Full quantitative analysis would be most reliable but may not always possible due to insufficient information about the system, lack of data, questionable aggregation technique or because the effort is not considered warranted. Therefore, semi-quantitative method or combination of semi-quantitative and qualitative ranking of risks by specialists, are considered practical and effective.

6.2 Risk matrix

Risk matrix is a frequency - consequence visualisation and evaluation tool used for the classification of events into risk categories to facilitate improvement decisions in terms of risk reduction or elimination. Basically, risk matrix gives the opportunity to combine qualitative ratings and quantitative estimates (even semi-quantitative ratings) of consequence and probability to produce risk rating. The design of the matrix depends on the context and circumstances in which it is used. In the description shown in Figure 2, quantitative estimates of failure frequency are aggregated with quantitative estimates of failure consequence using a risk matrix. The output of the risk analysis is risk level or category in qualitative terms such as intolerable, undesirable, tolerable negligible categories.

Figure 6-2: Risk matrix design using quantitative and qualitative approach

[12] IEC 31010 (2009). Risk management – Risk assessment techniques. International Organization for Standardization/ International Electrotechnical Commission, ISO.IEC 31010:2009.

In the case study, the frequency of occurrence of traffic interrupting failures is taken to be the first indicator in the risk matrix and operational consequence in terms of train delay is the second indicator. The qualitative categories of failure frequency and severity levels of the consequences typical for a railway system have been adapted from RAMS standard[13]. A typical risk matrix useful for performance improvement at the design and operation phase of track life cycle is presented in Figure 2. The numerical scaling shown in the Figure 2 is defined such that it reflects the acceptance limit and quality expectations of the infrastructure owner.

Frequency	Likely impact or consequence of failure			
	Insignificant	Marginal	Critical	Catastrophic
Frequent	Undesirable	Intolerable	Intolerable	Intolerable
Probable	Undesirable	Intolerable	Intolerable	Intolerable
Occasional	Tolerable	Undesirable	Undesirable	Intolerable
Remote	Negligible	Tolerable	Undesirable	Intolerable
Improbable	Negligible	Negligible	Tolerable	Tolerable

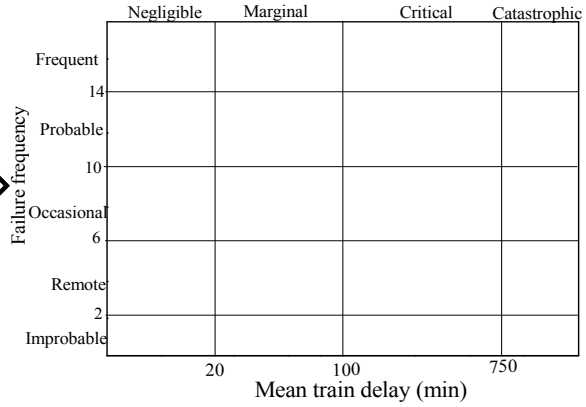

Figure 6-3: Typical risk evaluation matrix

6.3 Case study

A case study is hereby presented to demonstrate the use of risk matrix for risk analysis. A line section on the Swedish Transport Administration (Trafikverket) network is considered in the case study. The line section is a 168 km single track section on the heavy haul line commonly referred to as “Malmbanan”. The data used in the analysis are collected between 2010 and 2013 but for simplicity, only the data for the year 2011 is presented in this report. There are 171 records of infrastructure failure that interrupted traffic and resulted into operational delay consequence. The total delay (i.e. after five minutes of planned arrival time) as a result of infrastructure failure is 21550 min from approximately 1800 passengers and freight trains.

Train delays caused by infrastructure failure contributed approximately 15% of the total delay in 2011. Figure 6-4 shows the assemblies that are critical considering failure frequency and delay consequence separately. As it can be seen, track and switches & crossings (S&Cs) contribute the most to the number of traffic interfering failures on the line section. From the perspective of delay consequence, track, alternative power line, S&Cs, interlocking and catenary are critical failure modes for train operation.
Furthermore, because railway infrastructure is linearly distributed it is essential to divide the 168 km line into smaller zones for detailed study, performance assessment and improvement. This will facilitate the identification of critical zones that are bottlenecks to the achievement of targeted functional performance of the line section. The line section is divided into 37

[13] EN 50126 (1999). Railway applications. The specification and demonstration of reliability, availability, maintainability and safety (RAMS). Basic requirements and generic process. British Standards Institution, BS EN 50126-1:1999.

zones that are the traffic zones used by the Swedish Transport Administration for train operations management.

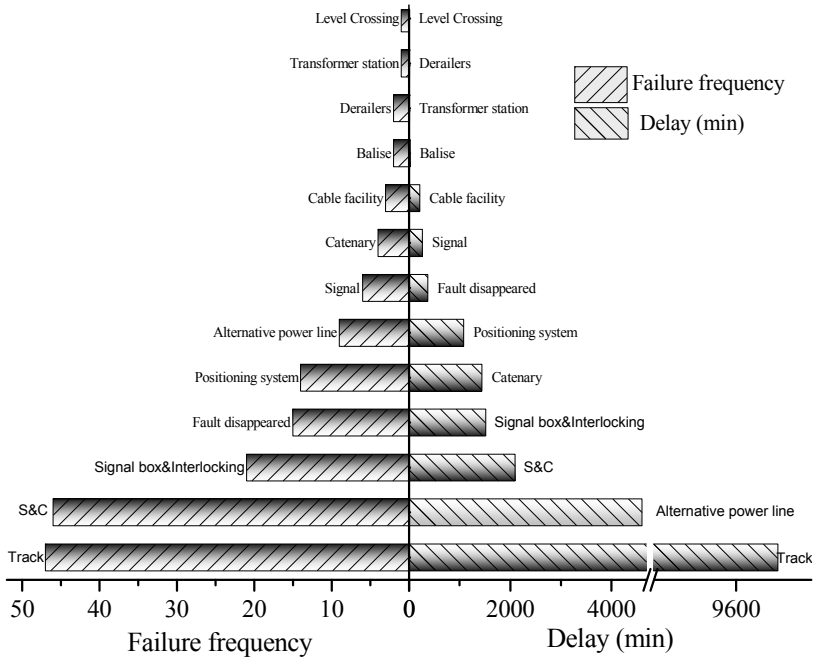

Figure 6-4: Critical failure modes based on failure frequency and delay consequence

Figure 6-5 shows the weakest links in the chain based on failure frequency and delay separately. The weakest links with respect to failure frequency are 8, 7 and 13 whereas 6–7, 12–13 and 2–3 are the weakest link with respect to operational consequence. This information is useful in identifying critical locations contributing to poor performance of the systems on the line. The quantification of the integrity of the zones is however different when the two indicators are used separately, as shown in Figure 6-5. Therefore the performance indicators must be aggregated in an index or visual representation to facilitate effective decision making.

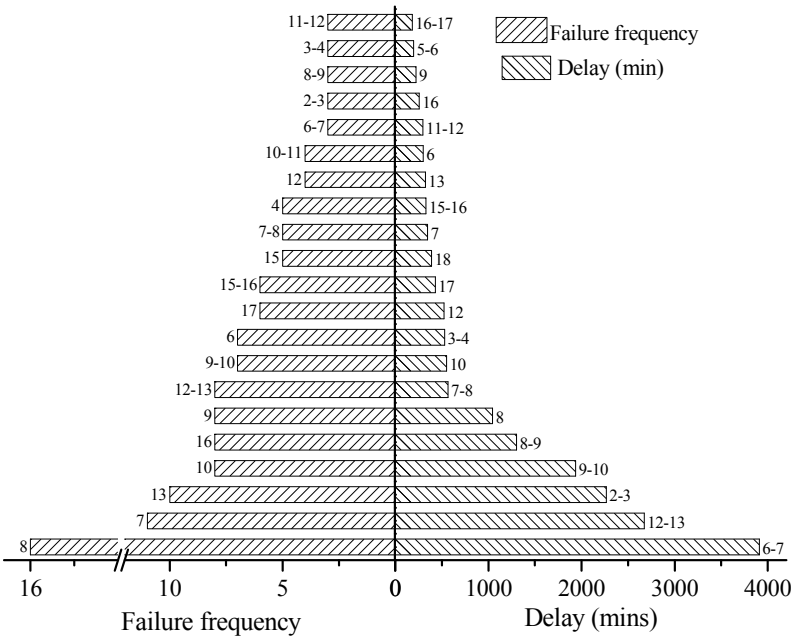

Figure 6-5: Weakest links (i.e. traffic zones) on the line

The risk matrix tool is employed for visualising the two indicators in an aggregated view. **Error! Reference source not found.** shows the categorisation of the traffic zones based on the risk of limiting the achievement of targeted performance requirements. Zones 8, 7, 2–3 and 6–7 fall within intolerable risk category, zones 13, 9, 16, 6, 10, 9–10, 12–13, 7–8, 3–4, 8–9, 12 are in the undesirable category, zones 15, 17, 15–16 and 10–11 belong to the tolerable risk category and zone 4 falls within the negligible impact category. All other zones are not categorised because they have less than three failure records, which makes the estimation of their lognormal mean delay impossible. These categorisations can be taken as risk priorities to support decision on mitigation options. To meet targeted performance requirements of the line, the traffic zones in the intolerable and undesirable risk categories must be subjected to detailed failure analysis so that they are controlled to a level that is tolerable.

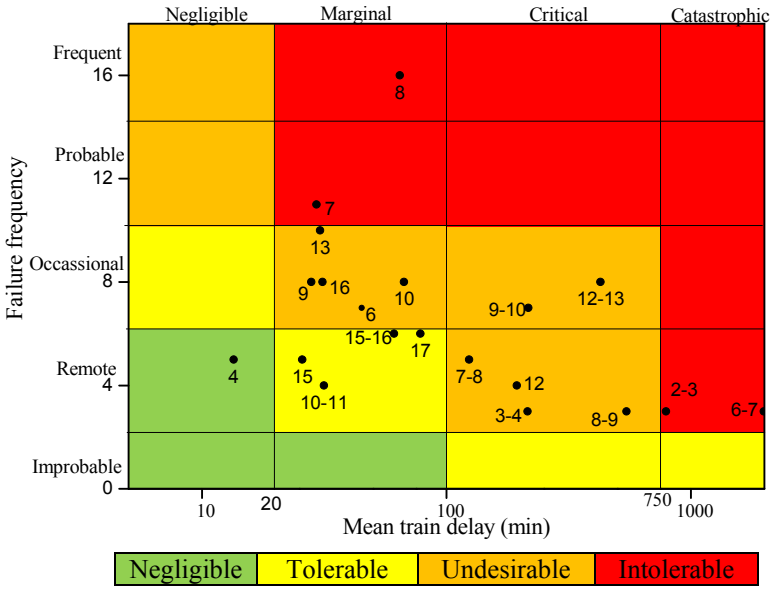

Figure 6-6: Categorisation of zones based on the risk of target performance requirements

6.4 Concluding remarks

- Risk matrix tool provides a visual presentation and categorisation of systems (higher and lower level system) and component into different risk group to enhance intervention for RAMS assurance.
- The result shows the traffic zones which are weakest link on the route investigated. Further analysis can be done on the items and subsystems in the line sections to rank them for improvement purpose.
- In case where economic and safety consequence are required (besides operation consequence), the second axis in the matrix can be changed to a combine all in cost term.
- The extended implication of this study is the applicability of risk matrix principle in the design phase of track and track components to assure a high performing track. Common challenge is the non-availability of data needed for the analysis at the design phase. Nonetheless, the following techniques are suitable for estimation of the failure frequency and consequence of the system: similarity analysis (for existing system or change in design parameters), stress analysis (for new operating conditions), simulation modelling or expert judgment (for new design) and etc.

7. TASK 4.1.5B - FROM SAFETY LIMITS TO MAINTENANCE LIMITS (LTU, NR, TRAIN)

This section describes a method for cost-effective maintenance of railway track geometry with the aim of moving the maintenance decision making from an approach based on safety limits to a process based on maintenance limits.

7.1 Research purpose and objectives

The purpose of the study is to propose a decision support tool to optimise track geometry maintenance by identifying cost-effective maintenance limits. The objectives are:

- To analyse track geometry degradation and its influencing parameters;
- To evaluate the effectiveness of the present track geometry maintenance strategy of Trafikverket (Swedish Transport Administration);
- To increase knowledge about geometrical degradation process in turnouts.
- To develop a cost models to specify a cost-effective inspection interval and maintenance limits.

7.2 Track geometry degradation and its influencing parameters

The degradation of track geometry is a complex phenomenon occurring under the influence of dynamic loads and is normally calculated as a function of traffic in mm/MGT, or time in mm/year (Esveld, 2001). Some factors which can affect the track geometry degradation are shown in the Ishikawa diagram in Figure 7-1. These factors are classified as design, construction, operation, and maintenance.

For a track section with similar traffic, the rate of degradation varies depending on construction and differences in substructure. Figure 7-2 shows the variability of longitudinal level degradation rate in different 200 m tangent segments of the studied track for the time interval 2007–2009. The figure clearly shows the high variability of degradation rates for the track with the majority of the sections having low degradation rates that can be controlled by preventive tamping at infrequent intervals. However, the tail of the distribution consists of sections with high degradation rates that need to be accurately monitored and restored with corrective tamping to reduce risks. The balance between preventive and corrective tamping must be based on an appropriate cost analysis, as suggested in this study.

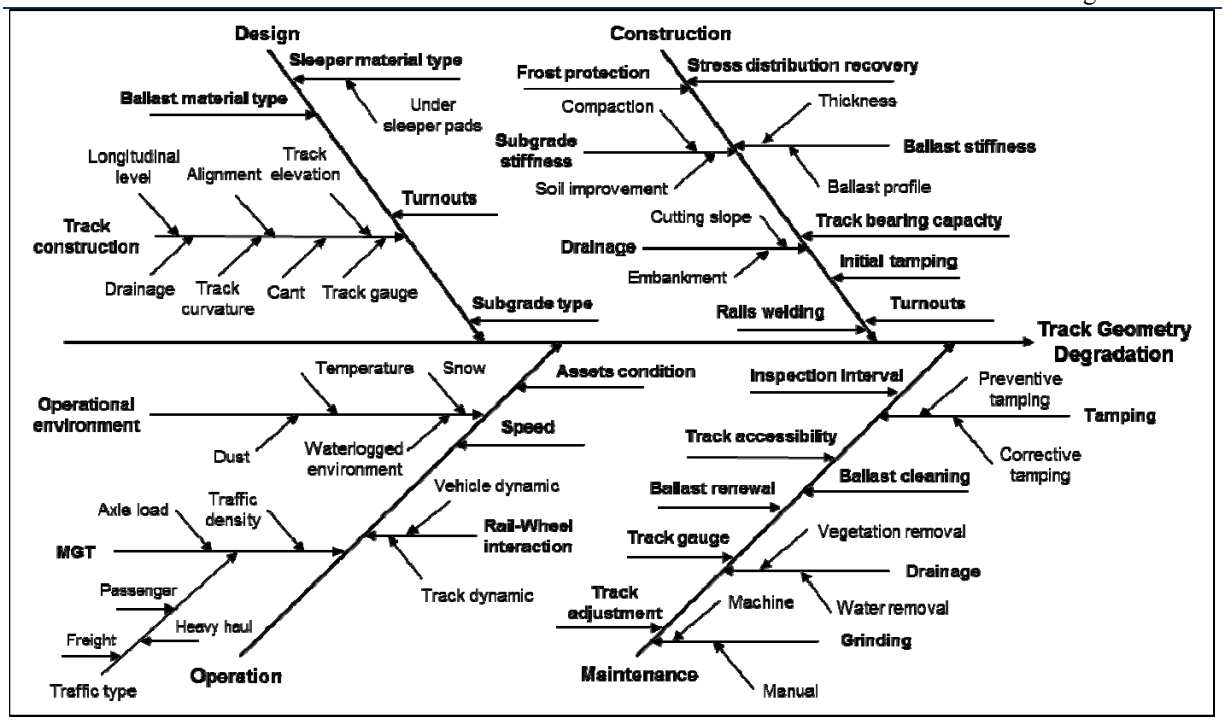

Figure 7-1 Ishikawa diagram (cause and effect diagram) of the factors influencing track geometry degradation.

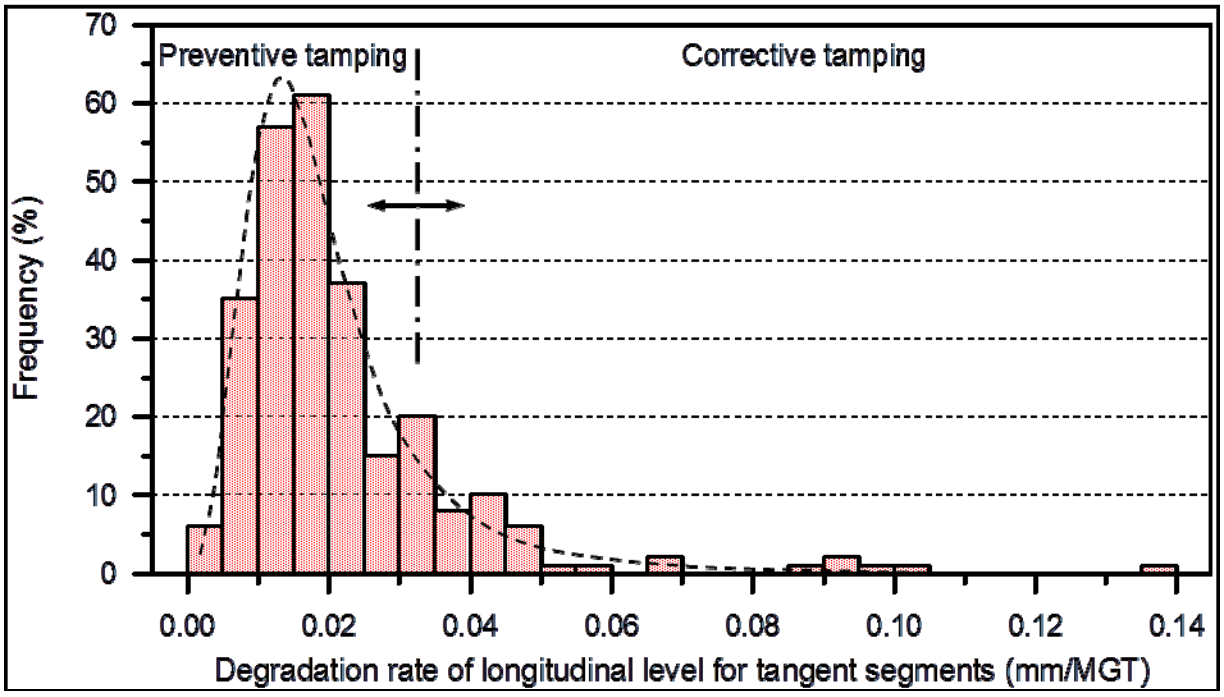

Figure 7-2 Histogram of longitudinal level degradation rates in tangent segments between 2007 and 2009.

The geometry data was collected from the iron ore line (Malmbanan) in northern Sweden, used by both passenger and freight trains, to find the probability distribution of geometry faults. The probability distribution analysis was based on the number of detected segments with geometry faults over the time interval between two consecutive inspections. No difference was considered between the occurrence of a single point fault and multiple point

faults on the same segment in the same time interval because maintenance should be carried out on the segment regardless of the number of detected geometry faults.

Since the exact times of fault occurrences were not known, the fault time data are considered interval-censored, whereby the object of interest was not constantly monitored. Thus, the inspection times in terms of MGT were used as interval ranges for fault times. The segments without any fault occurrences over the studied time period were also considered right-censored data. The linear regression technique was used to rank probability distributions, with goodness of fit illustrated by the correlation coefficient parameter (ρ).

The probability distribution analysis, performed using Weibull++7 software, shows that for B-faults, the lognormal distribution is the best fitted distribution at ρ=0.9889. The Weibull distribution provides the best fit for C-faults and safety faults data sets. Since the Weibull distribution is a flexible distribution which can be used to model many types of failure rate behaviour (Rausand and Høyland, 2004) and because the difference between ρ values obtained from the Weibull distribution and the lognormal distribution is very small, the Weibull distribution is also used to estimate the probability of B-faults (see Figure 7-3). The parameter values of the Weibull distribution and the value of the correlation coefficient (ρ) of each distribution for B-faults, C-faults and twist (3 m and 6 m) are shown in Table 1.

Table 1 The characteristics of pdf of B-failures, C-failures and twist (3 m and 6 m)

Type of failures	Type of distribution	Values of distribution parameters		ρ
		Shape (β)	Scale (η)	
pdf of B-failures	Weibull 2parameters	1.606	31.99	0.968
pdf of C-failures	Weibull 2parameters	1.379	116.114	0.986
pdf of twist (3 m & 6 m)	Weibull 2parameters	1.857	329.771	0.971

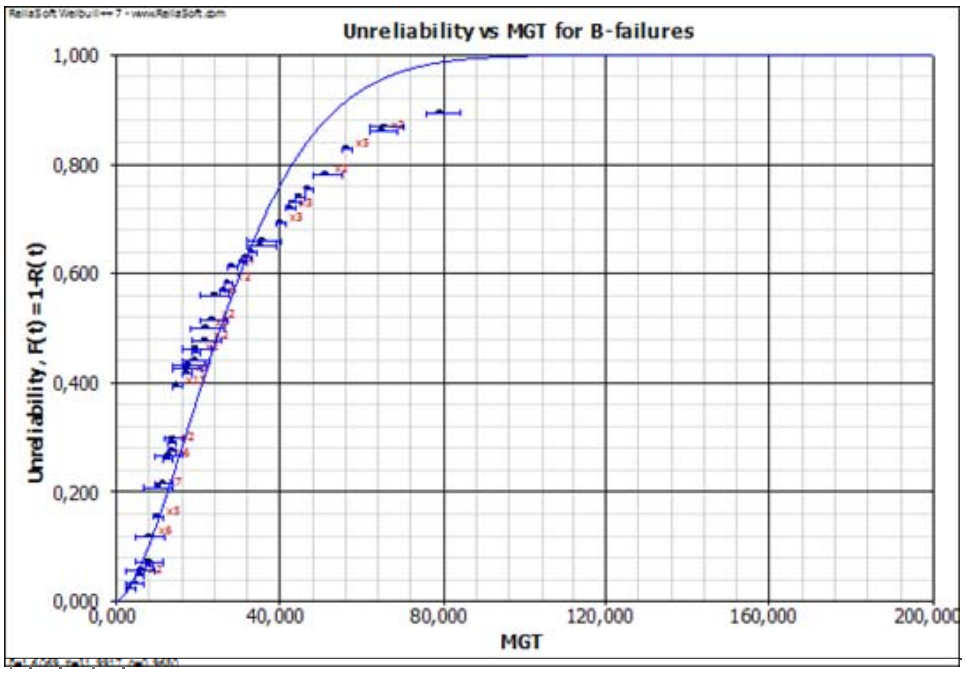
Unreliability vs MGT for B-failures
Unreliability, F(t) = 1-R(t)
1,000
0,800
0,600
0,400
0,200
0,000
0,000
40,000
80,000
120,000
160,000
200,000
MGT

(a)

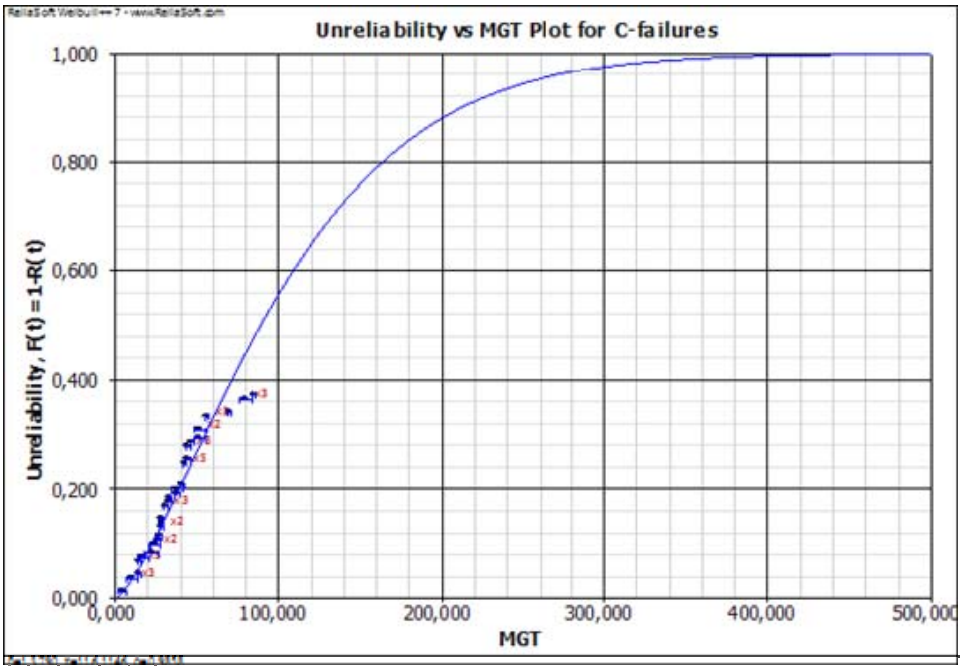
Unreliability vs MGT Plot for C-failures
Unreliability, F(t) = 1-R(t)
1,000
0,800
0,600
0,400
0,200
0,000
0,000
100,000
200,000
300,000
400,000
500,000
MGT

(b)

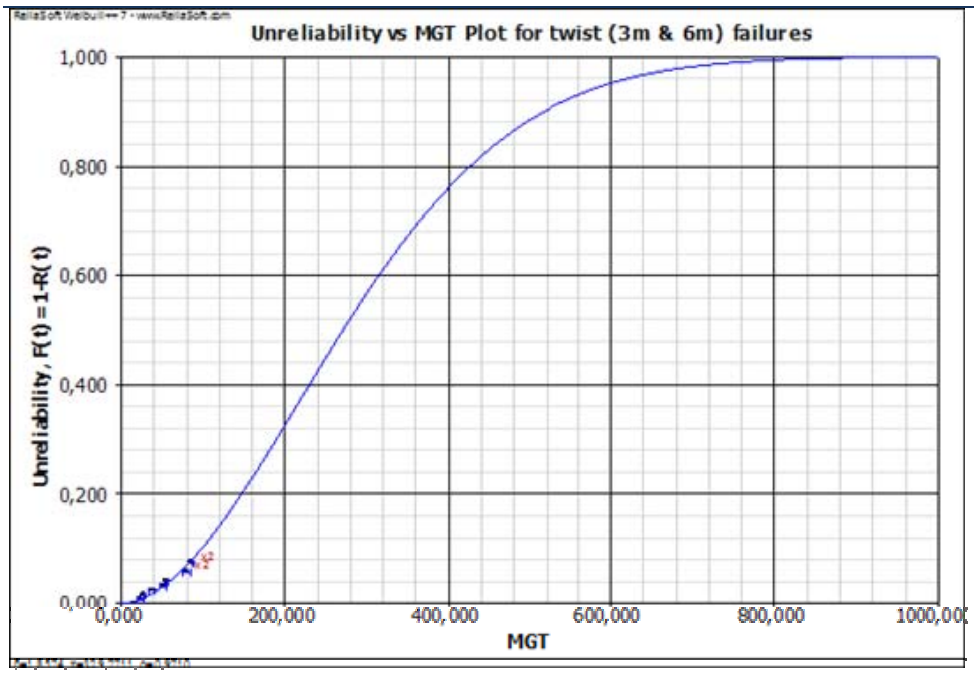

(c)

Figure 7-3 Cumulative distribution functions of geometry faults versus MGT (a) B-faults, (b) C-faults and (c) twist (3 m & 6 m) failures.

7.3 Analysis of geometrical degradation process in turnouts (Crossing location)

Turnouts are critical components of railway track systems in terms of safety, operation and maintenance. Each year, a considerable part of the maintenance budget is spent on their inspection, maintenance and renewal. Applying a cost-effective maintenance strategy helps to achieve the best performance at the lowest possible cost. In Sweden, the geometry of turnouts is inspected at pre-defined time intervals by the STRIX / IMV 100 track measurement car. This study used time series for the measured longitudinal level of turnouts on the Iron Ore Line (Malmbanan) in northern Sweden. Various geometry parameters were defined to estimate the degradation in each measurement separately. The growth rate of the longitudinal level degradation as a function of million gross tonnes (MGT) / time was evaluated. The defined parameters are the following (Figure 7-4):

- A: the distance between the peaks after and before crossing valley;
- C: the slope of the measurement line 1 metre before the crossing point;
- D: the slope of the measurement line 1 metre after the crossing point;
- E: the longitudinal level value at the first peak before the crossing point;
- E': the difference of the longitudinal level values between the first peak before the crossing and the valley before it;
- F: the longitudinal level value at the second peak after the crossing point;
- F': the difference of the longitudinal level values between the second peak after the crossing and the valley after it;

- G: the difference of the longitudinal level values between the first peak before the crossing and the crossing valley;
- H: the difference of the longitudinal level values between the second peak after the crossing and the crossing valley.

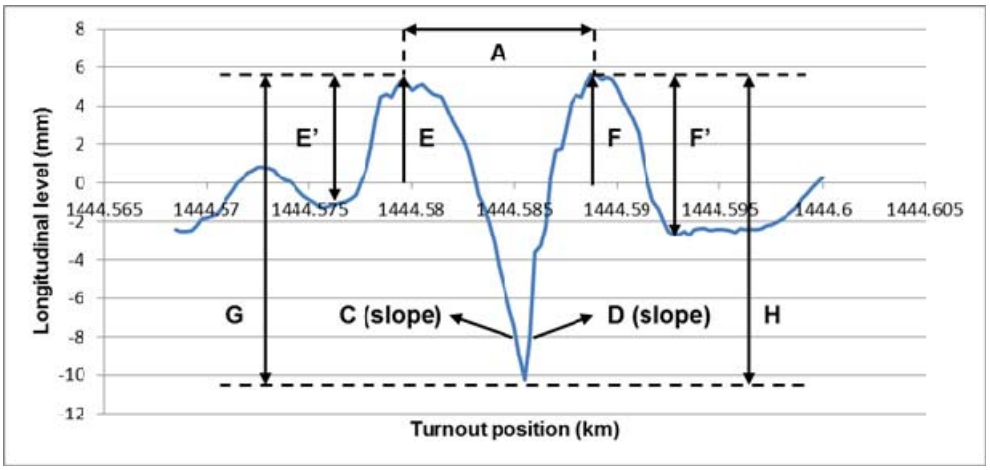

Figure 7-4 Defined geometry parameters in the second approach

The trends of the defined geometry parameters are shown in Figure 7-5. As can be seen in the figure (part (a)), parameter A in both turnouts has an increasing trend until 2011-06-29. As maintenance was carried out on Rsn 1 after 2010-06-29, the value of A for Rsn1 drops. However, after the maintenance execution, the magnitude of A again increases, reaching 9.5 m by 2011-06-29. At this point, the growing trend ends and the magnitude remain constant. Similarly, the C & D show an increasing trend in both turnouts until 2011-06-11; after this, they demonstrate a reducing trend until they ultimately become stable. This pattern shows that the crossing has continuously settled until it reaches a limit. After reaching this limit, the crossing cannot settle anymore, and the geometry fault widens. As expected, the trend for E & F is similar to that for E' & F'; the degradation grows slightly until 2011-06-11, and after this time, a sharp increase can be seen. To interpret these trends, it is necessary to consider the trends of G and H simultaneously. The G and H grow exponentially until 2011-06-11; at this point, they become constant. This indicates that the geometry fault wave at the crossing has reached its limit (about 25 mm) and the fault has transferred to the next wave in the crossing neighbourhood. This transfer can be perceived by the sharp increase in E/F & E'/ F' trends.

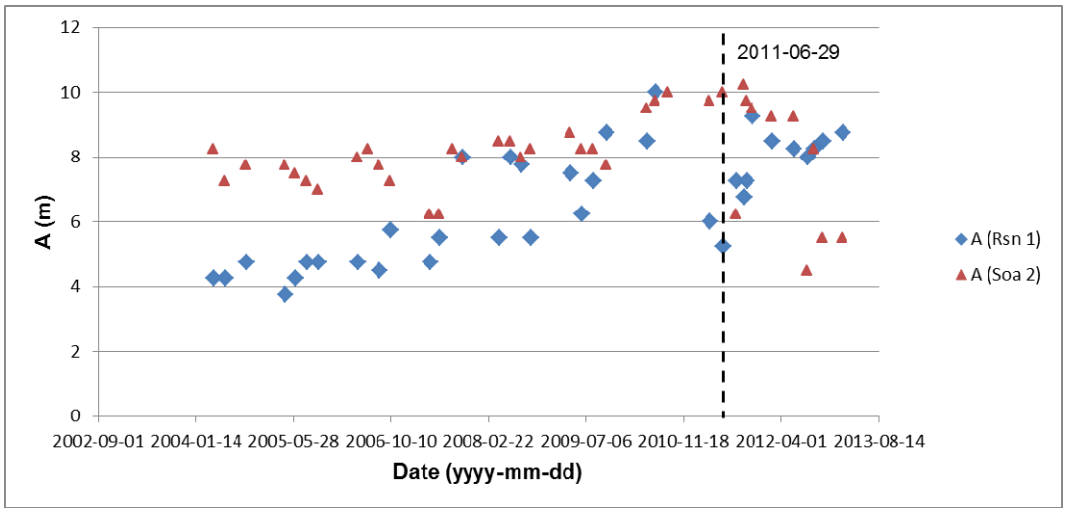

(a)

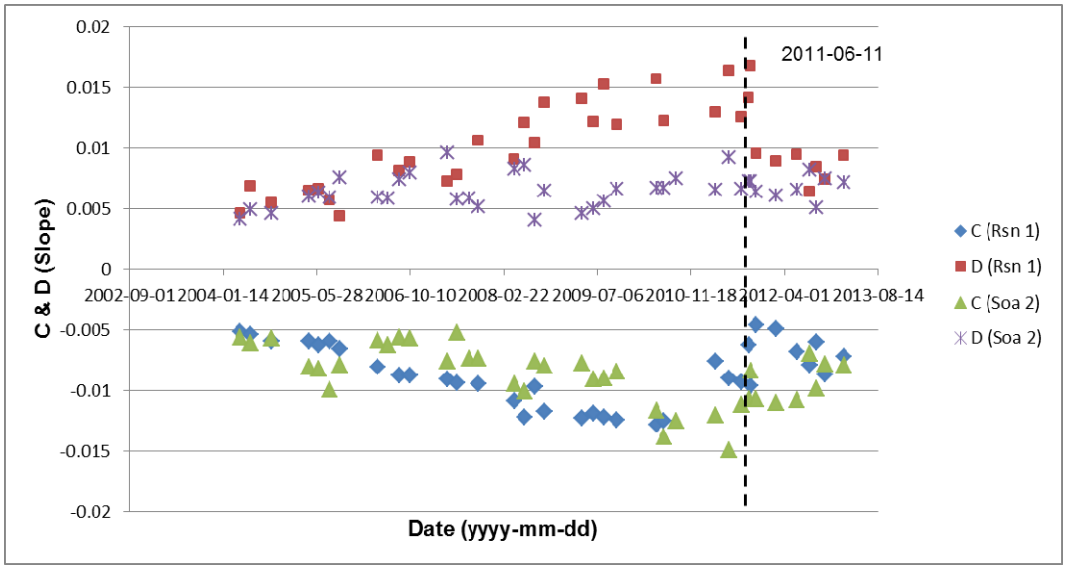
0.02
0.015
0.01
0.005
0
-0.005
-0.01
-0.015
-0.02
C & D (Slope)
2011-06-11
2002-09-01 2004-01-14 2005-05-28 2006-10-10 2008-02-22 2009-07-06 2010-11-18 2012-04-01 2013-08-14
Date (yyyy-mm-dd)
C (Rsn 1)
D (Rsn 1)
C (Soa 2)
D (Soa 2)

(b)

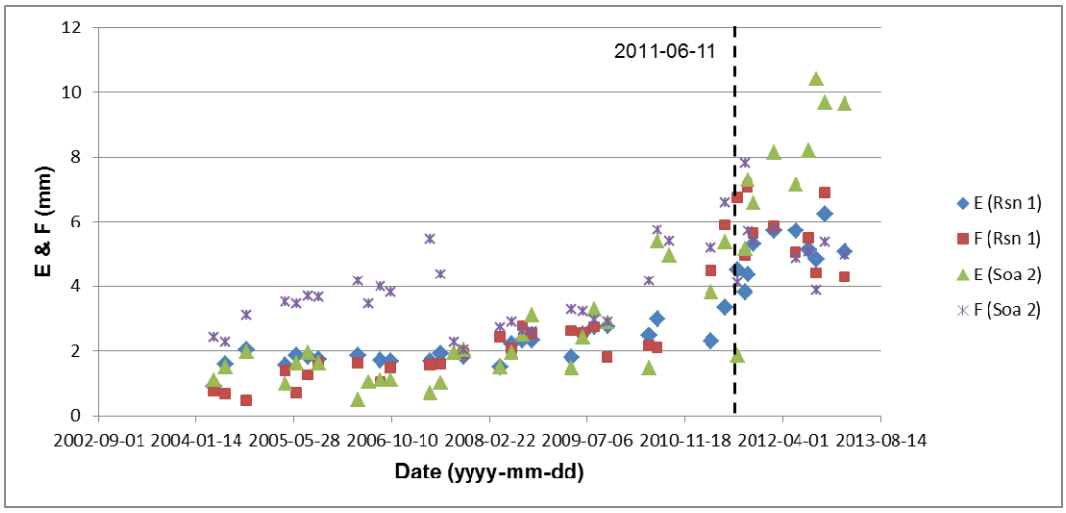
12
10
8
6
4
2
0
E & F (mm)
2011-06-11
2002-09-01 2004-01-14 2005-05-28 2006-10-10 2008-02-22 2009-07-06 2010-11-18 2012-04-01 2013-08-14
Date (yyyy-mm-dd)
E (Rsn 1)
F (Rsn 1)
E (Soa 2)
F (Soa 2)

(c)

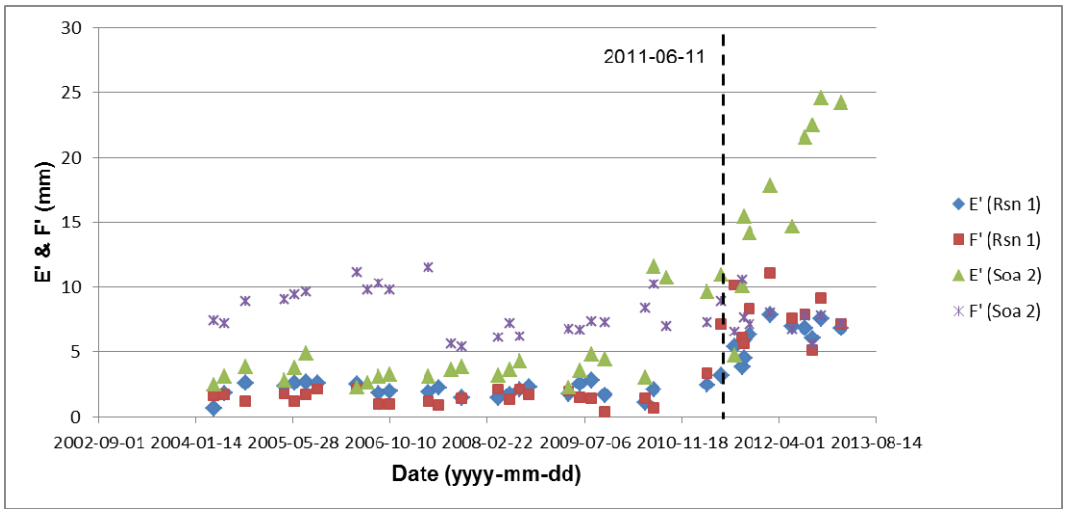
30
25
20
15
10
5
0
E' & F' (mm)
2011-06-11
2002-09-01 2004-01-14 2005-05-28 2006-10-10 2008-02-22 2009-07-06 2010-11-18 2012-04-01 2013-08-14
Date (yyyy-mm-dd)
E' (Rsn 1)
F' (Rsn 1)
E' (Soa 2)
F' (Soa 2)

(d)

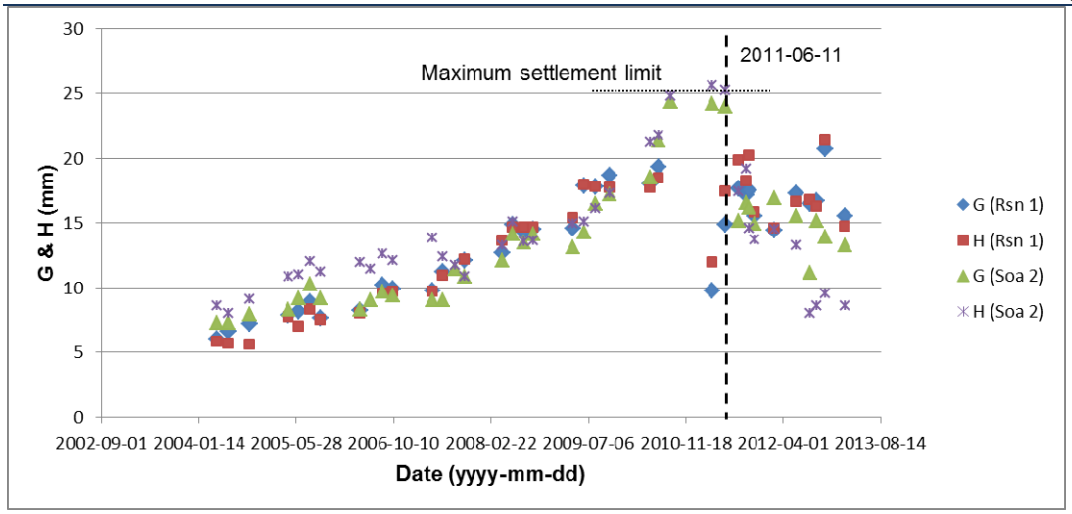

(e)

Figure 7-5 Trends of the defined Geometry parameters in selected turnouts (a) Parameter A, (b) Parameters C & D, (c) Parameters E & F, (d) Parameters E' & F' and (e) Parameters G & H

7.4 Evaluation of current maintenance strategy effectiveness

Trafikverket outsources the tamping of each line to different contractors, mostly using performance contracts. In this type of outsourcing, it is up to contractors to select appropriate methods and plan for the work. They are responsible for both regular measurements of track geometry and tamping.

In the performance contracts, two limits are specified for the Q-value, a goal limit and a contractual limit. If the actual Q-value of the track is higher than the goal limit, contractors will receive a bonus, while if it is below the contractual limit, they must pay a penalty.

Figure 7-6 evaluates the contractor performance from 2004 to 2010 on a case study line (Figure 7-6(a)) and a reference line in central Sweden (Figure 7-6(b)). It should be noted that the contractor is the same for both lines, but the contracts are different.

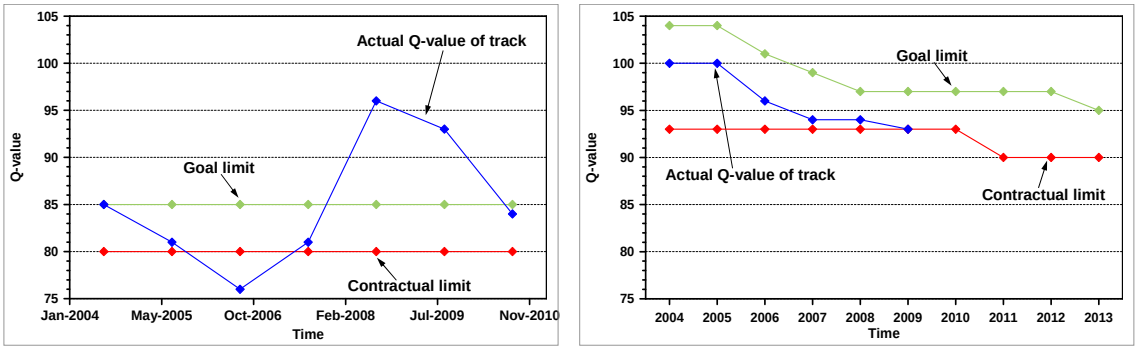

a) *b)*

Figure 7-6 Evaluation of the contractor's performance a: Contractor's performance on the case study line. b: Contractor's performance on a reference line in central Sweden.

The comparison of a contractor's performance on two different lines shows different maintenance policies. With the defined contractual and goal limits, the size of the associated penalties and bonuses will encourage the contractor either to be as close as possible to the lower contractual limit or to maintain a level above the goal limit. To interpret this, various

factors such as maintenance budget, functional requirements stated in the contract, amount of bonus and penalties mentioned in the contract, technical issues and maintenance decision criteria should be considered.

7.5 Specifying cost-effective maintenance limit for tamping

A cost model was developed to specify the cost-effective intervention limits (IL) for track geometry maintenance. The proposed model considered the degradation rates of different track sections and took into account the costs associated with inspection, tamping, delay time penalties and risk of accidents due to poor track quality. Track geometry data from the iron ore line (Malmbanan) in northern Sweden, used by both passenger and freight trains, was collected to estimate the geometrical degradation rate of each section. Since the effect of frost heaves on track geometry can introduce error into degradation trend analysis, only measurement data from June to October were considered.

As the inspection car (STRIX / IMV 100) has an error of 10-15 m (in some cases even higher) in specifying the longitudinal location of the track, the first step in data treatment was to adjust the sampled measurement data. Since the accuracy of the available programmes in data adjustment is unacceptable, the measurement data were adjusted manually.

Next, the standard deviation of the longitudinal level for each 200 m track section was calculated in every measurement. By applying the exponential regression trend line over the time series of the standard deviations, the degradation rate of each section could be estimated.

Since the occurrence of a twist 3 m fault greater than 15 mm or a twist 6 m fault greater than 25 mm is critical to derailment risk, the data reporting the occurrence of these failures between 2004 and 2010 were collected from the inspection reporting system to find the probability distribution of their occurrence. Results were presented in the previous study (see Figure 7-3). The probability function was used to determine the probability of safety fault occurrences at specified time intervals.

The model considered two types of faults: standard deviations of the longitudinal level and isolated safety faults (twist 3 m and 6 m). If the standard deviation of the longitudinal level for a 200 m track section goes over the specified IL and/or detection of safety faults, corrective tamping is performed at a fixed time interval after the inspection.

Figure 7-7 shows the observed tamping efficiency on the selected track sections, between 2007 and 2012, by specifying how much the longitudinal level deviation of each segment has been reduced by tamping. It also indicates the maintenance actions performed at different intervention limits.

To cover all degrees of tamping effectiveness, the model was run for two scenarios: the optimum scenario and the worst scenario. The optimum scenario uses the high maintenance effectiveness bound, while the worst scenario considers the low maintenance effectiveness bound (see Figure 7-7).

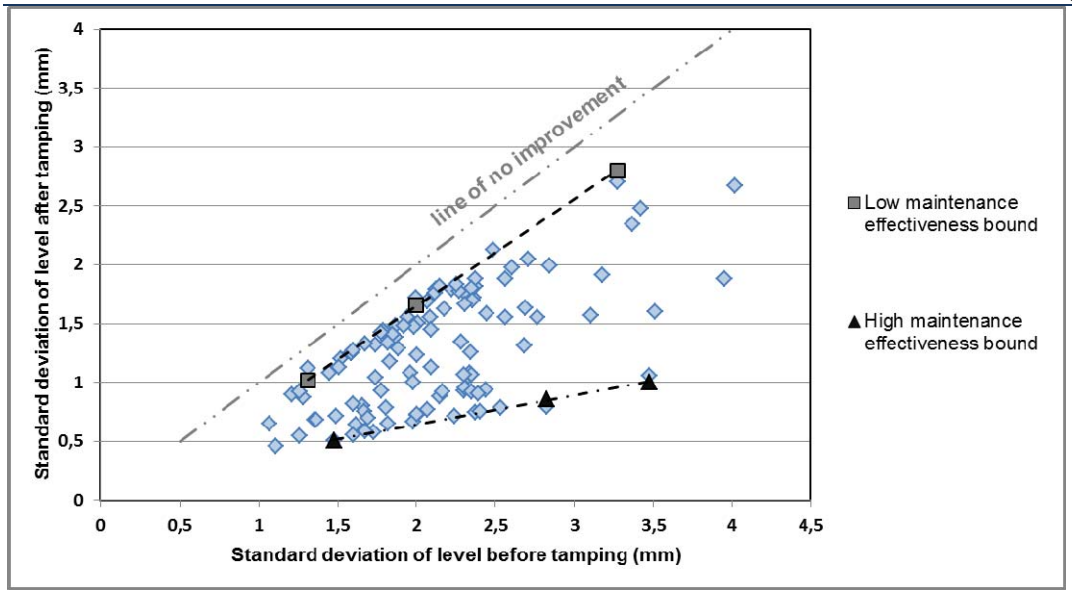

Figure 7-7 Observed tamping effectiveness within studied time interval

The simulation was performed for the time interval from 2013-04 to 2017-10. The total maintenance cost per MGT for each IL is shown in Figure 8. Depending on the maintenance effectiveness, the actual maintenance cost for each scenario can vary between the high and low maintenance effectiveness boundaries (grey dashed area in Figure 7-8). As can be seen, the seventh scenario (IL = 2 mm) is the most cost-effective alternative.

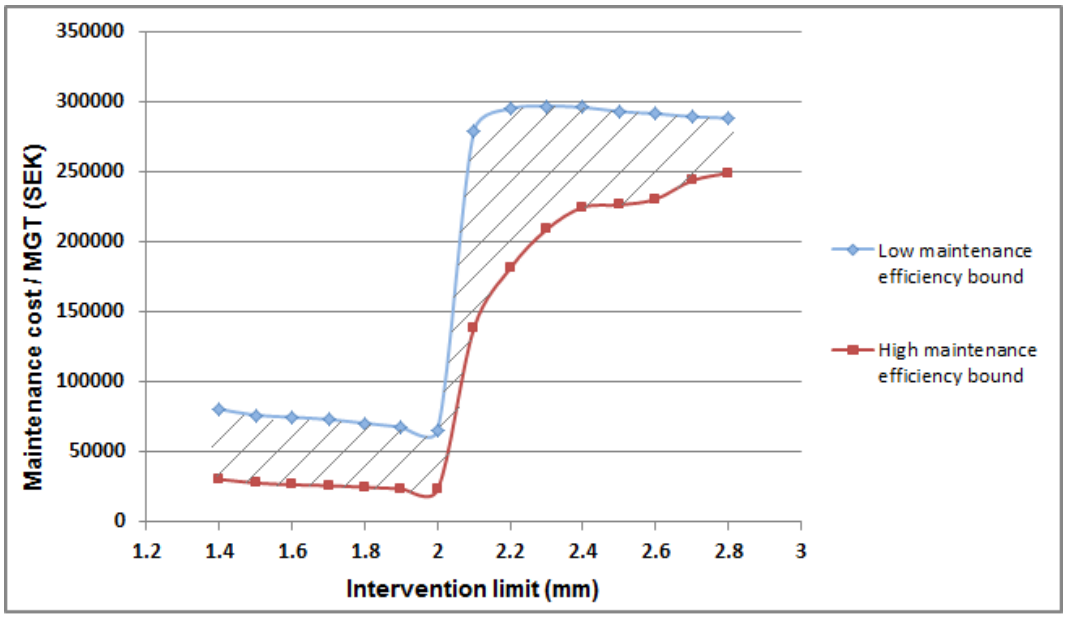

Figure 7-8 Comparison of maintenance cost per MGT for different intervention limits

The main reason for a sharp increase in maintenance cost by selecting the IL equal to or greater than 2.1 mm is the capacity loss cost due to speed reduction of passenger trains within a one-month planning horizon time interval.

The cost-effective IL should be specified for different track quality classes. The results of this study fit the quality class 2 of the studied line. In the south of Sweden, due to greater demand, the lines have better quality classes, allowing the trains to run at higher speeds. Therefore, lower intervention limits must be selected for tamping.

Although selecting IL=2 mm will result in the lowest maintenance cost, the amount of savings generated by deferring maintenance from 1.4 mm to 2 mm is not considerable. Allowing the track to deviate to higher levels can affect the energy consumption, ride comfort, and degradation rate of other components, and lead to faster settlement after tamping due to “track memory” etc. Therefore, in the long run and by considering the whole railway system, it may be more beneficial to select a lower IL than 2 mm.